



HAL
open science

Theoretical studies of constrained membranes

Osman Kahraman

► **To cite this version:**

Osman Kahraman. Theoretical studies of constrained membranes. Other [cond-mat.other]. Université de Lorraine, 2013. English. NNT : 2013LORR0109 . tel-01750097

HAL Id: tel-01750097

<https://hal.univ-lorraine.fr/tel-01750097v1>

Submitted on 29 Mar 2018

HAL is a multi-disciplinary open access archive for the deposit and dissemination of scientific research documents, whether they are published or not. The documents may come from teaching and research institutions in France or abroad, or from public or private research centers.

L'archive ouverte pluridisciplinaire **HAL**, est destinée au dépôt et à la diffusion de documents scientifiques de niveau recherche, publiés ou non, émanant des établissements d'enseignement et de recherche français ou étrangers, des laboratoires publics ou privés.



AVERTISSEMENT

Ce document est le fruit d'un long travail approuvé par le jury de soutenance et mis à disposition de l'ensemble de la communauté universitaire élargie.

Il est soumis à la propriété intellectuelle de l'auteur. Ceci implique une obligation de citation et de référencement lors de l'utilisation de ce document.

D'autre part, toute contrefaçon, plagiat, reproduction illicite encourt une poursuite pénale.

Contact : ddoc-theses-contact@univ-lorraine.fr

LIENS

Code de la Propriété Intellectuelle. articles L 122. 4

Code de la Propriété Intellectuelle. articles L 335.2- L 335.10

http://www.cfcopies.com/V2/leg/leg_droi.php

<http://www.culture.gouv.fr/culture/infos-pratiques/droits/protection.htm>

Theoretical Studies of Constrained Membranes



Osman KAHRAMAN

A thesis submitted for the degree of

Docteur en Physique

June 2013

Committee members

Jean-François Joanny (Reviewer)	Institut Curie, Paris
Igor Kulić	Institut Charles Sadron, Strasbourg
Carlos Marques	Institut Charles Sadron, Strasbourg
René Messina	Université de Lorraine, Metz
Hervé Mohrbach (Supervisor)	Université de Lorraine, Metz
Martin M. Müller (Supervisor)	Université de Lorraine, Metz
Helmut Schiessel (Reviewer)	Instituut Lorentz, Leiden
Norbert Stoop	Zürcher Hochschule für Angewandte Wissenschaften, Zürich

Acknowledgements

This work would not be possible without the guidance of Martin Müller and Hervé Mohrbach. I am more than grateful for their scientific and personal support. I also thank them for all the fun I had in Metz. Danke für alles Martin. Merci pour tout Hervé.

A very big thank you goes to Norbert Stoop. I enjoyed and learned a lot working with him. I am indebted to Igor Kulić for generously sharing his enthusiasm and his knowledge. I thank my friends and collaborators Jemal Guven, James Hanna and Gaetano Napoli for their contributions and for fruitful discussions. I express my gratitude to the other members of our laboratory, Alain Bérard, Yves Grandati, René Messina and Aotmane En Naciri for the good time we had.

I thank Jean-François Joanny and Helmut Schiessel for accepting to review my dissertation, and Carlos Marques for being in the committee.

Nothing would be possible without the love and the encouragement of my family. Teşekkürler Anne, Baba, Kaan. Teşekkürler Mehmet ve Sema Hocam.

Last but not least, my beloved wife Belgin, I can't thank you enough for always being there for me.

osman

March 2013

Abstract

The present thesis is devoted to the study of constrained membranes with a focus on biological structures such as growing tissues and the cell membrane. It combines analytical and numerical approaches to investigate the interplay of geometry and mechanics. It also includes some experimental results albeit they are few in number and modest in size.

After an introductory chapter, we explore three physical models addressed in three distinct chapters. In the first model, the deformations of growing soft tissues are treated as Gaussian point singularities in two dimensional surfaces. The equilibrium shapes are evaluated for two such defects forming a dipole. The predictions of the theory are also compared to tabletop experiments. The results of this work are reported in [I](#).

The next chapter studies the invaginations of self-avoiding fluid membranes in constrained spaces. To this end, we developed a Finite Element code and performed extensive simulations to construct a geometric phase diagram for a fluid membrane vesicle in a spherical confinement. We also investigate the effects of the membrane's spontaneous curvature and the deformations of the container on the geometry of the invagination. A survey of this work can also be found in [II](#) and [III](#).

In the fourth chapter of the manuscript, a tubular membrane composed of switchable components is proposed as a model to study conformations of intrinsically curved biological rods. We translated this system to a computational framework based on the Brownian Dynamics method and inquired how global shape emerges from local interactions. A publication related to this work is in preparation.

List of Publications

- I. J. Guven, J. Hanna, O. Kahraman, and M. M. Müller. Dipoles in thin sheets (submitted). [arXiv:1212.3262](#)
- II. O. Kahraman, N. Stoop, and M. M. Müller. Fluid membrane vesicles in confinement. *New Journal of Physics*, 14(9):095021, 2012.
- III. O. Kahraman, N. Stoop, and M. M. Müller. Morphogenesis of membrane invaginations in spherical confinement. *Europhysics Letters*, 97(6):68008, 2012. [arXiv:1201.2518](#)

Abrégé

La thèse est consacrée à l'étude des membranes sous contrainte en mettant l'accent sur les structures biologiques telles que les tissus en croissance et la membrane cellulaire. Elle combine des approches analytiques et numériques pour étudier le lien entre la géométrie et la mécanique. Elle contient également quelques résultats expérimentaux mais ce ne sont que peu nombreux et à petite échelle. Après un chapitre d'introduction, nous explorons trois modèles physiques abordés dans trois chapitres différents. Dans le premier modèle, les déformations des tissus mous lors de la croissance sont traitées comme des singularités ponctuelles gaussiennes dans les surfaces bidimensionnelles. Les formes d'équilibre sont calculées pour deux défauts qui forment un dipôle. Les prédictions du modèle sont par ailleurs comparées aux résultats des expériences. Le chapitre suivant étudie les invaginations des membranes fluides auto-évitant dans des espaces confinés. À cette fin, nous avons développé un code basé sur la méthode des éléments finis et effectué des simulations afin de construire un diagramme de phase (volume/surface) pour des membranes piégées à l'intérieur d'une sphère. Nous analysons également les effets de la courbure spontanée de la membrane et les déformations de la paroi extérieure sur la forme de l'invagination. Enfin, dans le quatrième chapitre de la thèse, en vue de modéliser des tiges biologiques, nous construisons une membrane tubulaire à partir d'éléments caractérisés par deux états géométriques. Cette approche nous a permis d'examiner, par le biais des simulations du type dynamique brownienne, comment la forme globale émerge des interactions locales.

Résumé

Etude théorique des membranes sous contrainte

Chapitre 1:

Introduction

La croissance et le développement des organismes ainsi que leur évolution au fil des générations dépendent fortement des contraintes physiques. Les lois physiques ne permettent pas certains plans d'organisation des êtres vivants: il n'existe pas d'animaux à roues puisque la circulation du sang n'est pas possible à l'intérieur d'un organe en rotation. Les lois de la diffusion limitent la taille des organismes, mais sont également responsable de la coopération des unités et du développement de structures complexes, tels que le xylème ou le phloème, les structures de transport vasculaires des plantes. Dans la nature, les mécanismes physiques lient la fonction si fermement à la forme qu'ils apparaissent comme une unité indivisible.

L'étude des formes, en particulier, nécessite l'observation systématique des motifs récurrents sur le corps entiers des organismes vivants. La collecte de données mène à une hiérarchie de structures qui soulève la question de savoir quels mécanismes particuliers conduisent à quelles structures particulières. Le but est alors de déterminer les contraintes physiques et biochimiques pertinentes parmi tout l'éventail d'interactions possibles. La compréhension de la complexité structurelle passe alors par la construction de modèles, nécessairement simplifiés pour se prêter à l'étude, mais suffisamment complexe aussi, pour fournir des réponses satisfaisantes.

Il est évident que la régulation chimique contrôle la formation du motif, mais les contraintes mécaniques peuvent également causer des modifications radicales de la géométrie de la matière vivante en réduisant la symétrie du système. L'importance des facteurs mécaniques dans la morphogenèse des tissus est largement reconnue, notamment pour les os et les muscles. Chez les plantes, la mécanique transmet de l'information géométrique entre deux différents niveaux d'organisation, la paroi cellulaire et les réseaux des microtubules.

Dans ce manuscrit, nous nous intéressons à l'interaction des contraintes mécaniques et de la géométrie pour des objets biologiques fins et minces. Ceux-ci sont caractérisés par leurs dimensions qui ne sont pas proportionnées. La peau ou la membrane cellulaire (objets minces) tombent dans cette catégorie puisque leur épaisseur est beaucoup plus petite devant leurs autres dimensions. Donc la taille de ces objets est proprement mesurée en termes d'aires. Par ailleurs, les composants du cytosquelette (objets fins), par exemple les microtubules, possèdent une seule dimension principale, par conséquent la taille peut être quantifiée en termes de longueurs. Bien que ces objets soient formés de composants discrets, l'ampleur de leur taille permet à un traitement dans le cadre de mécanique des milieux continus.

Dans cette perspective, nous allons examiner trois modèles physiques, abordés en trois chapitres distincts. Dans le premier chapitre, la déformation de tissus mous en croissance est traitée pour des singularités ponctuelles induites dans la surface. Le deuxième chapitre étudie les invaginations des membranes fluides dans des espaces restreints par un modèle numérique basé sur la méthode des éléments finis. Dans le dernier chapitre, nous nous servons d'une membrane tubulaire composée des éléments multistable pour étudier les conformations des filaments biologiques intrinsèquement courbés.

Chapitre 2:

Les dipôles dans les membranes minces élastiques

Dans l'organisation des êtres vivants en grandes structures, la croissance induit des formes élaborées comme les contours des feuilles des plantes ou les rides de la peau. Une des causes est la croissance anisotrope: les tissus ne se développent pas à la même vitesse dans toutes les directions. Mais l'intégrité du tissu est également exigée: ni des chevauchements ni des trous ne sont physiquement permis. Ces deux facteurs donnent lieu à des contraintes intrinsèques dans les tissus qui sont aussi appelés des *contraintes résiduelles* parce qu'elles sont toujours présentes même en absence des effets extérieurs.

Quand une dimension de ces systèmes est beaucoup plus petite par rapport aux autres dimensions, leurs formes sont convenablement décrites par des surfaces bidimensionnelles. Pour une surface, la déformation locale induite par la croissance peut être décomposée en deux degrés de liberté, la flexion et l'étirement. Dès qu'il devient plus facile de courber une telle membrane que de l'étirer, la configuration qui minimise l'énergie se trouve être celle qui confine l'étirement à des sommets et des crêtes pointus. Cet effet est analogue au froissement du papier. La déformation la plus simple de ce type peut être générée en enfonçant un papier plat dans un tube cylindrique par le biais d'une force ponctuelle. Mais le défaut conique créé de cette façon n'est pas une propriété intrinsèque du système, il est dû à des contraintes externes. Il est à remarquer que la longueur d'une courbe fermée à une distance unitaire est toujours égale à 2π . Considérons maintenant la forme d'un cornet de glace. Ce défaut particulier peut être reproduit en enlevant une tranche d'un disque et en collant les côtés exposés. Maintenant, la longueur d'une courbe fermée autour de la pointe du cône est $2\pi - \Psi$, avec Ψ égal à l'angle de la tranche retirée. La géométrie de la feuille autour du défaut est caractérisée par cet angle Ψ . La seule configuration stable qui minimise l'énergie de flexion est le cône circulaire régulier. Maintenant imaginons l'opération inverse qui consiste à insérer une tranche dans le disque plat. Le résultat est un nombre infini de formes pliées avec une symétrie diédrale comme des solutions d'équilibre. Le seul état stable c'est celui possédant la symétrie miroir. Dans la nature, les algues *Acetabularia acetabulum* développent des chapeaux coniques similaires à

ces défauts coniques.

Les déformations plus générales des membranes en croissance peuvent être étudiées par une construction multipolaire des défauts coniques. En principe, on peut combiner autant de défauts déficitaires et excédentaires qu'on veut sur une surface. Mais le multipôle le plus simple est un dipôle bien évident, composé d'un cône déficitaire et un deuxième excédentaires, séparés par une distance finie. Contrairement à un dipôle électromagnétique, la limite dipôle n'existe pas sur la feuille: la distance entre les défauts et la "magnitude" Ψ doivent être finies. En plus, cette superposition est d'une nature non-linéaire: lorsqu'on combine deux cônes, des étirements sont forcément introduits quelque part sur la surface. Nous allons contourner cette difficulté en faisant une approximation de la structure par une paire de pièces coniques maintenues ensemble par des faces planes. Dans notre analyse, nous négligeons l'énergie nécessaire pour créer la crête entre les deux défauts. Par conséquent, nous serons seulement intéressés par l'énergie de flexion des parties coniques, ce qui est quadratique en courbure moyenne.

Cette simplification nous permet d'étudier les deux parties coniques de la surface séparément. On sait que la surface obéit à l'équation de la structure:

$$M^2 - C^2 = \kappa'^2 + \frac{\kappa^4}{4} + (1 - C)\kappa^2, \quad (1)$$

où κ est la courbure de la surface exprimée dans un système de coordonnées adapté à la géométrie conique. M est la magnitude du vecteur conservé \mathbf{M} , associé à la symétrie rotationnelle continue du système. Enfin, la constante C est reliée à l'isométrie de la surface, autrement dit à la conservation de sa métrique. Nous résolvons cette équation pour les cônes déficitaire et excédentaire non fermés. L'interaction entre les deux parties se fait par l'intermédiaire des conditions à bords. Ainsi, en combinant les solutions isolées à l'aide de l'approximation mentionnée précédemment, nous obtenons toutes les solutions d'équilibres. En outre, en minimisant l'énergie de flexion, nous estimons des valeurs numériques pour l'angle α , qui correspond à l'ouverture des "ailes" de la surface du système dipolaire en fonction de Ψ . Pour comparer cette estimation aux mesures expérimentales nous avons construit des modèles en papier. Les prédictions de l'analyse théorique sont en bon accord avec les résultats expérimentaux.

Chapitre 3:

Les invaginations des membranes fluides

A part la croissance, des contraintes externes peuvent jouer un rôle essentiel dans la formation des membranes biologiques. Un exemple bien connu est la gastrulation de l'embryon de drosophile enfermé dans une coquille. Pour de nombreuses structures cellulaires, ce type de invagination est l'ingrédient principal pour un fonctionnement correct. Le réticulum endoplasmique constitue l'un des exemples les plus importants avec tous ses tubes et citernes formant un labyrinthe continu de membranes lipidiques. Dans le monde procaryote, la bactérie phototrope *Rhodobacter sphaeroides* développe des structures invaginées afin de multiplier sa surface et ainsi son exploitation de l'énergie solaire.

C'est peut-être la mitochondrie qui constitue le meilleur exemple de l'interaction entre la structure et la fonction. Par le remodelage effectif de sa structure interne repliée, la membrane interne de la mitochondrie contrôle de sa capacité de synthèse d'ATP. Les mitochondries sont des organelles entourées de deux couches de membranes phospholipidiques: la membrane externe et la membrane interne. La membrane interne a une surface plus grande que la membrane externe, donc elle est pliée vers la matrice, la solution aqueuse riche en protéines qui remplit l'organelle. Ces invaginations, appelées **crête**, ne sont pas des simple circonvolutions. Elles possèdent aussi une structure tubulaire ou lamellaire, reliées à la membrane interne par des ouvertures étroites appelées des **jonctions de crête**.

Pour différents types de cellules, il est possible d'observer des géométries totalement différentes d'invaginations internes mitochondriales. Des études expérimentales de la membrane interne suggèrent que l'ultrastructure de la membrane interne est le résultat d'une coopération entre la croissance de la surface, la composition des lipides et les effets des protéines. Des modèles simples conviennent sans doute pour comprendre la part de chaque contribution d'une manière clairement définie. Nous proposons un tel modèle comme un prototype de génération des invaginations. Notre modèle suppose la fluidité de la membrane, cependant, il n'est pas seulement valable pour les membranes lipidiques, mais il peut aussi être utile pour les tissus mous tant que les forces de cisaillement dans la surface peuvent s'équilibrer sur des échelles de temps plus petites que la croissance.

D'un point de vue théorique, la façon la plus simple de générer les invaginations de surface est d'imaginer une membrane ayant une surface et un volume constants, enfermée dans un conteneur rigide. Si la surface de la membrane dépasse celle du conteneur, elle doit flamber vers l'intérieur, cela est imposé par la géométrie. Alors, pour étudier les formes fondamentales de cette membrane enfermée, nous écrivons l'énergie d'Helfrich qui est au deuxième ordre en courbure moyenne H de la surface,

$$E_b = \frac{\kappa_b}{2} \int dA (2H - C_0)^2, \quad (2)$$

où κ_b est la rigidité de la membrane et la courbure spontanée C_0 représente la valeur préférée de la courbure moyenne. Donc nous cherchons les surfaces qui ont une surface et un volume constants, minimisant cette énergie sous contrainte de confinement. Pour cela, nous appliquons deux méthodes numériques différentes. Dans l'hypothèse d'axisymétrie de formes, ce problème variationnel peut être exprimé par un ensemble d'équations différentielles au premier ordre. Dans cette forme réduite, le système d'équations peut être intégré numériquement d'une manière relativement facile par une méthode de Runge-Kutta. Pour des géométries plus complexes possédant des asymétries et des auto-contacts, un traitement complet à trois dimensions du problème est plus approprié. Pour cela, nous avons mis au point un programme basé sur la méthode des éléments finis subdivisés qui convient à l'étude des membranes fluides.

En supposant $C_0 = 0$, d'après nos calculs pour un conteneur sphérique, nous discernons trois états différents. Pour des valeurs modérées de croissance de la surface, on observe des invaginations **axisymétriques**. Ces invaginations représentent une forme particulière: ils se composent d'un large domaine sphérique connecté à la partie de la membrane en contact avec le conteneur par un col étroit. Si on augmente encore l'aire de la surface, l'axisymétrie des invaginations est brisée et on trouve des invaginations **ellipsoïdales**. Pour une augmentation plus forte, la géométrie des invaginations change radicalement: on observe des invaginations du type **stomatocyte** qui se caractérisent par une invagination secondaire qui se forme à l'intérieur de la première. Nous avons classé ces structures dans un diagramme de phase à l'aide d'un modèle théorique

approximative.

Les invaginations axisymétriques obtenus pour la croissance modérée de la surface reproduisent la structure basique des invaginations biologiques tels que les crêtes mitochondriales ou gastrula embryonnaire. Il est intéressant de noter que, une coupe aléatoire effectuée sur une invagination du type stomatocyte ressemble à des images de la microscopie électronique des mitochondries dépourvues de la protéine mitofilin.

Nous étudions également les invaginations des membranes ayant une courbure spontanée constante non nulle. Nous montrons que la courbure spontanée fournit un moyen efficace de contrôle des échelles de longueur: déjà un petit changement dans sa valeur module la taille de l'invagination et sa jonction. En outre, nous examinons les effets d'un confinement non sphériques. En particulier, en utilisant des déformations ellipsoïdales du conteneur de simulation, nous montrons que les morphologies des invaginations sont stables par rapport aux petites perturbations géométriques.

Nos résultats pourraient aider à différencier les structures intrinsèques d'une membrane invaginée de celles qui sont issues des effets extrinsèques. Comme exemples de ces modulations externes, on peut penser à des interactions entre les protéines et la membrane dans le cas de la mitochondrie et à la différenciation cellulaire localisée dans le cas de la gastrulation. Ces deux effets peuvent être étudiés par l'introduction d'une courbure spontanée locale dans le système. Ceci peut être réalisé en mettant en œuvre une interface de type Ginzburg-Landau entre différents domaines de la membrane.

Chapitre 4:

Les tubes polymorphiques

Les effets des contraintes mécaniques se manifestent par un ensemble complètement différent de la morphologie dans le cas des objets unidimensionnels tels que les tiges ou les tubes. Comme exemple saillant, le monde macroscopique nous offre des vrilles végétales qui s'enroulent. Les plantes grimpantes, à la recherche d'un soutien structurel, cultivent des vrilles souples et flexibles. Les vrilles qui sont en contact avec un objet deviennent ligneuses et elles commencent à s'enrouler en spirale serrée. Dans cette phase, formant des ressorts naturels, les vrilles aident les plantes à résister à des vents et d'autres charges structurales.

Des études récentes sur les vrilles de vigne démontrent la formation d'une couche de cellules fibreuse gélatineuses lorsque ceux-ci sont enroulés. Les résultats suggèrent que ces fibres gélatineuses peuvent être la cause derrière l'enroulement chez les vignes par le biais de contraction asymétrique des fibres. Des expériences effectuées sur des systèmes modèles et de simulations numériques confirment cette vue de génération courbure intrinsèque via la brisure de symétrie radiale.

L'élasticité importe pour les objets macromoléculaires minces et longs aussi. Les biofilaments comme l'ADN ou les protéines hélicoïdales α sont traités avec succès dans le cadre de la théorie de l'élasticité en termes de courbures et des torsions. Par exemple, dans le cas des filaments d'actine, un membre de la famille du cytosquelette, la prédiction analytique de la longueur de persistance est en bon accord avec les mesures expérimentales. La longueur de persistance d'une tige, qui peut être définie comme une longueur au delà de laquelle le filament devient souple, est donnée par le rapport de rigidité κ aux fluctuations thermiques, $l_p = \frac{\kappa}{k_B T}$, où k_B est le constant de Boltzmann et T est la température. Pour des polymères réguliers, l_p est un constant qui dépend du matériel.

Cependant, un consensus sur les propriétés mécaniques des microtubules fait encore défaut. Il existe des preuves solides que la longueur de persistance des microtubules a une dépendance de longueur. Mais le fait que le comportement mécanique des microtubules est plus complexe que celui d'actine n'est pas tout à fait surprenant, puisque leur structure fait déjà soupçonner d'un niveau plus élevé de complexité. Les microtubules, qui exécutent des tâches multiples dans la

cellule, sont des cylindres creux constitués de dimères protéiques intrinsèquement courbés formant la paroi.

Pour comprendre ces anomalies, un modèle de tube anisotrope a été développé. Ce modèle est capable de prédire une longueur de persistance qui dépend de longueur du faisceau. Toutefois, ce modèle ne fournit pas un cadre cohérent pour aborder toutes les particularités mécaniques des microtubules. Dans une tentative d'interpréter les différents aspects de la mécanique des microtubules dans un scénario minimal, un modèle de tube polymorphe a été mis au point à partir de deux principes:

1. Les microtubules sont constitués de composés de dimères multistables qui peuvent être commutés entre les états droits et courbés.
2. Les dimères interagissent en coopération le long de l'axe du tube.

Ce modèle fournit des prédictions sur les propriétés statiques et dynamiques de la mécanique des microtubules qui sont en bon accord avec les résultats expérimentaux.

Inspiré par ce modèle de tube polymorphe, nous proposons et étudions un modèle de tube élastique anisotrope composé d'unités (dimères de tubuline) multistables et coopératives. A partir des interactions microscopiques de ces unités, nous allons progressivement explorer notre modèle pour expliquer comment une brisure de la symétrie globale pourrait être possible. Nous pavons la paroi du tube en sous-unités rectangulaires composées de deux carrés pouvant décrire un état courbé en modifiant l'angle entre les plans définis par ces carrés. Les propriétés élastiques sont assurées par des potentiels harmoniques d'étirement et de flexion associés aux liens de ce réseau. La bistabilité des unités est réalisée via les propriétés de flexion des liens qui passent par le milieu de rectangles. Pour cela, on choisit un potentiel quartique de flexion ayant un minimum à l'état rectiligne et un second minimum à l'état courbé avec une énergie plus faible. Donc pour une unité isolée l'état courbé est plus favorable. Dans le système, nous avons aussi un terme de coopérativité favorisant les états semblables entre sous-unités voisines longitudinalement. Nous intégrons ce système dans le temps en utilisant la méthode de la dynamique brownienne.

Les simulations numériques montrent que, dû à la compétition entre les différents termes élastiques dans le système, chaque section transversale du tube est capable d'adopter au moins trois configurations différentes. Deux de ces configurations ont une symétrie cylindrique. La dernière est la plus intéressante puisque cela correspond à une section fléchi, qui brise la symétrie cylindrique. Nous montrons que les transitions de ce système peuvent être comprises qualitativement en utilisant un modèle réduit qui représente une section du tube par trois cercles.

Pour les tubes composés d'un grand nombre de ces sections asymétriques, nous observons que l'orientation relative des sections successives peut être contrôlé par des interactions coopératives et répulsives le long de l'axe du tube. Lorsque les interactions répulsives sont plus fortes, les sections des tubes sont fléchies dans des directions radialement opposées, leurs déviations locales se neutralisent sur des longues échelles et le tube reste droit. Mais quand les forces d'attraction commence à contrebalancer les répulsifs, les sections ont d'abord une tendance à s'aligner localement. Pour une coopérativité suffisamment élevée, les sections sont déviées vers une même direction choisie au hasard rappelant le flambage d'Euler des tiges. Mais dans le cas du tube polymorphe, le flambage n'est pas induit sous l'effet d'une compression externe, mais il apparaît en raison de l'organisation interne des ses constituants. Ainsi on confirme les résultats du modèle polymorphe théorique en montrant la capacité du modèle à générer des courbures intrinsèques globales. Une direction pour une analyse plus approfondie est d'étudier la réponse du tube polymorphe aux forces et des couples extérieurs. Les effets des propriétés particulières méritent également à être étudiés. On peut facilement penser à intégrer un écart (seam) et une torsion intrinsèque qui sont présents dans le réseau des microtubules ou un cœur interne pour le cas des vrilles enroulées. Ce dernier peut également être pertinent pour la manufacture des systèmes robotiques souples.

Chapitre 5:

Perspectives

Tout au long de ce manuscrit, nous avons présenté nos recherches des réponses à problèmes qui s’organisent autour de la question “Comment les objets biologiques prennent leur forme?” En particulier, nous nous sommes intéressés à la morphogenèse des structures minces sous contraintes internes ou externes. Notre but n’était pas d’expliquer les spécificités des systèmes particuliers, mais de fournir des mécanismes généraux comme des générateurs des motifs de forme qui peuvent constituer les composantes de base des morphologies complexes. Nous avons donc eu pour but de lier la mécanique à la géométrie, espérant extraire des traits universels.

Dans la première partie, le modèle proposé était motivé par la structure flambée des tissus mous en croissance, alors que, dans notre deuxième modèle nous avons été guidés par les invaginations des membranes restreintes dans des espaces fermés. Enfin, pour le dernier modèle, notre motivation a surgit de la structure des tiges biologiques intrinsèquement courbés. Tout en développant nos modèles, nous nous sommes contraints à les rendre aussi simple que possible mais assez complexe pour saisir des aspects non triviaux. Les propriétés dimensionnelles des objets que nous avons abordés nous ont permis d’utiliser une approche basée sur la mécanique des surfaces. Dans ce cadre général, nous nous sommes servis des diverses méthodes qui vont des calculs analytiques à quelques expériences à petite échelle dans le chapitre 2, mais surtout de simulations numériques.

À l’avenir, une approche plus complète mérite d’être développée par la combinaison des facteurs internes et externes. Une étude systématique de la stabilité et la réponse à des charges structurales des dipôles que nous avons traités dans le chapitre 2 peut être intéressant pour des applications pratiques. On peut aussi penser à étudier les interactions des tubes polymorphes avec des membranes, ce qui est sans doute pertinent pour de nombreux processus biologiques. Dans la même direction, les invaginations des membranes enrichies par des protéines est un sujet qui attend encore être modélisé en termes simples bien que cela posera de nouveaux défis au niveau des méthodes numériques.

Contents

1	Constrained membranes	1
2	Dipoles in thin sheets	5
2.1	Conical defects	9
2.1.1	Bending of a constrained sheet	9
2.1.2	Geometry of a cone	10
2.1.3	Bending a cone	12
2.2	Dipole defects	14
2.2.1	Determination of curvature	15
2.2.2	Boundary conditions	16
2.2.3	Results	21
2.3	Conclusion	26
3	Fluid membrane invaginations	29
3.1	Mitochondria	30
3.2	Biological membranes	32
3.2.1	Molecular structure of biological membranes	32
3.2.2	Membrane proteins	34
3.2.3	Membrane mechanics	35
3.3	Model	37
3.4	Results	39
3.4.1	Spherical confinement	39
3.4.1.1	Moderate surface growth	39
3.4.1.2	High surface growth and symmetry breaking	46
3.4.2	Confined vesicles with spontaneous curvature	50

CONTENTS

3.4.3	Influence of the container geometry	52
3.5	Conclusion	57
4	Polymorphic tubes	59
4.1	Microtubules	63
4.1.1	Structure of microtubules	63
4.1.2	Experiments on microtubules	65
4.1.3	Anisotropic beam model	67
4.1.4	Polymorphic tube model	69
4.2	Numerical model	72
4.3	Results	75
4.3.1	One ring of dimers	75
4.3.2	Longer tubes	79
4.4	Conclusion	86
5	Final remarks	87
A	Parametrization of a surface	89
B	Harmonic approximation for dipole defects	91
C	Numerical calculations	97
D	Finite element simulations	101
D.1	Discretization	102
D.2	Self-avoidance	106
E	Brownian dynamics simulations	111
E.1	Stretching forces	111
E.2	Bending forces	112
E.3	Parameters	114
	References	117

List of Figures

2.1	Deformations of elastic sheets	6
2.2	Conical defects	7
2.3	Dipole geometries modeled with an A4 sheet of paper	8
2.4	Definition of variables for the surplus cone.	11
2.5	The angle β as a function of α for the torque dipole and the force dipole	21
2.6	Surplus cone touching the planar regions of the dipole	22
2.7	Dipole solutions as a function of (Ψ, α)	23
2.8	Minimal bending energy $\tilde{B}_{\min}^{\text{tot}}$ as a function of Ψ	24
2.9	Dependence of the angle α_{\min} on Ψ	25
3.1	Electron tomography images for different types of cristae	31
3.2	Illustration of the cell membrane with different types of membrane proteins embedded into the lipid matrix	33
3.3	Axisymmetric invagination of a fluid membrane inside a spherical container	40
3.4	Mean curvature and container force for axisymmetric invaginations	41
3.5	Geometric phase diagram with vertical slices of each simulation point.	44
3.6	Simple model omits the neck	47
3.7	Geometric phase diagram with vertical slices of each simulation point.	48
3.8	Slices of a finite element solution with high area	49
3.9	Slices of numerical equilibrium solutions of a membrane with spontaneous curvature	51

LIST OF FIGURES

3.10	Numerical equilibrium solution for a membrane inside an ellipsoidal container	53
3.11	Detachment of the membrane from the container	55
3.12	Shift of the transition lines for ellipsoidal containers	56
4.1	Tendrils perversion	60
4.2	Biofilaments of the cytoskeleton	61
4.3	Self-assembly of microtubules	63
4.4	Lattice deformation in microtubules due to the seam	64
4.5	Experimental methods for rigidity measurements	66
4.6	Polymorphic tube model	70
4.7	Construction of the polymorphic tube.	73
4.8	Two configurations for one ring of dimers	76
4.9	Simple model for one ring of dimers	77
4.10	Energy as a function of stretching rigidity for different minima of the simple model	78
4.11	Configurations for long tubes.	80
4.12	The effect of the horizontal bending μ_{b1}	81
4.13	The interaction energy E_{int} as function of θ	83
4.14	Cooperative confoplexes with protofilaments having 40 dimers	85
A.1	Surface parametrization	90
C.1	Definition of variables for numerical calculations of the axisymmetric invaginations	98
D.1	Handling of triangle-triangle contacts	107
E.1	Definitions of bond vectors	112

Chapter 1

Constrained membranes

The growth and the development of organisms and their evolution along generations depend heavily on physical constraints. Physical laws forbid for instance some body plans: there is no animal on wheels since the circulation of blood is not possible inside a rotating organ [1]. Obeying the laws of diffusion limits the size, but also provokes the cooperation of units and the development of elaborate structures, the transport tissues *xylem* or *phloem* of the vascular plants being striking examples [2]. In contrast to man made tools and devices, in nature, physical mechanisms tie the function tightly to the form.

The study of forms, in particular, requires a systematic observation of recurrent patterns on the whole bodies of living organisms and their parts. The collection of data leads to a hierarchy of structures which raises the question of which particular set of mechanisms leads to a particular structure. The task is to determine the relevant physical and biochemical constraints among the wide set of possible interactions. The understanding of the structural complexity requires constructing models, as simple as possible and powerful enough to provide satisfactory answers.

It goes without saying that the chemical regulation controls pattern formation, but mechanical constraints can also induce radical changes in the geometry of living matter by reducing the symmetry of the system. The importance of mechanical factors in the morphogenesis of tissues is largely acknowledged, especially for bones [3] and muscles [4]. In plants, the mechanics convey geometrical information between two different organization levels, the cell wall and the mi-

1. CONSTRAINED MEMBRANES

croton tubule arrays [5].

In this manuscript, we will be interested in the interplay of mechanical constraints and the geometry in the context of slender biological objects. These objects are characterized by having disproportionate dimensions. Tissues or membranes fall into this category since their thickness is much smaller than their lateral extension, their size is conveniently measured in terms of area. The constituents of the cytoskeleton, *e.g.* microtubules, on the other hand, possess one leading dimension, hence they are adequate to be quantified in terms of length. Albeit they are formed by discrete constituents, the dimensions of such objects justify a description in terms of continuum mechanics.

The morphogenesis of tissues is governed by differential growth which induces residual stresses. Due to this internal mechanical constraint, living tissues buckle in a way similar to crumpled paper: the stretching is concentrated in some sharp peaks and ridges. The physics of the simplest deformation of such kind can be captured by a conical point defect with a surplus or deficit angle. In the next chapter we will investigate a generalization of this growth model. We will combine two such defects, and study the equilibrium configurations of the dipole composed of one deficit and one excess cone.

Contrastingly, the source of mechanical constraints can be external. The folded structures of the mitochondrial crista or the gastrula in *drosophila* embryogenesis are salient examples with two different length scales. The confinement, *i.e.*, the outer membrane in mitochondria and the egg in *drosophila*, restrains the system to be in a specific portion of the space and helps it to invaginate. Certainly, there are other factors that interfere with the invaginations, *e.g.* curvature inducing proteins in mitochondria and the cell polarization in *drosophila*. To understand each contribution in a clearly defined way, a simple model system is a great help. To study the morphology of a typical folding process, in chapter 3, we consider such a model consisting of a closed membrane confined in a spherical cavity. If the area of the membrane exceeds the area of the confining sphere slightly, we observe a single axisymmetric invagination as a result of our numerical computations. A higher increase in the surface area forces the membrane to break the symmetry. We also investigate the effects of the spontaneous curvature of the membrane and the deformations of the container on the geometry of the

invagination.

The effects of mechanical constraints result in a completely different set of morphology in the case of one dimensional objects such as rods or tubes. The macroscopic world offers us coiling plant tendrils as an enchanting example to contemplate. In vine tendrils coiling is believed to be triggered by a thin layer of specialized cells capable to generate intrinsic curvatures. On the macromolecular level, microtubules are one of the amazing rod-like biopolymers undertaking multiple tasks in the cell. They are hollow cylinders composed of intrinsically curved protein subunits. When microtubules self-assemble, their cylindrical structure compels these building blocks to be in a straight configuration. The frustration caused by such a mechanical confinement is a good starting point to develop a polymorphic model to explain static and dynamic properties of microtubules [6]. Inspired by this approach, in chapter 4, we propose an anisotropic elastic tube model composed of multistable and cooperative patches. Starting from the microscopic interactions of the units, we gradually build up our model to explain how a global symmetry breaking could be possible.

1. CONSTRAINED MEMBRANES

Chapter 2

Dipoles in thin sheets

Every living organism grows one way or another. As they organize in large structures, the growth induces shapes of rich complexity such as the contours of plant leaves [7] or the wrinkles of the skin [8]. One cause is anisotropic growth: not all points in a tissue grow at the same rate. But there is also the requirement of integrity: neither overlaps nor holes are physically possible. These two factors result in internal stresses in tissues which are as well called *residual* [9], since they persist in tissues even without any external constraints.

Often, one dimension of a growing system is very small compared to its two other dimensions. Therefore, it is legitimate to describe such thin objects by two-dimensional surfaces. For a surface, the local deformation induced by the growth can be decomposed into two degrees of freedom, bending and stretching. When it is much easier to bend such a membrane than to stretch it, the configuration that minimizes the energy is found to confine the stretching to some localized sharp peaks and ridges [10].

This effect is similar to paper crumpling (see Fig. 2.1a). The surface of the paper is spanned by a network of peaks and ridges (Fig. 2.1b). The simplest deformation of such kind can be generated by applying a point force to a flat paper to push it into a hollow cylinder (see Fig. 2.1c and also [11, 12, 13]). But the conical defect created this way is not an intrinsic property of the system, it is generated as a response to an external load. Note also that the length of a closed curve around the defect at a distance of one is always 2π . Now, compare this with the shape of an ice cream cone in Fig. 2.2a. There, the point defect

2. DIPOLES IN THIN SHEETS

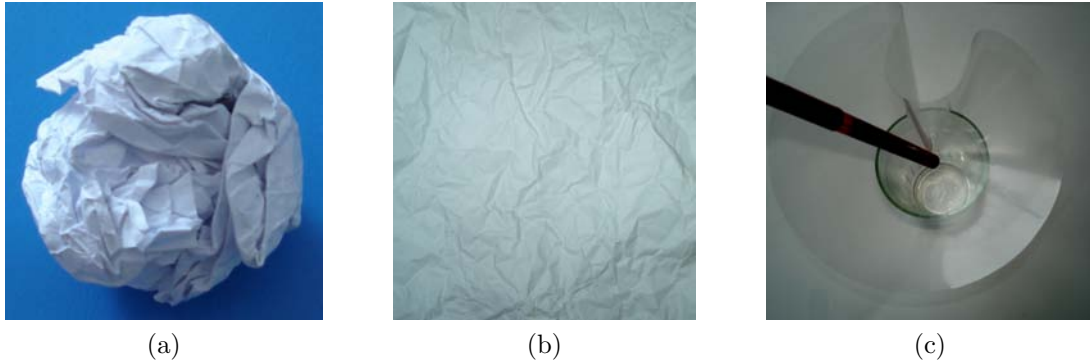


Figure 2.1: Deformations of elastic sheets. (a) Crumpled paper ball, (b) flattened crumpled paper, and (c) developable cone.

is due to the removal of a wedge followed by gluing. A closed curve around the apex of such a cone is $2\pi - \Psi$, Ψ being the angle of the removed wedge. The geometry of the sheet around the point defect is characterized completely by this angle Ψ . The only stable configuration that minimizes the cost of bending is the regular circular cone. The reverse operation consists of adding a wedge of surplus angle Ψ to a flat disc [14, 15]. The result is an infinite number of dihedrally symmetric circular folds as equilibrium shapes. The only stable one is the state with a two-fold symmetry (see Fig. 2.2b and [16]). In nature, the unicellular algae *Acetabularia acetabulum* (Fig. 2.2c) develops similar conical caps during their development [17].

More general deformations of “stretch-phobic” membranes can be studied by constructing multipoles of conical defects. The question of how to construct such multipoles has been hinted at in the treatment of disclination dipoles as “dislocations” in crystalline membranes [18, 19]. So in principle, one can combine any number of deficit and surplus point defects on the sheet. One common example is folding a cardboard box from a flat template: on eight vertices eight point defects are generated.

The simplest of such composite defects is a dipole, constructed by combining one deficit and one excess cone on the sheet, separated by a finite distance. In contrast with an electromagnetic dipole, the dipole limit does not exist on the sheet: the distance between the defects and their “charges” should be finite, one

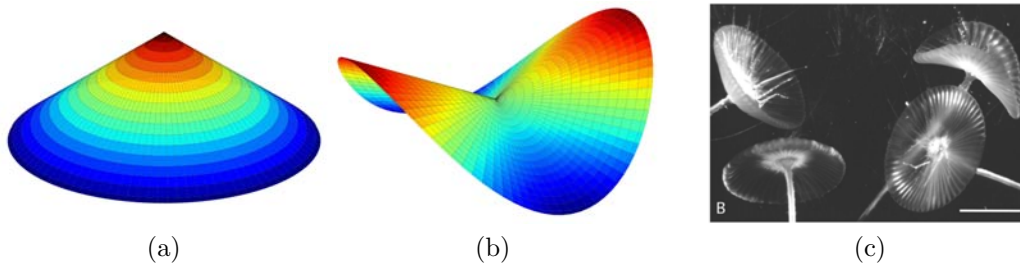


Figure 2.2: Conical defects. (a) Cone and (b) e-cone, and (c) algae *Acetabularia acetabulum* (from [17] with permission of the publisher).

cannot remove an arbitrarily large wedge from the surface. A more delicate complication arises from the non-linear nature of the superposition. In general, when stitching two cones together, some stretching is inevitably introduced somewhere on the surface. We will bypass this difficulty by approximating the polar geometry by a pair of conical pieces held together by a ridge with planar faces on either side interpolating between the cones. In our analysis, we will neglect the energy required to create the ridge between the two defects. Hence, we will be only interested in the bending energy of the conical parts, which is quadratic in mean curvature. As crude as it seems, this simple model is sufficient enough to understand the broad features of the dipole.

The best way to familiarize oneself with the peculiar geometry of a dipole defect on an unstretchable sheet is to construct one with a sheet of paper. A nice way to do this starts by marking two points that form a line near the center of the sheet, parallel to the longer side. Then, at one of the points, cut out a wedge of angle Ψ and glue the two exposed sides together. At the other point, do the opposite: make an incision from that point to the boundary to expose two sides. Then insert the Ψ -wedge by gluing. To get pretty dipoles, round off two sides in conical forms (see Fig. 2.3).

Two distinct stable shapes are possible: either the two sides extend into two opposite regions of space (Fig. 2.3a), or the whole sheet lies beneath the line joining the two points (Fig. 2.3b). Both of these configurations are stable with respect to small perturbations of the sheet. Provided that significant forces are applied, it is also possible to transform one configuration to the other one. Away

2. DIPOLES IN THIN SHEETS

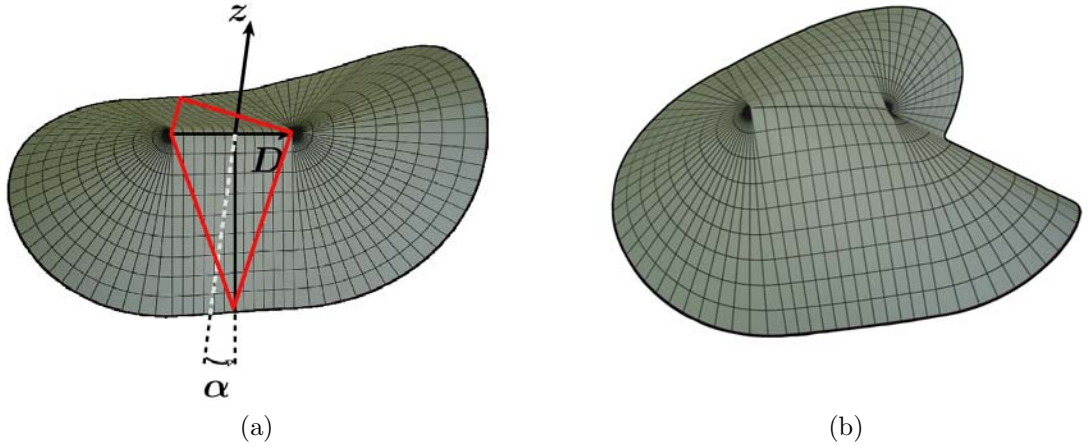


Figure 2.3: Dipole geometries modeled with an A4 sheet of paper. (a) Torque dipole and (b) force dipole of strength $\Psi = \frac{\pi}{4}$ and dipole length $D = 6$ cm.

from the singular points, the shape of the dipole in Fig. 2.3b resembles the “developable cone” obtained by pushing a sheet into a cup with a point *force* at its center (Fig. 2.1c). In the following, we will refer to this configuration as the **force dipole**. Following the same cup analogy, the second dipole in Fig. 2.3a seems to represent an applied *torque*. Accordingly, we will call this configuration **torque dipole**.

In both models, the surface of the sheet can be approximated by two open conical domains, one with a deficit angle and the other with a surplus, joined by two planar regions. For the torque dipole, the two planar regions seems to form neat triangles, with two corners at two singularity points and the third corner lying on the boundary of the sheet (the patch enclosed by the red borders in Fig. 2.3a). The two triangular regions seems to meet at the ridge with a sharp dihedral angle 2α . For the force dipole, we will use the same planar region approximation, but we have to keep in mind that the ridge is not straight for this type of dipole; moreover the flat regions are not as easily identifiable as in the case of the torque dipole.

In our theoretical analysis, \mathbf{D} denotes the dipole vector. It points from the deficit singularity to the surplus singularity along the straight ridge connecting two conical parts (see Fig. 2.4b). The vector \mathbf{z} will denote the vertical axis which is perpendicular to \mathbf{D} and which lies in the apparent mirror plane of the

equilibrium dipole geometries.

In the next section, we will start by describing the geometry and mechanics of isolated conical defects. We will mainly follow the derivations of Guven and Müller [20]. The application of these results to the dipole defects and comparison to experimental results will be pursued in section 2.2.

2.1 Conical defects

2.1.1 Bending of a constrained sheet

For an arbitrary configuration $\mathbf{X}(s^1, s^2)$ of a surface, parameterized by the set of local variables s^i the bending energy is given by

$$E_b[\mathbf{X}] = \frac{\kappa_b}{2} \int dA (2H)^2, \quad (2.1)$$

where H is the mean curvature and dA is the area element (see appendix A for a definition of the geometrical measures). In the following we will set the bending rigidity κ_b to one.

When the sheet is deformed, it should remain intrinsically flat, *i.e.*, the Gaussian curvature vanishes everywhere except in the neighborhood of induced defects. It also resists to shear or stretching deformations. These constraints can be implemented by fixing the metric $a_{\alpha\beta}^0$ at every point on the surface via a tensorial Lagrangian multiplier function $T^{\alpha\beta}$:

$$E_C[\mathbf{X}] = E_b[\mathbf{X}] - \frac{1}{2} \int dA T^{\alpha\beta}(s^i) (a_{\alpha\beta} - a_{\alpha\beta}^0). \quad (2.2)$$

Applying an arbitrary deformation $\mathbf{X} \rightarrow \mathbf{X} + \delta\mathbf{X}$, the equilibrium can be expressed as a conservation law:

$$\nabla_\alpha \mathbf{f}^\alpha = 0, \quad (2.3)$$

2. DIPOLES IN THIN SHEETS

where the stress tensor can be written as the sum of bending and metric terms:

$$\begin{aligned}\mathbf{f}^\alpha &= \mathbf{f}_0^\alpha + T^{\alpha\beta} \mathbf{e}_\beta \\ &= [-2H (b^{\alpha\beta} + a^{\alpha\beta} H) \mathbf{e}_\beta + 2(\nabla^\alpha H) \mathbf{n}] + T^{\alpha\beta} \mathbf{e}_\beta.\end{aligned}\quad (2.4)$$

The normal projection of the conservation law gives the shape equation:

$$\varepsilon = \varepsilon_0 - b_{\alpha\beta} T^{\alpha\beta} = 0, \quad (2.5)$$

where the bending contribution is given by

$$\varepsilon_0 = 2\nabla^2 H - 2H(2H^2 - b_{\alpha\beta} b^{\alpha\beta}). \quad (2.6)$$

The tangential projection of the conservation law implies the conservation of $T^{\alpha\beta}$:

$$\nabla_\alpha T^{\alpha\beta} = 0. \quad (2.7)$$

2.1.2 Geometry of a cone

A natural representation of the conical geometry consists of closed curves, each one is the intersection of the surface with a sphere centered on the apex. We parametrize the curve Γ on the unit sphere with $\Gamma : s \rightarrow \mathbf{u}(s)$, where s is the arc length (see Fig. 2.4a). Therefore, the overall surface can be parametrized by the mapping:

$$(r, s) \rightarrow \mathbf{X}(r, s) = r\mathbf{u}(s). \quad (2.8)$$

The tangent vector adapted to this representation reads $\mathbf{t} = \mathbf{u}'$, where prime is a derivative with respect to the parameter s . The normal to the surface is given by $\mathbf{n} = \mathbf{u} \times \mathbf{t}$. The surface is flat along r , but it is curved along s with the curvature

$$\kappa = -\mathbf{n} \cdot \mathbf{t}' = -(\mathbf{u} \times \mathbf{t}) \cdot \mathbf{t}' = -\mathbf{u} \cdot (\mathbf{t} \times \mathbf{t}'). \quad (2.9)$$

The vectors \mathbf{u} , \mathbf{t} , and \mathbf{n} form a right-handed basis adapted to the geometry of the surface. Given the curvature κ , the curve (and the surface) can be constructed

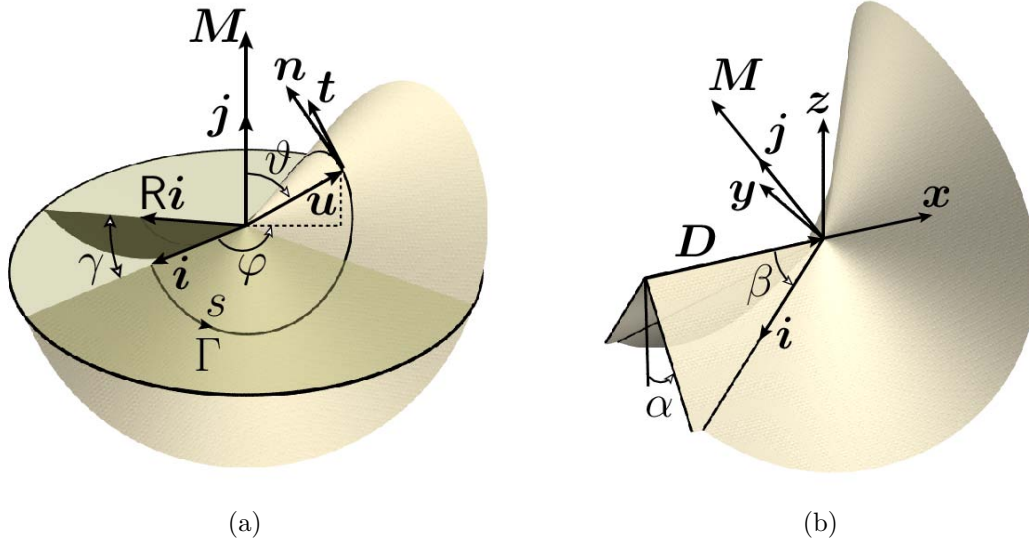


Figure 2.4: Definition of variables for the surplus cone. The same conventions are used for the deficit defect. (a) Local surface basis ($\mathbf{u}, \mathbf{t}, \mathbf{n}$). The vector \mathbf{j} is chosen in the direction of \mathbf{M} , and the generators along the boundaries are given by \mathbf{i} and $R\mathbf{i}$, both perpendicular to \mathbf{j} . The direction of the vector \mathbf{u} is expressed by its azimuthal and polar angles on the unit sphere, φ and ϑ , respectively. The azimuthal angle is measured with respect to \mathbf{i} and the polar angle with respect to \mathbf{j} . (b) A right handed Cartesian chart $(\mathbf{x}, \mathbf{y}, \mathbf{z})$. The unit vector \mathbf{x} is parallel to the dipole vector \mathbf{D} and it points away from the ridge. Note that the torque vector \mathbf{M} is not necessarily aligned with the vertical axis \mathbf{z} .

using the structure equations, similar to the Frenet-Serret equations [21]:

$$\begin{aligned}
 \mathbf{u}' &= \mathbf{t}, \\
 \mathbf{t}' &= -\kappa\mathbf{n} - \mathbf{u}, \\
 \mathbf{n}' &= \kappa\mathbf{t}.
 \end{aligned} \tag{2.10}$$

Then, the two fundamental forms are (see appendix A)

$$a_{\alpha\beta} = \begin{pmatrix} 1 & 0 \\ 0 & r^2 \end{pmatrix}, \quad b_{\alpha\beta} = -r \begin{pmatrix} 0 & 0 \\ 0 & \kappa \end{pmatrix}, \tag{2.11}$$

where $a_{\alpha\beta}$ and $b_{\alpha\beta}$ are respectively the metric and the curvature tensors.

2. DIPOLES IN THIN SHEETS

Not surprisingly, the Gaussian curvature $K = \det(b_{\alpha\beta})$ vanishes everywhere, whereas the mean curvature is $H = -\frac{\kappa}{2r}$.

2.1.3 Bending a cone

In general, for a specific problem, one should solve Eqs. 2.5 and 2.7 at the same time with the relevant boundary conditions. However, in the special case of the conical geometry, one can integrate the radial dependence of the curvature H , and express the bending energy as a function of s solely. Since the curvature diverges as $r \rightarrow 0$, we introduce a cutoff of radius r_0 at the apex and write the bending energy as:

$$E_b[\mathbf{u}] = \frac{a}{2} \int_{\Gamma} ds \kappa^2, \quad (2.12)$$

where $a = \ln(R/r_0)$ contains the dimensional dependency of the system.

Instead of applying the general equations 2.5 and 2.7 to the conical geometry, one can think of applying a variational approach directly to the integrated energy 2.12. However, in general the two processes of Hamiltonian variation and fixing the geometry do not commute [20]. Nevertheless, as Guven and Müller have shown, given that the boundary conditions are symmetrical, it is safe to reverse the order of these operations [14, 20]. As we will see, this procedure will give us an analog of the Euler-Lagrange equation of the Euler Elastica. We should keep in mind that the analogy is only valid for systems with symmetrical boundaries. Otherwise, the analogy breaks down, as one can see in the case of a cone brought down by the gravity [20].

It is convenient to enforce geometrical constraints by a set of Lagrange multipliers [22]. Hence we will be interested in the functional

$$F[\mathbf{u}, \mathbf{t}, \lambda, \Lambda, \mathbf{f}] = \int_{\Gamma} ds \left[\frac{a}{2} (\mathbf{u} \cdot (\mathbf{t} \times \mathbf{t}'))^2 + \frac{\lambda}{2} (\mathbf{u}^2 - 1) + \frac{\Lambda}{2} (\mathbf{t}^2 - 1) + \mathbf{f} \cdot (\mathbf{t} - \mathbf{u}') \right], \quad (2.13)$$

where the Lagrange multiplier functions $\lambda(s)$ and $\Lambda(s)$ enforce the unity of the vectors \mathbf{u} , \mathbf{t} and where \mathbf{f} makes sure that the first of the structure equations 2.10 is satisfied.

Using the equations 2.10, the variations of F with respect to \mathbf{u} and \mathbf{t} are given

by:

$$\begin{aligned}\mathbf{f}' &= -(a\kappa^2 + \lambda)\mathbf{u} + a\kappa\mathbf{n}, \\ \mathbf{f} &= -(\Lambda + 2a\kappa^2)\mathbf{t} - a\kappa'\mathbf{n}.\end{aligned}\tag{2.14}$$

We take the derivative of the equation in the second line of 2.14 and substitute it in the first line. The projection onto \mathbf{t} gives $\Lambda' = -5a\kappa\kappa'$ whose integral gives us Λ as a function of κ up to a constant c :

$$\Lambda = c - \frac{5}{2}a\kappa^2.\tag{2.15}$$

Projection on \mathbf{u} gives $\Lambda + 2a\kappa^2 = -(a\kappa^2 + \lambda)$, hence we determine λ using Eq. 2.15,

$$\lambda = -\frac{a}{2}\kappa^2 - c.\tag{2.16}$$

Finally, the normal projection yields the Euler-Lagrange equation:

$$-a\left(\kappa'' + \frac{1}{2}\kappa^3 + \kappa\right) + c\kappa = 0.\tag{2.17}$$

The constant c in the shape equation is associated with the stress in the surface due to the fixed area constraint, which is in this form, expressed as fixing the arc length.

It is also possible to make directly use of the symmetry of the system to determine the surface. We break the translational symmetry of the system by fixing its apex, but the bending energy is still invariant with respect to three-dimensional rotations. Therefore, the variations of the functional F with respect to an infinitesimal rotation $\delta\mathbf{X} = \mathbf{b} \times \mathbf{X}$ should vanish.

The variation of F can be put in the form:

$$\delta F = - \int ds \frac{d}{ds} [\mathbf{f} \cdot \delta\mathbf{u} + a\kappa(\mathbf{u} \times \mathbf{t}) \cdot \delta\mathbf{t}].\tag{2.18}$$

Under a constant infinitesimal rotation, the variations of \mathbf{u} and \mathbf{t} are specifi-

2. DIPOLES IN THIN SHEETS

cally given by $\delta\mathbf{u} = \mathbf{b} \times \mathbf{u}$ $\delta\mathbf{b} = \mathbf{b} \times \mathbf{t}$. The condition $\delta F = 0$ leads to

$$\frac{d}{ds} [\mathbf{b} \cdot (\mathbf{u} \times \mathbf{f} + a\kappa\mathbf{u})] = 0. \quad (2.19)$$

This requires the term in the parenthesis to be constant, so we put:

$$\mathbf{u} \times \mathbf{f} + a\kappa\mathbf{u} = \mathbf{m}, \quad (2.20)$$

where \mathbf{m} is a constant vector. Recalling Noether's theorem, the vector \mathbf{m} can be identified as the conserved quantity related to the continuous rotational symmetry of the system.

Writing the vector $\mathbf{M} = \frac{\mathbf{m}}{a}$ explicitly in the basis $\{\mathbf{u}, \mathbf{t}, \mathbf{n}\}$ and defining $C = c/a$:

$$\mathbf{M} = \kappa\mathbf{u} + \kappa'\mathbf{t} + \left(\frac{1}{2}\kappa^2 - C\right)\mathbf{n}. \quad (2.21)$$

Its square produces the first integral of the shape equation:

$$M^2 - C^2 = \kappa'^2 + \frac{\kappa^4}{4} + (1 - C)\kappa^2, \quad (2.22)$$

where we used $M = |\mathbf{M}|$. The solution of this equation for an isolated conical point defect is given in [14]. The equilibrium shapes are found to be ruff-like dihedrally symmetric shapes that can be enumerated by the number of folds. This quantized structure arises because of the closure condition, $\kappa(0) = \kappa(s_e) = 0$. The only stable shape is the twofold [16]. The symmetry is broken for cones having a surplus angle larger than $\Psi^{\text{kiss}} = 7.08$. Beyond this value the folds of the stable cone touch each other and the symmetry is broken in favor of skewed cones characterized by repetitive spiral windings with increasing growth [15].

2.2 Dipole defects

To attack the dipole problem, we will first solve the equation 2.22 for open deficit and surplus cones. Their interaction will be through the boundary conditions. In the following, we will express the quantities differing for surplus and deficit part with \pm , where $+$ denotes the surplus cone and $-$ the deficit.

2.2.1 Determination of curvature

Equation 2.22 can be solved for κ in terms of elliptic functions. To see this, we first assume $C < 1$ and define $\lambda^{-2} := 1 - C$. Then Eq. 2.22 can be put in the form:

$$\int_{\Gamma} ds = \int_{\Gamma} \frac{d\kappa}{\sqrt{(M^2 - C^2) - (\frac{1}{4}\kappa^4 + \lambda^{-2}\kappa^2)}}, \quad \text{where } M^2 - C^2 > 0. \quad (2.23)$$

Integrating both sides for a point s on the curve yields

$$s = \frac{\sqrt{2}\lambda}{\sqrt{1+\eta}} \mathcal{F} \left[\sin^{-1} \left(\frac{\kappa\lambda}{\sqrt{2(\eta-1)}} \right), \frac{1-\eta}{1+\eta} \right], \quad (2.24)$$

where $\eta = \sqrt{1 + (M^2 - C^2)\lambda^4} \geq 1$. The function $\mathcal{F}[[s, k]]$ is the elliptic function of the first kind with the parameter k [23].

Inverting it, we obtain

$$\kappa(s) = \frac{\sqrt{2}\sqrt{-1+\eta}}{\lambda} \operatorname{sn} \left[\frac{\sqrt{1+\eta}}{\sqrt{2}\lambda} s, \frac{1-\eta}{1+\eta} \right], \quad (2.25)$$

where the function $\operatorname{sn}[[s, k]]$ is the sine of the Jacobi amplitude $\operatorname{am}[[s, k]]$ with parameter k [23].

The curvature of the dipole defect has two distinct forms on two different parts: the curvature of the conical part with the deficit angle has one extremum while the curvature of the part with the surplus angle has three. Hence specifying the number of extrema $n_+ = 3$ and $n_- = 1$ and requiring $\kappa(0) = \kappa(L) = 0$, we obtain the constant λ as

$$\lambda_{\pm} = \frac{\sqrt{1+\eta} L_{\pm}}{2n_{\pm}\sqrt{2} \mathcal{K} \left[\frac{1-\eta}{1+\eta} \right]}, \quad (2.26)$$

where $\mathcal{K}[[k]]$ denotes the complete elliptic integral of the first kind [23]. We will assume that the extremum of the deficit cone will be a maximum of the curvature. For the surplus part, we will set the three extrema to be two minima and one

2. DIPOLES IN THIN SHEETS

maximum. Putting $k := \frac{1-\eta}{1+\eta} \in [-1, 0]$, we get the curvature on both parts:

$$\kappa_{\pm}(s) = \mp \frac{4n_{\pm}\sqrt{-k}\mathcal{K}[[k]]}{L_{\pm}} \operatorname{sn} \left[\frac{2n_{\pm}\mathcal{K}[[k]]}{L_{\pm}} s, k \right]. \quad (2.27)$$

The solutions with opposite extrema can be obtained by rotating the found shapes by an angle of π around the dipole vector, which is indeed Eq. 2.27 with opposite signs.

Since $\lambda^{-2} := 1 - C$, one has:

$$C_{\pm} = 1 - \frac{4n_{\pm}^2(1+k)\mathcal{K}[[k]]^2}{L_{\pm}^2}. \quad (2.28)$$

A similar calculation, done for $C > 1$, gives the same expressions for $\kappa_{\pm}(s)$ and C , but now with the definition $k = \frac{1+\eta}{1-\eta} < -1$.

At $s = 0$, the quadrature 2.22 reduces to $M = \sqrt{\kappa'(0)^2 + C^2}$, which allows to determine the magnitude of the torque vector \mathbf{M} in terms of k and L_{\pm} :

$$M_{\pm} = \sqrt{-\frac{64n_{\pm}^4 k \mathcal{K}[[k]]^4}{L_{\pm}^4} + \left[1 - \frac{4n_{\pm}^2(1+k)\mathcal{K}[[k]]^2}{L_{\pm}^2} \right]^2}. \quad (2.29)$$

The only parameters left undetermined are k and L . In the next section, the boundary conditions at \mathbf{i} and \mathbf{Ri} will help us to derive implicit expressions that specify the values of these parameters.

2.2.2 Boundary conditions

Even though the vector \mathbf{M}_{\pm} is conserved in each of the cones, it is not necessarily aligned with the vertical axis \mathbf{z} . Let the vector \mathbf{j} denote the direction along which the vector \mathbf{M} is aligned, with $\mathbf{M} = M\mathbf{j}$ and $M > 0$ (see Fig. 2.4a). The mirror symmetry requires that the vector \mathbf{M} should lie in the plane defined by the dipole vector \mathbf{D} and the vertical axis \mathbf{z} .

The vector \mathbf{i} denotes the generator along one boundary, *i.e.*, $\mathbf{i} = \mathbf{u}|_{s=0}$. The other generator is given by $\mathbf{Ri} = \mathbf{u}|_{s=L_{\pm}}$ where \mathbf{R} represents a reflection in the mirror plane.

We will parametrize the vector \mathbf{i} of each cone by two angles: the angle $\beta \in$

$\{0, \pi\}$ it makes with the dipole vector and the angle $\alpha \in \{0, \pi\}$ the \mathbf{Di} plane makes with the mirror plane \mathbf{Dz} (see Fig. 2.4b). While each cone has its own β , the angle α is the same for both. When the dipole charge is $\Psi = 0$, the sheet is flat and $\alpha = \pi/2$. Given the charge Ψ and the ratio D/R , the geometries will be completely determined by α , which will be set by the minimum of the bending energy.

The length L of the curve Γ is given by the angles β and Ψ :

$$L_{\pm} = 2\pi - 2\beta_{\pm} \pm \Psi. \quad (2.30)$$

Since the arc length of the deficit part cannot be negative, the value of Ψ can never be larger than 2π . For a given D , this sets an upper limit for the strength of the “charge-neutral” dipole. Therefore, the dipole limit $\Psi \rightarrow \infty$, $D \rightarrow 0$ with $\Psi D = \text{const.} > 0$ does not exist for elastic sheets, breaking the analogy to the electrostatic dipoles.

We will use the projections of the constant vector \mathbf{M} onto the local trihedron $(\mathbf{u}, \mathbf{t}, \mathbf{n})$ to determine β in terms of fixed angles Ψ and α (see again 2.4).

The direction of \mathbf{u} in Euclidean space can be specified by the azimuthal angle φ , measured with respect to the vector \mathbf{i} and the polar angle ϑ measured with respect to the vector \mathbf{j} . Projecting 2.21 onto \mathbf{u} , we obtain

$$M(\mathbf{j} \cdot \mathbf{u}) = M \cos \vartheta = \kappa, \quad (2.31)$$

which relates the polar angle ϑ to the curvature κ . Eqn. 2.31 implies that the radial lines where κ vanishes lie on the plane perpendicular to \mathbf{M} , *i.e.*, $\mathbf{i} \perp \mathbf{j}$ and $R\mathbf{i} \perp \mathbf{j}$. It also implies that above this plane defined by the vectors \mathbf{i} and $R\mathbf{i}$ the curvature κ is strictly positive, and below the plane, it is strictly negative.

The projection of \mathbf{M} onto \mathbf{t} gives the derivative of Eqn. 2.31. The last projection onto \mathbf{n} returns

$$M(\mathbf{j} \cdot \mathbf{n}) = M \varphi' \sin^2 \vartheta = \frac{1}{2} \kappa^2 - C, \quad (2.32)$$

2. DIPOLES IN THIN SHEETS

which relates the azimuthal angle φ to the integrated curvature

$$\varphi' = \frac{1}{M \sin^2 \vartheta} \left(\frac{1}{2} \kappa^2 - C \right) = \frac{\frac{1}{2} \kappa^2 - C}{M \left(1 - \frac{\kappa^2}{M^2} \right)} = \frac{1}{2} M \left[\frac{M^2 - 2C}{M^2} \left(\frac{1}{1 - M^{-2} \kappa^2} \right) - 1 \right]. \quad (2.33)$$

It is known that [23]

$$\int \frac{ds}{1 - b \operatorname{sn}^2 \llbracket c s, k \rrbracket} = \frac{1}{c} \Pi \llbracket b, \operatorname{am} \llbracket c s, k \rrbracket, k \rrbracket, \quad (2.34)$$

where Π is the elliptic integral of the third kind. Equations 2.33 and 2.34 combine to

$$\begin{aligned} \varphi_{\pm}(s) &= \int_0^s dt \varphi'(t) \\ &= \frac{M_{\pm}^2 - 2C_{\pm}}{2M_{\pm}} \frac{L_{\pm}}{2n_{\pm} \mathcal{K} \llbracket k \rrbracket} \\ &\quad \Pi \left[\left[\frac{16n_{\pm}^2 (-k) \mathcal{K} \llbracket k \rrbracket^2}{M_{\pm}^2 L_{\pm}^2}, \operatorname{am} \left[\left[\frac{2n_{\pm} \mathcal{K} \llbracket k \rrbracket s}{L_{\pm}}, k \rrbracket, k \rrbracket \right] - \frac{M_{\pm}}{2} s \right. \right. \end{aligned} \quad (2.35)$$

We introduce a Cartesian coordinate system on the surplus defect. The unit vector \mathbf{x} , parallel to the dipole vector \mathbf{D} is directed away from the ridge (see Fig. 2.4). Combined with the vector \mathbf{z} and the vector perpendicular to both, \mathbf{y} , this defines a right-handed basis. A similar coordinate system can be attached to the deficit defect with the unit vector \mathbf{x} anti-parallel to \mathbf{D} .

With these definitions, the trihedron $(\mathbf{u}, \mathbf{t}, \mathbf{n})$ at $s = 0$ is then given by:

$$\begin{aligned} \mathbf{i} &\equiv \mathbf{u}_{s=0} = -\cos \beta \mathbf{x} + \sin \beta \mathbf{i}_{\perp}, \\ \mathbf{t}_{s=0} &= \sin \beta \mathbf{x} + \cos \beta \mathbf{i}_{\perp}, \\ \mathbf{n}_{s=0} &= -\cos \alpha \mathbf{y} + \sin \alpha \mathbf{z}, \end{aligned} \quad (2.36)$$

where $\mathbf{i}_{\perp} = -\sin \alpha \mathbf{y} - \cos \alpha \mathbf{z}$. We express the unit vector \mathbf{j} in terms of the Cartesian basis $(\mathbf{x}, \mathbf{y}, \mathbf{z})$:

$$\mathbf{j} \sim \frac{\mathbf{i} \times \mathbf{Ri}}{|\mathbf{i} \times \mathbf{Ri}|} = \frac{\cos \alpha \sin \beta \mathbf{x} - \cos \beta \mathbf{z}}{\sqrt{1 - \sin^2 \alpha \sin^2 \beta}}. \quad (2.37)$$

C_+	$\beta < \frac{\pi}{2}$	$\beta > \frac{\pi}{2}$
$\alpha < \frac{\pi}{2}$	-	+
$\alpha > \frac{\pi}{2}$	+	-

C_-	$\beta < \frac{\pi}{2}$	$\beta > \frac{\pi}{2}$
$\alpha < \frac{\pi}{2}$	+	-
$\alpha > \frac{\pi}{2}$	-	+

Table 2.1: The sign of C depends on the value of α and β .

According to equation 2.21, the projection of $\mathbf{M} = M\mathbf{j}$ onto \mathbf{t} has to be equal to κ'_\pm . Following the definition of signs given in Eq. 2.27 the sign of \mathbf{j} follows as

$$\mathbf{j}_\pm^{\alpha < \frac{\pi}{2}} = \mp \frac{\mathbf{i} \times \mathbf{Ri}}{|\mathbf{i} \times \mathbf{Ri}|}, \quad \text{and} \quad \mathbf{j}_\pm^{\alpha > \frac{\pi}{2}} = -\mathbf{j}_\pm^{\alpha < \frac{\pi}{2}}, \quad (2.38)$$

since we have defined $M > 0$. Then for all $\alpha \in \{0, \pi\}$, the projection at $s = 0$ yields

$$\frac{M_\pm |\cos \alpha|}{\sqrt{1 - \sin^2 \alpha \sin^2 \beta_\pm}} = \frac{8n_\pm^2 \sqrt{-k} \mathcal{K}[[k]]^2}{L_\pm^2}. \quad (2.39)$$

We project \mathbf{M} onto \mathbf{n} at $s = 0$:

$$C_\pm^{\alpha < \frac{\pi}{2}} = \mp \frac{M_\pm \sin \alpha \cos \beta_\pm}{\sqrt{1 - \sin^2 \alpha \sin^2 \beta_\pm}}, \quad \text{and} \quad C_\pm^{\alpha > \frac{\pi}{2}} = -C_\pm^{\alpha < \frac{\pi}{2}}. \quad (2.40)$$

As it is listed in Tab. 2.1, the sign of C depends on the value of α and β according to the relation:

$$\text{sign } C_\pm = \mp \text{sign} \left[\left(\frac{\pi}{2} - \alpha \right) \left(\frac{\pi}{2} - \beta \right) \right]. \quad (2.41)$$

In order to write $\varphi(s)$ in terms of α and β , we define the angle γ between \mathbf{i} and \mathbf{Ri} :

$$\cos \gamma = \mathbf{i} \cdot \mathbf{Ri} = \cos^2 \beta + \cos(2\alpha) \sin^2 \beta, \quad \text{where } \gamma \in \{0, \pi\}. \quad (2.42)$$

The range of the azimuthal angle $\phi = \varphi(L)$ on the \mathbf{iRi} plane depends on this angle γ in a nontrivial way (see Tab. 2.2).

Finally, with the help of Eqn. 2.35 we find the following expression for ϕ :

$$\phi_\pm = \varphi_\pm(L_\pm) = L_\pm \left(\frac{M_\pm^2 - 2C_\pm}{2\mathcal{K}[[k]]M_\pm} \Pi \left[\left[\frac{16n_\pm^2(-k)\mathcal{K}[[k]]^2}{M_\pm^2 L_\pm^2}, k \right] - \frac{M_\pm}{2} \right) \right), \quad (2.43)$$

2. DIPOLES IN THIN SHEETS

ϕ_+	$\beta < \frac{\pi}{2}$		$\beta > \frac{\pi}{2}$	
	$\phi_+ < 0$	$\phi_+ > 0$	$\phi_+ > 0$	$\phi_+ < 0$
$\alpha < \frac{\pi}{2}$	n. p.	$2\pi - \gamma$	$2\pi - \gamma$	self-contact
$\alpha > \frac{\pi}{2}$	self-contact	γ	γ	n. p.

ϕ_-	$\beta < \frac{\pi}{2}$		$\beta > \frac{\pi}{2}$	
	$\phi_- < 0$	$\phi_- > 0$	$\phi_- > 0$	$\phi_- < 0$
$\alpha < \frac{\pi}{2}$	$\gamma - 2\pi$	γ	γ	n. p.
$\alpha > \frac{\pi}{2}$	n. p.	n. f.	n. f.	n. f.

Table 2.2: The functional dependence of $\phi_{\pm} = \varphi_{\pm}(L_{\pm})$ on the angle γ depends on the sign of ϕ_{\pm} and the value of α and β (see text). Shapes with both $C_{\pm} < 0$ and $\phi_{\pm} < 0$ are not possible (= n. p. in the table). For the deficit cone one does not find solutions if $\alpha > \frac{\pi}{2}$ (= n. f. in the table).

where we have used that $\text{am} \llbracket 2n_{\pm}\mathcal{K}\llbracket k \rrbracket, k \rrbracket = n_{\pm}\pi$ for $k < 1$.

Depending on the configurations of vectors \mathbf{i} , \mathbf{Ri} , and \mathbf{j} the value of ϕ can be positive or negative. If ϕ is positive, it is equal to $\phi = \gamma$ if \mathbf{j} and $\mathbf{i} \times \mathbf{Ri}$ are parallel, or to $\phi = 2\pi - \gamma$ if the two vectors are anti-parallel (see Eqn. 2.38) Whereas when ϕ is negative, it gives $\phi = \gamma - 2\pi$ if \mathbf{j} and $\mathbf{i} \times \mathbf{Ri}$ are parallel, and $\phi = -\gamma$ if they are anti-parallel.

The sign of ϕ depends on the sign of C (see Tab. 2.1) in a tricky way. When C is negative, by Eqn. 2.33, $\varphi'(s)$ is positive for all $s \in \{0, L_{\pm}\}$ and consequently $\phi > 0$ in this case. Hence both C and ϕ cannot be negative at the same time (= n.p. in Tab. 2.2). For C positive, the situation is more complicated. Now φ' is always negative at $s = 0$, but if C is not too big, ϕ changes sign along the path Γ . The projections of \mathbf{M} at $s = L/2$ where the curvature κ is maximal is helpful to determine C^{cr} , where ϕ changes sign: ϕ_{\pm} changes sign when $\vartheta(L/2) = 0$, *i.e.*, when $M^{\text{cr}} \stackrel{2.31}{=} \kappa(L/2)$ and $2C^{\text{cr}} \stackrel{2.32}{=} \kappa^2(L/2) = (M^{\text{cr}})^2$.

At this point we have everything to calculate β_{\pm} as a function of α . Given Ψ and α , one can now determine the shape of each conical section using Eqn. 2.39 and the condition on ϕ (see Eq. 2.43 and Tab. 2.2).

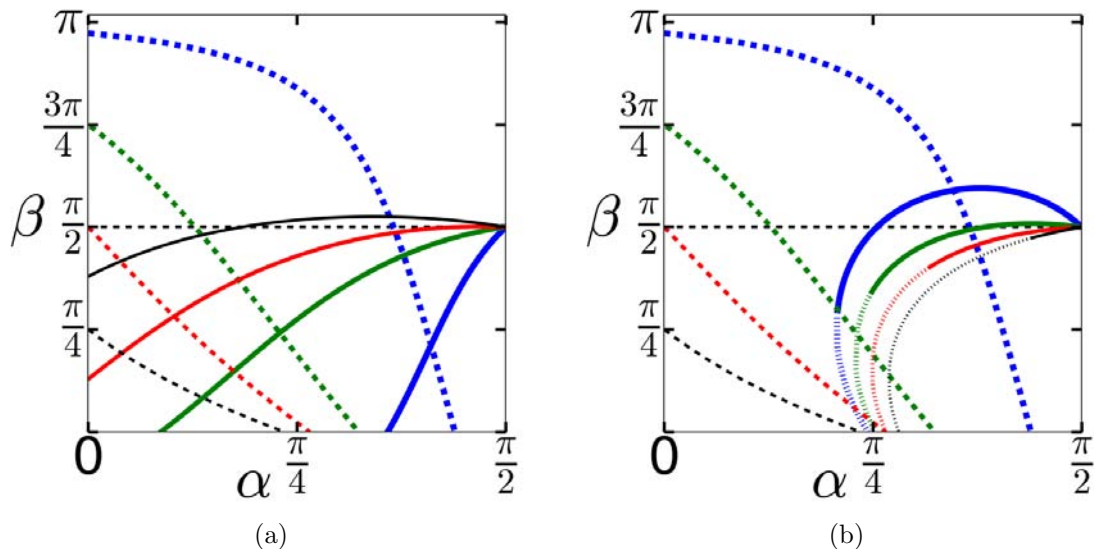


Figure 2.5: The angle β as a function of α for (a) the torque dipole and (b) the force dipole, with strength $\Psi = \frac{\pi}{18}$ (thick blue curves), $\frac{\pi}{2}$ (green curves), π (red curves), and $\frac{3\pi}{2}$ (thin black curves). The dashed curves show $\beta_-(\alpha)$, the solid curves $\beta_+(\alpha)$. Shapes where the surplus part of the force dipole intersects with the planar regions correspond to the dotted part of the curves for $\beta_+(\alpha)$. For the torque dipole, intersections occur for higher values of Ψ ($\Psi \gtrsim 5.14$).

2.2.3 Results

In the previous section we derived the necessary tools to determine β_{\pm} as a function of α using the projections of \mathbf{M} onto the local trihedron $(\mathbf{u}, \mathbf{t}, \mathbf{n})$ ¹. In Fig. 2.5a, the results for the torque dipole are shown for four different values of Ψ . For a fixed Ψ , the deficit cone admits solutions for β_- up to a maximum value of α (dashed curves in Fig. 2.5a). For the surplus part, there is similarly a minimum value of α below which no solution for β_+ can be found (solid curves in Fig. 2.5a). In the limit of vanishing strength, $\Psi \rightarrow 0$, both of the limits on α go to $\frac{\pi}{2}$, which corresponds to a planar sheet. Note that the case $\alpha > \frac{\pi}{2}$ means a sign inversion in the curvature $\kappa_{\pm}(s)$, and implies a rotation of the equilibrium solution around the dipole vector \mathbf{D} by an angle of π . Such an operation does not affect the value of the angle β . Therefore the solutions of β_{\pm} for $\alpha > \frac{\pi}{2}$ are

¹Instead of examining the problem in its full non-linear glory one can also confine oneself to a harmonic approximation –see appendix B

2. DIPOLES IN THIN SHEETS

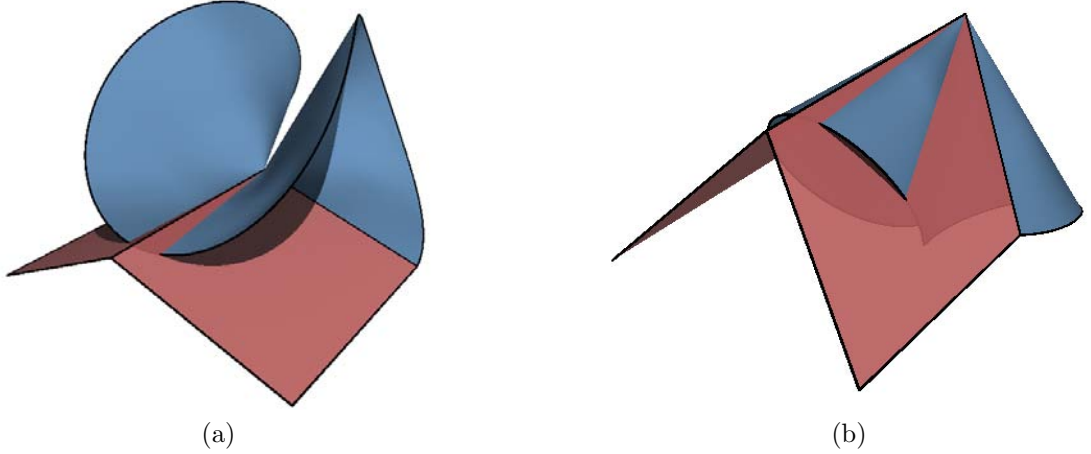


Figure 2.6: Surplus cone touching the planar regions of the dipole. (a) In the case of the torque dipole, the cone can penetrate through the dipole vector. (b) In case of the force dipole, the cone can touch the planar regions from below.

simply given by the mirror reflection of the plot at $\alpha = \pi/2$ or equivalently by $\beta_{\pm}(\pi - \alpha) = \beta_{\pm}(\alpha)$.

Similar relations holds for the force dipole. For $\alpha < \frac{\pi}{2}$, the curves of β_- of the deficit cone are the same as those of the torque dipole. With the chosen sign convention of $\kappa_+(s)$, the solutions for the surplus cone of the force dipoles can be found when $\alpha > \frac{\pi}{2}$. By rotating these solutions around \mathbf{D} by an angle of π , we obtain the plot Fig. 2.5b similar to the torque dipole solution Fig. 2.5a. Once again, the values of α are bounded by a lower limit, which is now determined according to the requirement that the equilibrium surfaces should not self-contact. In fact, three types of self-contacts are possible:

- i. the surplus cone can touch the planar regions of the dipole (see Fig. 2.6),
- ii. adjacent folds of the surplus cone can touch each other,
- iii. when D/R is too small, surplus and deficit cones can touch each other in the force dipole configuration.

We assume that the ratio D/R is sufficiently large, so we exclude case [iii](#). But we have to still consider the cases [i](#) and [ii](#). We have found numerically that the

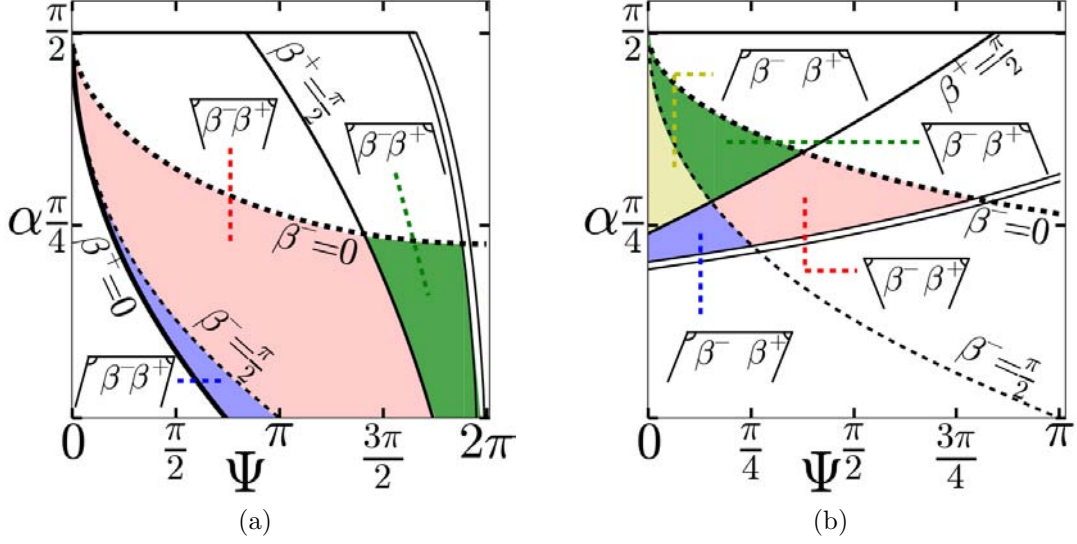


Figure 2.7: The shaded zone represents those values of (Ψ, α) for which values of β_+ and β_- , and thus solutions, may be found for (a) the torque dipole and (b) the force dipole. Different colors represent qualitatively different cases. For example, in the blue region $\beta_- > \frac{\pi}{2}$ and $\beta_+ < \frac{\pi}{2}$. The double curve indicates shapes where the surplus part touches (a) the dipole vector, (b) the planar regions of the dipole (see Fig. 2.6).

surplus cone touches the planar regions **i** before it touches itself **ii**. In Fig. 2.5b, the solutions with self-intersection are marked with dotted lines. The shapes with self-contact are expected to break mirror symmetry, as it is observed in simulations of the monopole [15].

So far, we derived the solutions for the conical parts separately. In order to construct the full dipole shape, we combine the isolated solutions we have found so far. The only requirement is that the angle α has to be the same for both parts. Hence, for a given Ψ , we compute the range of α for which an equilibrium solution exists for both part of the dipole. The results are plotted in Fig. 2.7 where double curves indicate the self-contact of the dipole shapes.

To extract the value of α predicted by our theoretical model, we calculate the total bending energy of the system and minimize it. Neglecting the effect of the width of the sheet and the size of the dipole vector D , we simply write the total energy as the sum of the normalized bending energy of deficit and surplus parts:

2. DIPOLES IN THIN SHEETS

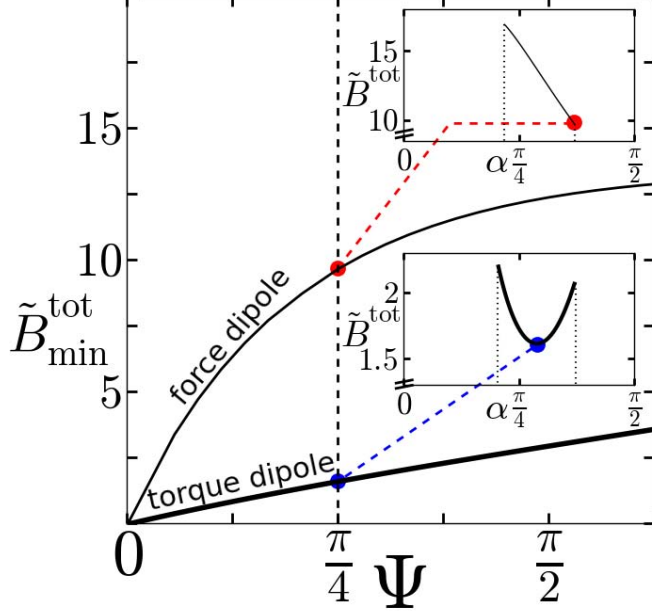


Figure 2.8: Minimal bending energy $\tilde{B}_{\min}^{\text{tot}}$ as a function of Ψ for the torque (thick curve) and the force dipole (thin curve). Insets: Total bending energy \tilde{B}^{tot} of each dipole as a function of α for $\Psi = \frac{\pi}{4}$.

$$\tilde{B}^{\text{tot}} = \tilde{B}_+ + \tilde{B}_-,$$

$$\text{with } \tilde{B}_{\pm} = \int_0^{L_{\pm}} ds \kappa_{\pm}^2 / 2 = 8 \frac{n_{\pm}^2}{L_{\pm}} \mathcal{K}[[k]] (\mathcal{E}[[k]] - \mathcal{K}[[k]]), \quad (2.44)$$

where the function $\mathcal{E}[[k]]$ is the complete elliptic integral of the second kind [23]. In the insets of Fig. 2.8 we show \tilde{B}^{tot} as a function of α for $\Psi = \frac{\pi}{4}$. The circular dots in the insets mark the angle α_{\min} , where we find the minimum $\tilde{B}_{\min}^{\text{tot}}$ for both dipoles. Interestingly, at this minimum, the sum $\mathbf{M}^{\text{tot}} = \mathbf{M}_+ + \mathbf{M}_-$ of the conserved torque vectors is vertical. The generic behavior of \tilde{B}^{tot} is the same for other values of Ψ : for the torque dipole, \tilde{B}^{tot} is always convex, the minimum lies somewhere in the middle of the curve. For the force dipole, the minimum is always at the upper limit where $\beta_- = 0$.

Experimental observations on the paper dipole (see Fig. 2.3) can be understood in the light of our theoretical results. The first observation is that the

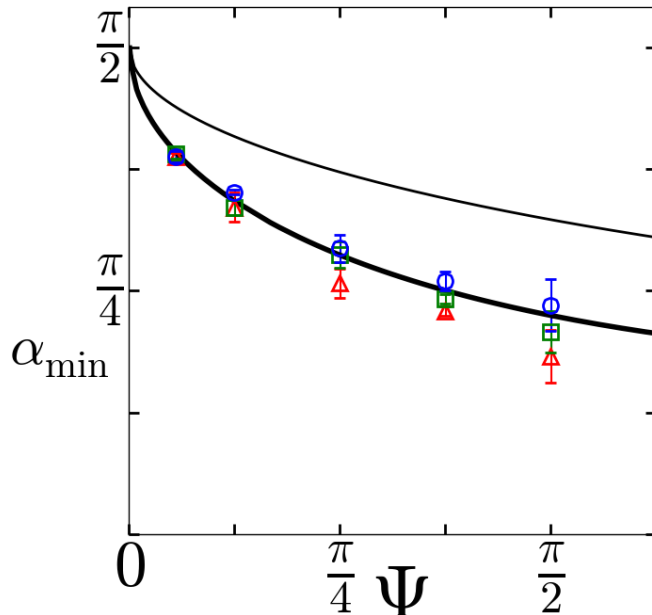


Figure 2.9: Dependence of the angle α_{\min} on Ψ determined semi-analytically (solid curves) for both dipoles, and experimentally for the torque dipole using an A4 sheet of paper with dipole vectors $D = 2$ cm (red triangles), 4 cm (green squares), and 6 cm (blue circles). Points and error bars are mean and standard deviation of four measurements.

conversion from a force dipole into a torque dipole seems to be much easier than the conversion from a torque dipole into a force dipole. This is consistent with the difference in the energy of the two states: For all Ψ , the energy \tilde{B}^{tot} of the torque dipole is lower than that of the force dipole (see Fig. 2.8). This implies the existence of an energy barrier between the two states, since both conformations are stable with respect to small deformations.

It is also possible to compare the theoretical value of α_{\min} to experiments (see Fig. 2.9). According to the theory, the angle α of the force dipole will be as large as possible. However, in contrast to our analysis, the real physical sheet can also stretch outside of the singularities, and thereby it can increase the dihedral angle even further. The result is a ridge which is not entirely straight, as mentioned earlier. In the vicinity of the ridge, the angle α_{\min} seems to be approximately equal to $\frac{\pi}{2}$, but its exact value depends on where along the ridge it is measured.

2. DIPOLES IN THIN SHEETS

The angle α_{\min} of the paper model of the torque dipole, is relatively constant along the ridge. Hence, it is easier to measure its value and compare it to the theory (see Fig. 2.9). For the experiments, we chose five different strengths for Ψ and three for the dipole length D . For each set of (Ψ, D) , we constructed four paper models of the dipole. We measured the angle α_{\min} for each paper model using one of two different methods. The first one consists of placing a compass on the ridge and measuring the angle of the compass with a protractor. In the other one, we measured $\tan(\alpha_{\min})$, which is given by the ratio of half the wingspan of the model to the vertical height of the ridge.

The experimental and theoretical results are plotted in Fig. 2.9. The experimental points show that α_{\min} increases with D for fixed Ψ , a dependence that our model does not consider. However, the theory explains well the functional dependence of α_{\min} on the dipole strength Ψ .

2.3 Conclusion

As a natural extension of monopole defects in elastic sheets, we have constructed paper models of dipole defects. We observed two stable local minima of bending energy: Away from its ridge, the force dipole has a geometry similar to a well-known fundamental component of crumpling [11], whereas the torque dipole bears similarities to a numerically-generated buckled dislocation in a crystalline sheet [18].

In order to carry out analytical calculations, we assumed that the system can be decomposed into two conical singularities joined by flat parts. This assumption, as crude as it seems at first sight, explains the non-trivial dipole shapes surprisingly well.

Besides being an important step in the modeling of growth induced defects, the torque dipole also seems to be a potentially useful element in lightweight load-bearing structures, due to its rigidity. For this purpose, it is necessary to investigate the far-field asymptotic geometry of both dipoles.

The next step in an exploration of the multipole expansion will involve accommodating sheets with more than two defects. One possible analytical strategy can be to focus first on the conformal geometry, and then linearize the geometry

around the singularities. For an arbitrary combination of deficits and surpluses, a numerical method is also a promising candidate.

2. DIPOLES IN THIN SHEETS

Chapter 3

Fluid membrane invaginations

Aside from growth (see chapter 2), external forces and constraints can play a crucial role in the shaping of biological membranes. A well studied example is the gastrulation within a surrounding egg shell [24]. For many of the eukaryotic cell structures this kind of shape formation is the main ingredient for correct functioning. The endoplasmic reticulum (ER) constitutes one of the most important examples with all its tubes and cisternae forming a continuous labyrinth of lipid membranes [25]. It plays a central role in biosynthesis; almost all lipids and proteins a cell requires are produced in the lumen of the ER. It also stores calcium ions, thus acting as a reservoir of Ca^{2+} and participates in the regulation of cell signaling [26].

In the prokaryotic world, the counterparts of the membrane regulation exist as well. The purple phototropic bacterium, *Rhodobacter sphaeroides*, increases its surface area in order to multiply the exploitation of solar energy [27]. Upon biogenesis of the membrane, high curvature domains are initiated on the cytoplasmic membrane of the bacteria first. The following budding process gives rise to free intracytoplasmic membrane vesicles which are fully functional in converting solar energy to ATP. Since they are autonomous, these structures can be considered as bacterial organelles to some extent.

Maybe it is the mitochondrion which constitutes the best example of the interplay between structure and function. By effectively remodeling its internal folded structure, the inner membrane of the mitochondrion controls its capacity of ATP synthesis [28]. The alteration of this dynamical and subtle mechanism is

3. FLUID MEMBRANE INVAGINATIONS

closely linked to numerous diseases [29].

In this chapter, we will present a simple mechanical scenario as the prototype of the generation of membrane invaginations. Our model will assume the fluidity of the membrane. Before we present our model and its implications, we will briefly review the structure of the mitochondria and their lipid membranes as a representative system. However, the model we consider is not only valid for fluid lipid bilayer membranes, it can also be relevant for soft tissues as long as in-plane shear forces can equilibrate on time scales smaller than growth [30].

3.1 Mitochondria

Mitochondria are the energy plants of eucaryotic cells. Besides producing ATP through a complex procedure called cellular respiration (including processes such as oxidative phosphorylation, Krebs cycle, and electron transport chain), they take part in metabolic functions like heme biosynthesis, biogenesis of Fe/S clusters and cell death [29].

Mitochondria are dynamic organelles, able to divide and to fuse depending on the needs of the cell. Their size varies in the micrometer range, with a diameter of around $0.5\mu\text{m}$ and length $1 - 10\mu\text{m}$. The shape and the number of mitochondria in a cell are controlled by their relative rate of fusion and fission. They can have a variety of different shapes ranging from small spheres to long tubes. If, in a given moment, there is more fusion than fission, mitochondria are mostly long and highly interconnected. On the other hand, if fission exceeds fusion, they are numerous and in the shape of small spheres or short nodes. As a consequence of this dynamic picture, their number changes from several to hundreds in a cell where they are attached to the cytoskeleton.

Mitochondria are bounded by two layers of phospholipid membranes: **the outer membrane** and **the inner membrane**. The outer membrane draws the contour of the organelle hence defines the overall shape. In contrast with the shape diversity *in vivo*, mitochondria are usually spherical or ellipsoidal *in vitro* [28]. The inner membrane has a larger surface area than the outer membrane so it is folded into the matrix, the protein rich aqueous environment that the inner membrane surrounds [28].

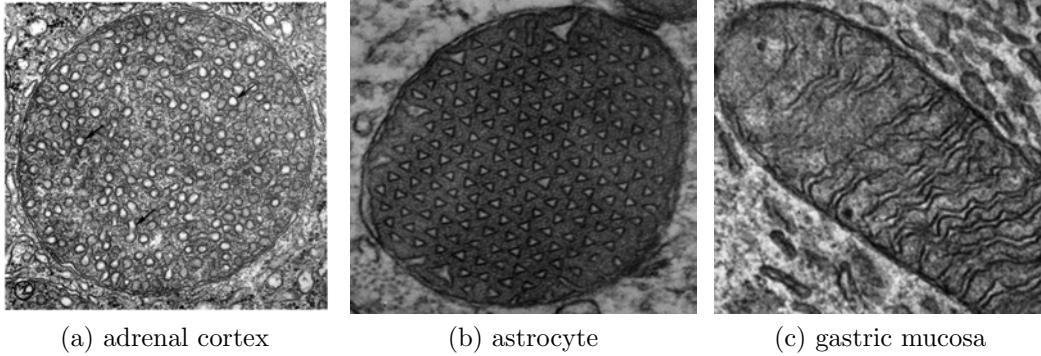


Figure 3.1: Electron tomography images for different types of cristae from [33], [34], and [35] respectively.

These convolutions of the inner membrane were first observed by electron microscopy studies of Palade [31] and Sjöstrand [32]. They have proposed two different models to explain the structure of mitochondria. The baffle model of Palade described the outer membrane as a regular eukaryotic membrane containing voltage dependent anion channels. According to this model, the inner membrane, which is of prokaryotic origin forms random invaginations called *cristae mitochondriales*. In addition to the Palade’s model, the septa model of Sjöstrand described a third membrane dividing the matrix into many compartments.

The developments in imaging technology with the use of electron tomography enhanced the quality of mitochondria images and pushed researchers to revisit a model first proposed in 1966. The model of Daems and Wisse [36] states that the cristae are not simple convolutions but tubular or lamellar structures, connected to the inner membrane by narrow necks called *crista junctions*. So, in this model the inner mitochondrial membrane has three domains: the **inner boundary membrane** apposed to the outer membrane, **crista junctions** and **cristae** [37].

For different cell types, it is possible to observe completely different geometries of inner mitochondrial invaginations. Figure 3.1 represents electron microscopy images of adrenal cortex¹, astrocyte², and gastric mucosa cells, depicting re-

¹Adrenal cortex constitutes the perimeter of the adrenal gland situated at the top of the kidneys. It is mainly responsible for the stress response through the production of various hormones.

²Astrocytes are supporting cells of the nervous system. They are at least five times more numerous than neurons in human brain.

3. FLUID MEMBRANE INVAGINATIONS

spectively spherical, triangular and lamellar crista. While the geometry of the invaginations shows a great diversity, the crista junctions seem to share a uniform size and shape [29]. They are usually narrow circular or ellipsoidal tubes with a diameter in the range of 12nm to 40nm. On the other hand, the length in general varies between 30 to 50 nm except few species like *Neurospora Crassa* for which lengths of 150 - 200 nm are also observed [38].

Experimental studies of the inner membrane suggest that the ultrastructure of the inner membrane is a result of a cooperation involving increase in surface area, lipid composition (such as the concentration of cardiolipin in the membrane [39]) and protein interactions [40, 41]. Before we proceed to our model, we need to understand the intricate details of the biological membrane. Thus, we can see the way of reducing its complexity.

3.2 Biological membranes

The biological membrane is the frontier of the cell, the unit of high level life. Defining the physical limits of the cell and in eukaryotes that of the organelles as well, it confines all the machinery that make the cycles of production, consumption and reproduction possible. But it is not only a simple contour, it behaves more like a border with customs, it regulates all mechanical and chemical communication of the cell with the outside world. It senses and bears the pressure, receives and sends messages, conducts and stops flows.

It achieves all of duties thanks to its macromolecular structure of high complexity. Its permeability is regulated by specialized pores such as ion channels or aquaporins (see chapter 11 in [25]) and it palpates its environment using contact devices such as cadherin and integrin (see chapter 19 in [25]).

3.2.1 Molecular structure of biological membranes

It is known since the 1920's that the cell membrane is composed of a double layer of lipid molecules. Gorter and Grendel showed that the lipids extracted from an erythrocyte membrane form a monolayer with an area doubling the surface of the cell [42]. In 1972, Singer and Nicolson [43] proposed the **fluid mosaic**

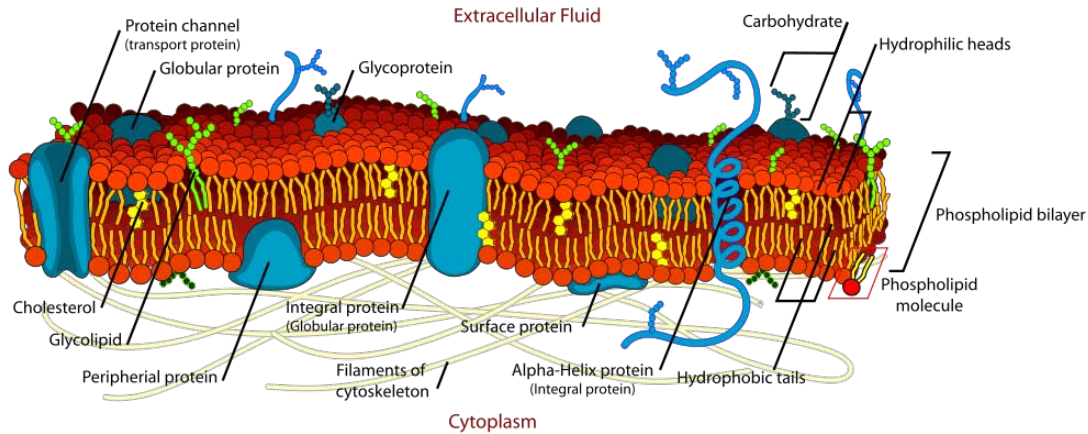


Figure 3.2: Illustration of the cell membrane with different types of membrane proteins embedded into the lipid matrix [44].

model describing the cell membrane as a two-dimensional liquid of lipids in which proteins are dissolved (see fig. 3.2). The membrane's molecular architecture is governed by the chemical properties of the lipid molecules.

Lipids are amphiphilic molecules. They consist of two parts: a negatively charged **hydrophilic** head which is highly soluble in water and a **hydrophobic** tail with two hydrocarbon chains. In aqueous solution, this polar structure of lipid molecules results in a peculiar behavior: the tail tries to be isolated from the water molecules whereas the head tends to be oriented towards the solution. Above a critical concentration in aqueous environment, the lipid molecules self-assemble to satisfy the needs of both parts.

Different types of lipids can be identified with respect to their head groups, the length of the hydrocarbon chains, the number of unsaturated bonds (double C=C bonds) within the chains, and the chemistry of the backbone binding the head to the tail [45, 46]. The chemical details of a lipid molecule determine how it interacts with other lipid molecules, and hence the morphology of lipid self-assemblies. Usually, these assemblies of lipids are classified with respect to the geometry they adopt: Micelle, monolayer, planar bilayer and curved bilayer. Of these, the curved bilayers, which are capable to form vesicles, are of particular interest since they constitute an experimental model of the cell membrane.

A typical phase diagram of a lipid vesicle as a function of water concentration

3. FLUID MEMBRANE INVAGINATIONS

and temperature possesses two states. At low temperatures, the bilayer forms a two-dimensional gel with a crystalline structure. However, at biologically relevant temperatures, it makes a transition into a liquid-crystalline state. In the latter case, the lipid bilayer behaves as a two-dimensional liquid, the molecules are free to move in the surface. A lipid molecule in the liquid-crystalline state would diffuse the length of a cell of $10\mu\text{m}$ diameter in 25s [46]. This property of the lipid membrane makes it a peculiar material that cannot resist static shear deformations.

3.2.2 Membrane proteins

Whereas the lipid molecules play the foremost role in the structure, they are supported by the membrane proteins, long polypeptide chains that undertake most of the functions of the membrane. Since proteins are usually complex macromolecules, their structure is characterized by four levels of organization. The **primary structure** of a protein refers to the linear amino acid sequence. The interactions of nearby amino acids result in local three-dimensional conformations, specifically α *helices*, β *sheets* and *turns*. This is called the **secondary structure**. The **tertiary structure** corresponds to the overall three-dimensional conformation, that combines helices, sheets and turns to one final form. Some proteins have more than one polypeptide chain. For instance, the F_1F_0 -ATP synthase complex, the protein responsible for the ATP synthesis in the organelle, is composed of 13 subunits. This highest level of organization with more than one polypeptide unit is called the **quaternary structure**.

Depending on how they are situated in the membrane, membrane proteins are divided into three types.

- Integral membrane proteins consist of hydrophobic domains embedded into the lipid matrix and hydrophilic domains in solution. Hence, they cross the bilayer.
- Peripheral membrane proteins are temporarily attached to the membrane and only via indirect interactions. They bind to integral membrane proteins, or to the lipid head groups.

-
- Lipid-anchored proteins are attached to one side of the lipid bilayer by covalently binding to few lipid molecules.

The diversity of proteins in structure and in interactions with the membrane provides a subtle control mechanism for the cell to control the morphology of its membranes. Integral proteins such as nicotinic acetylcholine receptors or voltage dependent potassium channels induce local curvatures because of their conical shapes [47]. Another possible mechanism of membrane sculpting is initiated by peripheral proteins. The dynamin family imposes tubular forms whereas coat protein complexes such as clathrin, COPI and COPII induce spherical curvatures by forming scaffolds around the membrane [48].

For the special case of the mitochondria, the proteins hold a central position in the communication between structure and function. The regular arrangement of the F₁F₀-ATP synthase is probably one of the actors driving the inner membrane to tubulation [29, 40, 49]. There are also proteins known to affect cristae morphology directly such as mitofilin in humans [50] or Fcj1 in yeast [41]. The composition of membrane lipids is also known to modify the membrane geometry, especially the concentration of cardiolipin [39]. The *in situ* structure of the mitochondrial membrane becomes functional as result of the cooperation of these different effects.

3.2.3 Membrane mechanics

A large enough membrane structure, *e.g.*, the membrane of a cell or an organelle, can be considered as a two-dimensional surface embedded in three-dimensional space, since its thickness ($\sim 5\text{nm}$) is negligible with respect to the lateral size (at the order of micrometers). On this level of coarse-graining, the interactions between lipid molecules are translated to a mechanical energy of the surface, expressed as a function of curvatures of the two-dimensional surface. One possible way to write the curvature dependency is to combine second order terms. Hence, we obtain the classical curvature model:

$$E_b = \frac{\kappa_b}{2} \int dA (2H - C_0)^2 + \kappa_G \int dA K, \quad (3.1)$$

3. FLUID MEMBRANE INVAGINATIONS

where H is the mean and K the Gaussian curvature (see appendix A for a definition of the geometrical quantities). The material constants κ_b and κ_G are, respectively, the bending rigidity and Gaussian rigidity, or saddle-splay modulus. The spontaneous curvature C_0 represents an intrinsic preferred mean curvature value of the membrane due to a possible asymmetry of lipid density in the membrane layers. This model proposed independently by Canham [51], Helfrich [52] and Evans [53], proved itself useful to explain phenomena such as membrane tethering or budding [45]. The famous Gauss-Bonnet theorem from differential geometry states that for a given topology of genus g , the integral of Gaussian curvature is a topological invariant of value $4\pi(1 - g)$. Therefore, the second term in 3.1 is constant for a vesicle of spherical topology. Since its variation is zero, the term does not appear in the equilibrium equations and is neglected in the following. This leaves us with only the mean curvature term:

$$E_b = \frac{\kappa_b}{2} \int dA (2H - C_0)^2 . \quad (3.2)$$

In aqueous solution, the concentration of free lipid molecules is very low due to the hydrophobic repulsion of the tail as we mentioned earlier. Therefore, once the system is in equilibrium there is practically no exchange of lipid molecules between the solution and the bilayer. This also means that the surface area is constant and this conservation should be a part of the mechanical description. Another contribution to the mechanics arises from the osmotic pressure. Even though the bilayer is permeable to the water molecules, it is not to a lot of water soluble molecules (*e.g.* sugar). If the osmotic pressure due to concentration gradients was not balanced, this would result in a net flow of water and an eventual breakdown of the lipid membrane. So the volume of the vesicle should be controlled in such a way to prevent the osmotic pressure to build up [45].

The energy scales of the terms associated to area conservation and osmotic pressure outweigh the bending term. In other words, it is much easier to bend the surface of a lipid vesicle than to expand (or shrink) its area or volume. Therefore, these two terms are usually treated as constraints on the area A , and the volume V and incorporated into the mechanical energy via Lagrange multipliers σ and

p :

$$E = \frac{\kappa_b}{2} \int dA (2H - C_0)^2 + \sigma A + pV . \quad (3.3)$$

The variation of the energy with respect to the variation of the surface gives an equilibrium condition, which is also known as the shape equation [54, 55]:

$$p + 2\sigma H - \kappa_b [(2H - C_0)(2H^2 - 2K - C_0H) + 2\Delta H] = 0 . \quad (3.4)$$

Note that the bending part of the equation above is the same as the equation 2.6 provided that the spontaneous curvature C_0 vanishes and we use the identity $b_{\alpha\beta}b^{\alpha\beta} = 4H^2 - 2K$.

For simulation purposes, it is usually more suitable to enforce the constraints with penalties. We will also make use of the following form of the mechanical energy:

$$E = \frac{\kappa_b}{2} \int dA (2H - C_0)^2 + \frac{\mu_A}{2}(A - \bar{A})^2 + \frac{\mu_V}{2}(V - \bar{V})^2 , \quad (3.5)$$

where μ_A and μ_V are penalty factors implementing the constraints.

Note that the energy formulation we use here is very similar to that of elastic sheets of Chapter 2. When C_0 vanishes, the bending energy 3.2 is the same as the energy given in Eq. 2.1. However, an unstretchable sheet is more rigid than its fluid counterpart due to the local metric conservation. For instance, a conical defect on a fluid membrane is unstable: it can always lower its energy by smoothing out the singularity [16].

3.3 Model

From a theoretical point of view, the simplest way to generate surface invaginations is to imagine a growing, closed membrane enclosed in a rigid container of constant area and volume. When the surface area of the membrane exceeds that of the container, it should buckle inwards; this is required by the geometrical constraint. Hence, omitting the action of proteins on the membrane provides a clear formulation of the invagination problem separating internal anisotropies due

3. FLUID MEMBRANE INVAGINATIONS

to proteins from the external effect of the confinement.

Since we are interested in the deformations of large membrane structures, we use the continuous description of the membrane surface as given by the equation 3.2. The deformation of a closed membrane of known volume V and surface area A in a confinement introduces a new length scale into the system, *i.e.*, the size of the cavity. But we are interested in the relative size of the membrane with respect to that of the container. So, we describe the system by the dimensionless scaled volume v and area a , such that

$$v = V/V_c \quad \text{and} \quad a = A/A_c, \quad (3.6)$$

where V_c and A_c are the volume and the area of the container. When a exceeds 1, one naturally expects the membrane to fold inside, a transition that lowers the symmetry of the system. Without doing any calculation, it is intuitively obvious that, for sufficiently high values of a , the infoldings of the membrane should touch itself. To be physically plausible the impenetrability of the membrane has to be included in the model via self-avoidance of the surface of the continuous description. The system, already nonlinear itself, becomes even more complex due to the boundaries in contact with the container. In this study, we resorted to two different numerical methods to overcome this issue.

The first method we rely on is the “shooting method”. In this method, we implement the constraints via Lagrange multipliers as given in the equation 3.3. Under the assumption of axisymmetry of shapes with no self-contact, the variational problem of finding extrema of the system 3.3 can be expressed by a set of first order differential equations. In this reduced form the variational equations of the system can be numerically integrated in a relatively easy manner by a Runge Kutta method (see appendix C for more details).

For more complex geometries involving asymmetries and self-contacts, a full three-dimensional treatment of the problem using the finite elements (FE) technique is more suitable. Rather than blindly using classical FE approaches used in material sciences [56], one should be careful about the peculiarities of fluid membranes. The mechanical energy we adopt involves squares of curvatures which are second derivatives of the surface vector function. This means in the language

of FE that trial functions should have square-integrable derivatives up to second order. In order to satisfy this requirement, we describe the membrane surface according to the subdivision FE technique adapted to the study of fluid membranes [57, 58]. We model the effect of the outer membrane by adding a rigid¹ container to the system. In terms of FE simulations this means that we apply a repulsive force field penalizing the membrane if it tries to go beyond the boundary of the cavity field. Such kind of soft constraint allows the membrane to intrude into the force field, but of course at the expense of increasing its energy. Consequently, the radius of the shell can slightly exceed that of the container. Similarly, the self-avoidance of the membrane is enforced by a quadratic repulsive potential between intersecting polygons of the discretized surface (see appendix D for further details on the simulations).

3.4 Results

3.4.1 Spherical confinement

As a first step, we consider a system with a spherical container. We simulated the fluid inner membrane inside this container for a large range of scaled surface area a and scaled volume v . Imposing $a > 1$, it is intuitively clear that the membrane will not fit into the container in a trivial way. It has to break its symmetry by folding into the interior². In the following, we will present the results of the simulations of this system in two parts, each corresponding to different invagination regimes.

3.4.1.1 Moderate surface growth

Already a small increase in the surface area will cause the inner membrane to detach slightly from the container. For sufficiently large values of surface growth, this detachment has a peculiar form: it consists of a large spherical domain connected via a narrow neck to the part in contact with the outer shell (see fig. 3.3a). The contribution of the invagination to the bending energy is about $e_s = 8\pi\kappa$, the value of the bending energy of a sphere. A secondary invagination

¹Rigid, in the sense that it does not change its spherical geometry

²Note that the volume enclosed by the membrane has to be smaller than 1 as well.

3. FLUID MEMBRANE INVAGINATIONS

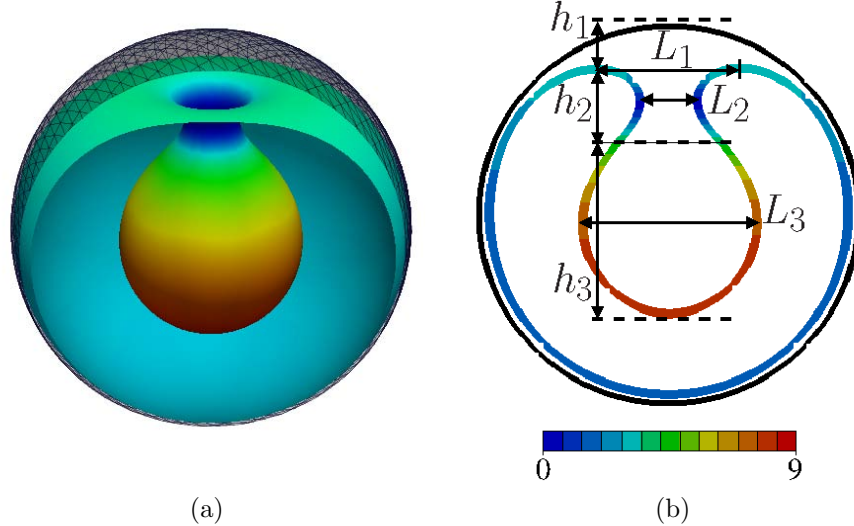


Figure 3.3: (a) Numerical equilibrium solution for a membrane (smooth surface) inside a spherical container (black mesh) with scaled area $a = 1.2$ and scaled volume $v = 0.8$. The membrane bulges inward and forms an invagination reminiscent of a light bulb. (b) Vertical slice of the inner membrane, which contains the axis of symmetry, together with the corresponding bending energy density. In (b) the measured distances of the invagination are defined (see Tab. 3.1).

of the same form would contribute another e_s to overall energy, which is why the equilibrium state does not have multiple invaginations.

For moderate surface growth, the inner membrane appears to maintain the axisymmetry of the initial sphere. We confirmed this impression by analyzing the curvature profile of the horizontal slices:

1. We calculated the symmetry axis of the shape by taking the mean of the surface normals at each vertex.
2. We took a slice of the membrane perpendicular to the axis of symmetry at the point where the invagination is the thickest.
3. Using a discrete formulation of the curvature based on a second-order polynomial approximation of the curve on sample points [59], we estimated the curvature for each invagination slice.

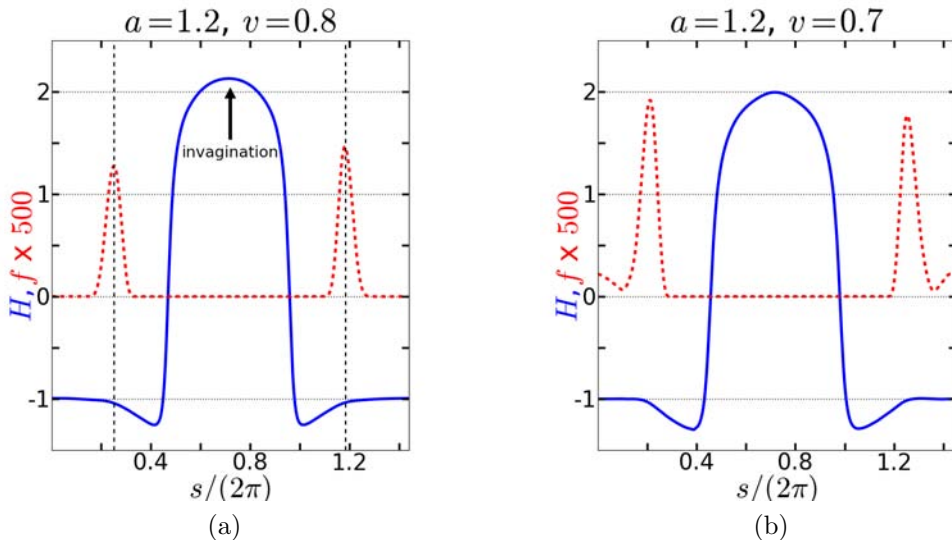


Figure 3.4: Mean curvature H of the inner membrane (blue solid line) and container force $f = |\mathbf{f}_a^{C1}|$ (red dotted line) as a function of the scaled arc length $s/(2\pi)$ for $a = 1.2$ and (a) $v = 0.8$ and (b) $v = 0.7$. All curves were obtained with the finite element method.

We concluded that the inner membrane shapes under moderate surface growth are axisymmetric within the numerical errors.

Once the axisymmetry of the shapes is established it is possible to reduce the fourth order differential shape equation 3.4 to a set of first order ordinary differential equations which can be solved numerically using the shooting method (see appendix C for details). This method confirms that the obtained shapes are truly axisymmetric. For $(a, v) = (1.2, 0.8)$, for instance, the profile found with the shooting method (see Fig. C.1) coincides with the shape of the finite element method in Fig. 3.3a within the numerical errors. Therefore, a two-dimensional vertical slice of the shape which contains the axis of symmetry embodies all the necessary information of a given solution. For $(a, v) = (1.2, 0.8)$, such a two-dimensional slice is shown in Fig. 3.3b together with the bending energy density¹.

In Fig. 3.4a, we provided the mean curvature of the inner membrane along a

¹Although the membrane shape resembles a stomatocyte as it is found in the corresponding reduced volume problem without the container, we note that it is the confinement which forces the membrane into this form; a free vesicle would adopt the form of an ellipsoid for these parameter values [45].

3. FLUID MEMBRANE INVAGINATIONS

two-dimensional slice (see blue solid line) and also the corresponding container forces (see red dotted line). At the section where the membrane is in contact with the container, the mean curvature of the membrane is constant as expected; it equals the mean curvature of the unit sphere, *i.e.*, $H = -1$. To invaginate, the membrane has to detach from the container decreasing its mean curvature $H < -1$ ¹. At the neck, the surface normal changes its orientation, $H > 0$. It becomes greater than one towards the tip of the invagination. For the idealized problem at the point where the inner membrane loses contact with the container, delta forces are needed to equilibrate the system. In the finite element simulations, we observe smooth spikes instead of the ideal delta forces, since the membrane can slightly penetrate into the container, which is implemented by a quadratic potential and not with an infinite potential well.

For the same scaled area value $a = 1.2$ but slightly smaller volume $v = 0.7$, the inner membrane is still axisymmetric. The mean curvature of a two-dimensional slice has the same behavior (blue solid line in Fig. 3.4b). However, the force curve (red dotted line in Fig. 3.4b) has three peaks instead of two. The third peak is a sign that the bottom part of the membrane also penetrates the container. Not surprisingly, the numerical shooting method does not provide any solution for these values of (a, v) , because the underlying model does not allow the membrane to penetrate into the container (see Fig. 3.5 and also appendix C). However, the container forces at $(a, v) = (1.2, 0.7)$ are very small compared to the other forces in the system, especially with respect to the dominant bending term. The mean curvature stays still almost equal to $H = -1$, at the bottom. But for lower values of v , the invagination touches the opposite part of the membrane at the bottom and pushes it. As a result, the two self-touching layers of the membrane go slightly beyond the limits of the container.

In Fig. 3.3b, we defined length parameters to quantify the simulation results. The variable L_1 denotes the horizontal distance between the uppermost points; L_2 and L_3 are taken at the narrowest and the broadest point of the invagination, respectively. The vertical distance h_1 indicates how much the inner membrane

¹Indeed, at this point it has a more pronounced “curvature”, because the absolute value of the mean curvature is bigger than that of a unit sphere $|H| > 1$, the minus sign indicates the orientation of the normal.

(a, v)	L_1	L_2	L_3	h_1	h_2	h_3	e_b
(1.1,0.9)	0.94	0.48	0.65	0.23	0.47	0.54	1.80
(1.2,0.9)	0.65	0.27	0.88	0.09	0.28	0.91	1.86
(1.3,0.9)	0.57	0.23	1.04	0.06	0.28	0.99	1.88
(1.1,0.8)	1.00	0.48	0.76	0.35	0.46	0.70	1.83
(1.2,0.8)	0.76	0.31	0.95	0.20	0.34	0.10	1.87
(1.3,0.8)	0.62	0.24	1.11	0.09	0.31	1.08	1.88

Table 3.1: Measurements of characteristic system parameters (see Fig. 3.3b). The error of measurement is about ± 0.05 for all length and ± 0.1 for the scaled bending energy $e_b := E_b/(8\pi\kappa)$. All values were obtained with the finite elements method.

detaches from the container, h_2 measures the length of the neck, and h_3 the extension of the tip of the invagination. In Table 3.1 we report the corresponding numerical values for moderate surface growth and $v = 0.8$ and 0.9 . We remark that for constant volume v the height h_3 of the large domain of the invagination increases with increasing surface area a , whereas the neck shrinks both in length h_2 and diameter L_2 . Decreasing the volume enclosed by the inner membrane, leaves the overall geometry intact but a quick glance to the geometric phase diagram (see fig. 3.5) reveals that the invagination penetrates deeper.

In the last column of Tab. 3.1, we provided our measurements of the bending energy e_b of the whole inner membrane normalized by the bending energy of a sphere. We find that it is very close two. As we mentioned earlier, each invagination's contribution to the bending energy is about e_s . The domain which is in contact with the container contributes also at the order of e_s , making the total bending energy close to that of two spheres. This makes it plausible to think of the system as the conjunction of two isolated spheres. We thus imagine that we cut the neck as it is pictured in Fig. 3.6a. In this case, we are left with two distinct vesicles: the invagination constitutes the inner vesicle enclosed into the outer one (the part of the membrane in contact with the container). We consider such a system as a simple model for the inner membrane. In this simplified setup, the radius of the outer vesicle is equal to that of the container, $R_o = 1$. The radius of the inner sphere is set to R_i . Then, the scaled area a of the system can be written as the sum of the scaled areas of both spheres $a = 1 + R_i^2$. Similarly, the

3. FLUID MEMBRANE INVAGINATIONS

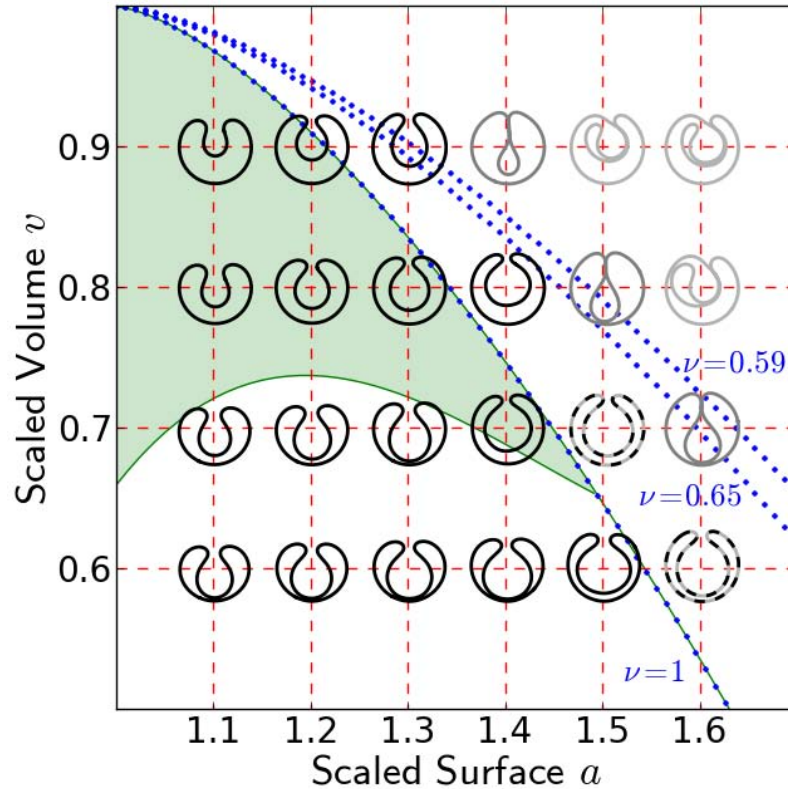


Figure 3.5: Geometric phase diagram with vertical slices of each simulation point. The color of each slice corresponds to the different regimes observed: the invagination is either axisymmetric (black), ellipsoid-like (dark gray), or stomatocyte-like (light gray). The slices of the non axisymmetric shapes lie in the symmetry plane perpendicular to the slit-like neck. For the dotted slices a metastable ellipsoid-like state has been observed. Eqn. 3.8 is plotted for different values of ν (dotted lines). The green shaded zone represents the values of (a, v) for which solutions could be found with the numerical shooting method. The underlying model in numerical shooting does not allow the membrane to penetrate into the container (see appendix C).

ratio v of the volume between the two spheres to the volume of the container is given by the difference $v = 1 - R_i^3$. Eliminating the R_i dependence we can easily relate the two scaled parameters by the following simple relation:

$$v = 1 - (a - 1)^{3/2}. \quad (3.7)$$

The system of two isolated spherical vesicles exists only if this equation is fulfilled. At the limit case where $a = 1$ and $v = 1$, the inner radius vanishes and we are just left with one unit sphere. The opposite limit corresponds to $a = 2$ and $v = 0$ where the inner sphere reaches the size of the outer one and the system consists of two unit spheres. The case $v < 1 - (a - 1)^{3/2}$ corresponds to the region below the blue dotted line marked with $\nu = 1$ in the geometric phase diagram (see Fig. 3.5). Under this condition, the 2-sphere system should be under stress since the volume between the two spheres wants to be smaller than the membrane can accommodate with the available area. But, the system in the simulations does not feel such a stress, since it can still decrease its volume below the requirement 3.7 by detaching the outer part from the container. This explains why the invaginations are axisymmetric for moderate surface growth: The energetically favorable state requires a sphere-like inner domain and the constraints on volume and area are satisfied by a detachment from the container (see Fig. 3.6b).

A possible improvement of the 2-sphere model could consist of adding a tube to connect the two spheres, approximated by a shape whose geometric properties are fully known. Indeed a visual inspection of the neck of axisymmetric invaginations suggests the catenoid as a good candidate. However, such a model turns out to be insufficient to explain the results of simulations *quantitatively*. This is not so surprising if we look at the mean curvature plots again (see Fig. 3.4a and Fig. 3.4b). Along a slice, the mean curvature H at the neck changes abruptly from negative (part in contact with the container) to positive (invagination) in contrast to a catenoid whose mean curvature is exactly zero everywhere.

The opposite condition, *i.e.*, $v > 1 - (a - 1)^{3/2}$ indicates an excess of surface area. The resolution of this frustration will be the breaking of the symmetry as one can see by flashforwarding to Fig. 3.7a. But the existence of the neck

3. FLUID MEMBRANE INVAGINATIONS

alleviates this effect: the tip of the invagination can still keep a shape close to a sphere if a is not too large (see Fig. 3.5). The transition occurs at higher values of a than the 2-sphere model predicts.

3.4.1.2 High surface growth and symmetry breaking

For a realistic simulation of the biological membrane, one should ensure the self-avoidance of the computational surface. Even though this requirement does not hinder the simulation of axisymmetric shapes, it becomes an issue if we are willing to pack more and more membrane into the container. To accomplish this, we implemented a collision resolution algorithm. Essentially, it detects the self-contacts of the mesh and penalizes them by gradients derived from the minimization of the intersection contour (see appendix D.2 for more details).

Equipped with this algorithm, we investigated a larger range of (a, v) values where the membrane loses its axisymmetry. An example of such a shape can be seen in Fig. 3.7a. The invagination is not spherical anymore, it rather forms an ellipsoid reminding us of the shapes found in reduced volume problems such as in [45]. The invagination is connected to the outer part of the inner membrane via a neck, which is now expanded to a slit. The slit, composed of two opposite membrane patches apposed to each other, appears to separate two tube-like openings. We observe this peculiar form as a metastable state in the simulations of points $(a, v) = (1.5, 0.7)$ and $(1.6, 0.6)$. It endures for long simulation times, indicating that this configuration is a local minimum although the global minimum of the system is axisymmetric¹. If we constrain the system more, by increasing the surface area or the volume inside, this metastable state turns out to be the equilibrium shape (see $(a, v) = (1.4, 0.9)$, $(1.5, 0.8)$, and $(1.6, 0.7)$ on the phase diagram in Fig. 3.5). Another shape transition occurs if we constrain the system a bit more. For instance, for $(a, v) = (1.5, 0.9)$, we observe that a second invagination bulges into the first one (see fig. 3.7b – 3.7d), forming a stomatocyte-like invagination. The shape of the secondary invagination resembles an axisymmetric one.

¹This is true for the FE simulations where the inner membrane can penetrate into the force field of the container. The numerical shooting method did not yield any axisymmetric solution for these values of (a, v) .

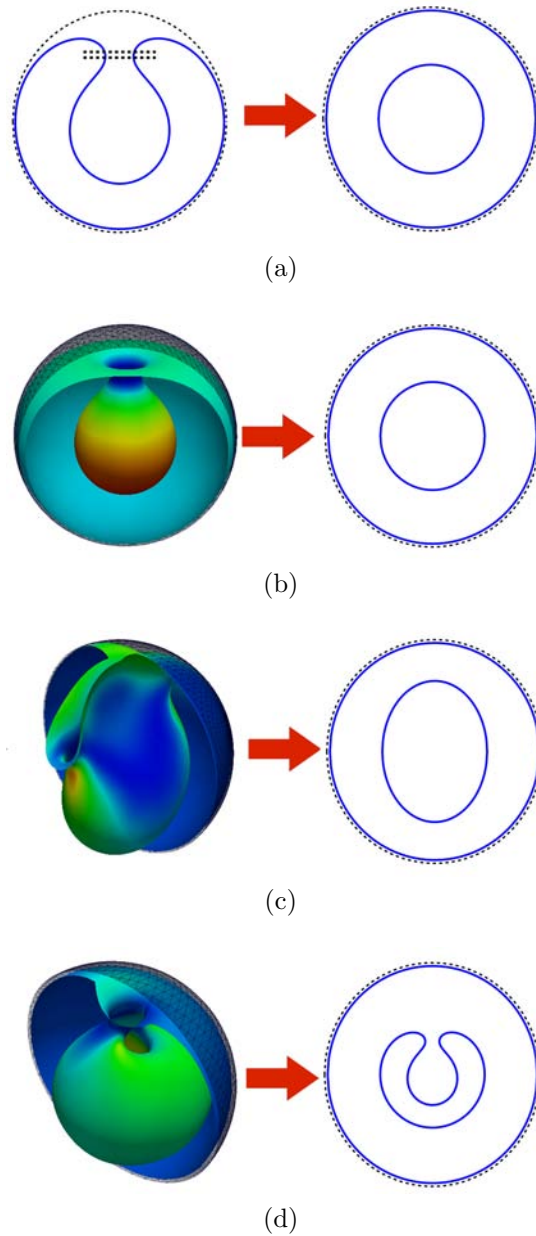


Figure 3.6: In the simple model the neck of the inner membrane is omitted. As depicted in (a), this operation leaves us with a spherical boundary membrane and a vesicle which corresponds to the invagination. (b) For moderate surface growth the inner vesicle has a spherical shape as equilibrium solution which corresponds to axisymmetric invaginations. Higher surface area forces the vesicle to break the axisymmetry, by adopting an ellipsoidal shape (c) first, then a stomatocyte (d).

3. FLUID MEMBRANE INVAGINATIONS

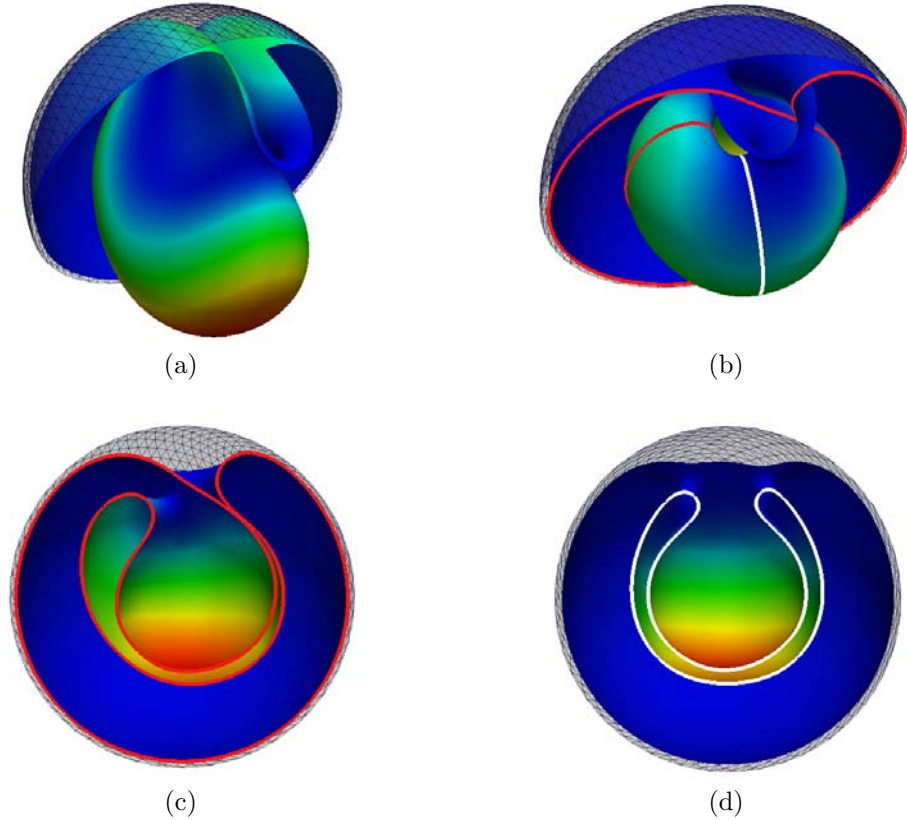


Figure 3.7: Numerical equilibrium solutions which break axisymmetry. (a) Ellipsoid-like state for $(a, v) = (1.6, 0.7)$. (b) Stomatocyte-like state for $(a, v) = (1.6, 0.9)$. (c) Cut of the stomatocyte-like state along the symmetry plane. (d) Cut of the stomatocyte-like invagination perpendicular to the symmetry plane.

To understand these shape transitions, we apply the simple model neglecting the neck again. We keep the outer sphere of radius one (*i.e.*, the part of the membrane in contact with the container) in the system but now we have a vesicle (the invagination) of arbitrary shape inside. We use the definition of the reduced volume $\nu_i = \frac{6\sqrt{\pi}V_i}{A_i^{3/2}}$, where V_i and A_i are the volume and the area of the inner vesicle, respectively. We can write the scaled area as a function of outer and inner vesicle, *i.e.*, $a = \frac{A_o + A_i}{A_o}$. Similarly, the scaled volume is $v = \frac{V_o - V_i}{V_o}$. Combining all these definitions, the relation between a and v now reads:

$$v = 1 - \nu(a - 1)^{3/2}. \quad (3.8)$$

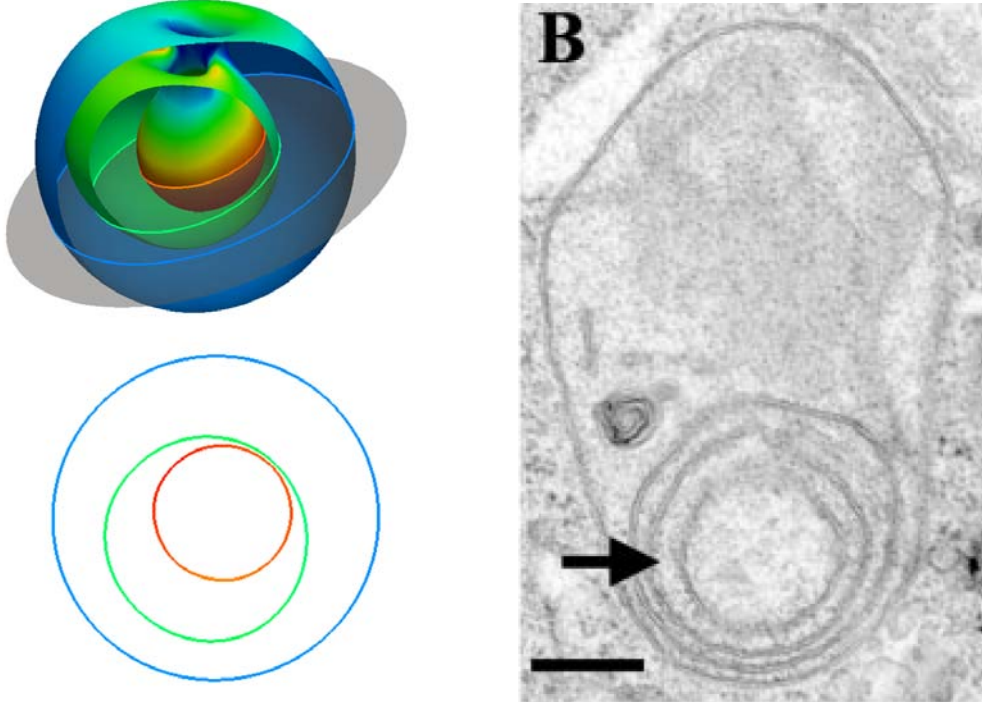


Figure 3.8: Slices of a finite element solution with high area (left: $(a, \nu) = (1.6, 0.8)$ as in Fig. 3.7b resemble electron microscopic images of mitochondria with high and uncontrolled surface growth (right: Figure 6B reproduced from Ref. [50]; scale bar corresponds to 250 nm).

Since we know the equilibrium shape of a vesicle of fixed reduced volume from [45], we can tell which shape the inner vesicle will adopt. For $0.65 \leq \nu \leq 1$ the global energy minimum corresponds to a spherical volume enclosing a prolate ellipsoid in the middle (see Fig. 3.6c). Decreasing the value of ν more and more, causes the ellipsoid to become oblate for $0.59 \leq \nu \leq 0.65$, while for $\nu \leq 0.59$ the invagination distorts into a stomatocyte shape (see Fig. 3.6d). The transition lines corresponding to different values of ν are depicted in the phase diagram (Fig. 3.5) by blue dotted lines. We observe that the corresponding shape transitions can indeed be found in the phase diagram but with a small shift. This is due to the existence of the neck that connects the inner and outer membrane domains.

The transition from an ellipsoidal invagination to a stomatocyte-like invagination suggests a mechanism to accommodate the surface growth in the system. In case of further increase of the surface area, we would expect a third invagination

3. FLUID MEMBRANE INVAGINATIONS

forming in the interior, then a fourth, a fifth and so forth. A similar structure is observed in experiments of John *et al.* in which the inner membrane protein mitofilin is suppressed [50]. The mitofilin controls the architecture of the inner mitochondrial membrane and it is essential for the formation of normal tubular cristae as well as cristae junctions. In the absence of mitofilin, the inner membrane forms stacks of onion-like structures, which resemble cuts of our numerical shapes rather closely (see Fig. 3.8). Similar shapes are also observed in the experiments of Paumard *et al.*, where the subunits e and g of mitochondrial protein F_1F_0 -ATP synthase are suppressed [60]. Obviously, the topology of the complex membrane structure in the experiments is different from the spherical topology of our simulation results, however, the basic structure is the same. *In vivo*, the topology is a dynamical property of the membranes which is known to be remodeled by self-contacts and curvature sensing proteins. Although our simulation model does not include any topological changes, in the light of biological data, we can speculate that the membrane domains in contact with each other at the neck would possibly fuse if allowed, changing the topology. In a similar manner, we can imagine a fusion scenario for the ellipsoidal invagination in Fig. 3.7a: a fusion taking place at the slit-like neck would form two tubular necks that connect the invagination with the rest of the membrane.

3.4.2 Confined vesicles with spontaneous curvature

Fusion and fission processes can also be initiated by the mediation of proteins. The self-contact of the membrane is not a crucial requirement. The classical example is vesicle formation and budding, especially in clathrin-mediated endocytosis. The budding is initiated by BAR domain proteins, stabilized by the polyhedral scaffold of the clathrin coating proteins [61], and scised by the recruitment of dynamin to the neck [62]. A similar but opposite budding/scission mechanism can be found in the endolysosomal pathway. In this pathway, the ESCRT machinery induces and cleaves the endosomal buds from the inside of the neck [63]. The work of proteins is indispensable for the correct folding of mitochondrial cristae as well [41, 50].

Regardless of the specific details of each mechanism, all these processes can

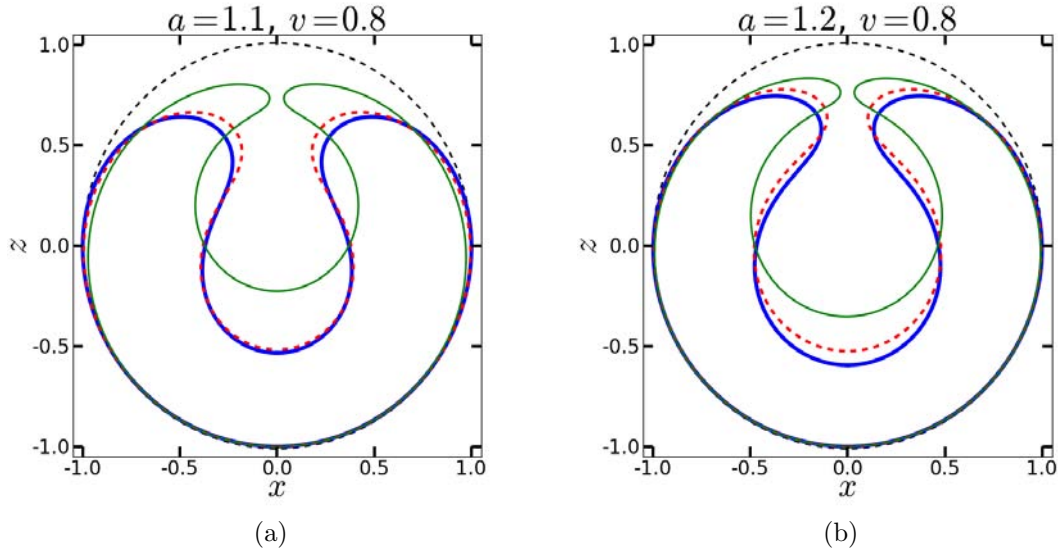


Figure 3.9: Slices of numerical equilibrium solutions of a membrane inside a spherical container with $v = 0.8$ and (a) $a = 1.1$ and (b) $a = 1.2$. The spontaneous curvature varies from $C_0 = 0$ (blue thick solid line) to $C_0 = 0.1$ (red dashed line) and $C_0 = 1$ (green thin line). All slices were obtained with the finite element method and compared to the shooting method (see text).

be understood in terms of a local curvature regulation of the membrane. From a theoretical point of view, such an induced curvature corresponds to a change in the preferred ground state of the membrane; hence it can be accommodated via the spontaneous curvature term C_0 of the energy 3.2. This is in contrast to our previous simulations where a free membrane, having $C_0 = 0$, would adopt a flat shape. By choosing a non vanishing value for the spontaneous curvature C_0 , constant along the whole surface, we set the mean curvature the membrane wants to adopt. Thus, we can study the effect of curvature regulation in a global manner. However, due to the other factors in the system, like the constraints on surface area, enclosed volume, and confinement, the exact shape cannot be predicted ad hoc.

In Fig. 3.9 we plot the slices of the equilibrium surfaces at fixed scaled area and volume for different values of spontaneous curvature, namely $C_0 = 0, 0.1$, and 1. Both for $a = 1.1$ and $a = 1.2$, the system conserves its axisymmetry while the spontaneous curvature increases. However, the shape is modified: the

3. FLUID MEMBRANE INVAGINATIONS

neck shrinks in size gradually, the invagination moves up and adopts a more spherical form. Even though the preferred curvature is positive, the part where the membrane is in contact with the container has to maintain the contact, so it is firmly constrained to a constant negative mean curvature, $H = -1$.

The validity of the FE simulation results can be checked with the shooting method as well, since the shapes are axisymmetric. For low values of the spontaneous curvature, such as $C_0 = 0.1$, the results issued from two different computations coincide within the numerical errors. For the higher values of spontaneous curvature such as $C_0 = 1$, the shooting method does not give a solution. The reason for this is similar to the example given in Fig. 3.4b in Sec. 3.4.1.1. The Finite Element surface leaves the container at the bottom, in stark contrast to our implementation of the shooting method where there is no room for the surface to exceed the container. For even higher values of C_0 , no equilibrium shape can be found at all, the mesh destabilizes around the neck. This suggests that for strong curvatures, the neck prefers to be pinched-off to free the invagination as an independent vesicle, in agreement with what can happen *in vivo*.

As a result, even a *global* modification of the curvature ground state works as an effective way of controlling the length scales of an invagination, a fact which has been already observed before for unconfined membranes [64, 65, 66, 67].

3.4.3 Influence of the container geometry

Until this point we have considered membranes confined in a spherical container. However, membrane invaginations *in vivo* such as the cristae of mitochondria usually occur in a non-spherical confinement. The shape of mitochondrial outer membranes show a large diversity. They are observed in the form of small spheres as well as large tubular networks [68]. Therefore, the effects of the deformation of the container shape merits attention.

In section 3.4.1.1, we have seen that in a spherical confinement, the invaginations of a fluid membrane of zero spontaneous curvature, can be understood by simple arguments of reduced volume (see Eq. 3.8). For a general confinement, we can exploit this bit of knowledge before rushing into any numerical computation. We incorporate the arbitrariness of the container into the approximative

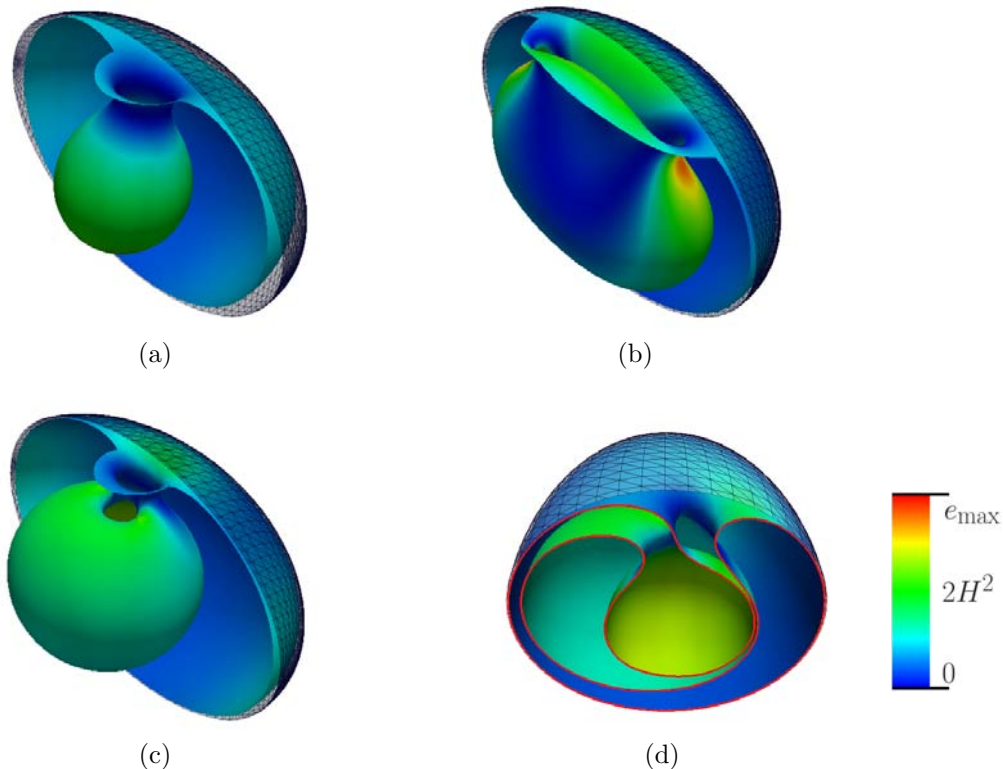


Figure 3.10: (a) Numerical equilibrium solution for a membrane (smooth surface) inside an ellipsoidal container (black mesh) with axes $\xi = 1.5$, $\chi = \zeta = 1$, scaled volume $v = 0.8$ and scaled area (a) $a = 1.2$, (b) $a = 1.5$, (c) $a = 1.6$, (d) $a = 1.6$, cut through xy -plane. Colors represent the bending energy density of the membrane ($\equiv 2H^2$). Maximum values of the scale bar are (a) $e_{\max} = 12$, (b) $e_{\max} = 20$, (c) $e_{\max} = 12$ and (d) $e_{\max} = 12$, respectively.

model, by introducing the area A_c and the volume V_c of the container as variables. Again, we omit the neck and assume that the invagination is a free vesicle held inside the outer part of the inner membrane in contact with the container. We can then express the scaled surface a of the inner membrane as the sum of the areas of the invagination, A_i , and the boundary membrane, A_o , divided by the container area¹. If we assume that the boundary part is a closed vesicle that coincides with the container, both have the same area, *i.e.*, $A_o = A_c$, we obtain

¹One can as well normalize a and v with respect to the unit sphere instead of the container. This results in a slightly modified equation 3.9 but does of course not change the predictions of the model.

3. FLUID MEMBRANE INVAGINATIONS

$a = \frac{A_o + A_i}{A_o}$. Similarly, the scaled volume is given by $v = \frac{V_o - V_i}{V_o}$. Hence, v and a are now related by the equation

$$v = 1 - \frac{\nu_i}{\nu_o}(a - 1)^{3/2}, \quad (3.9)$$

where the parameters ν_i and ν_o denote the reduced volume of the invagination and of the boundary membrane (*i.e.*, the container), respectively. Note that for a spherical container $\nu_o = 1$, and this relation reduces to Eq. 3.8. Hence, according to Eq. 3.9, in the case of an arbitrary confinement, the transition lines should shift with respect to the spherical case as a function of the reduced volume.

In principle, one can apply any kind of deformation to the container in the simulations, as long as the potential corresponding to the geometry is well defined. We choose a prolate ellipsoid as the container shape because firstly, it is a comparatively simple deformation of the sphere with a tunable reduced volume and secondly, it is a good approximation for tubular organelles. For a prolate container, the equation of the surface is now given by:

$$\frac{x^2}{\xi^2} + \frac{y^2}{\chi^2} + \frac{z^2}{\zeta^2} = 1, \quad (3.10)$$

where we will tune the reduced volume by the axis parameter $\xi \geq 1$, while setting the two others equal to one. Increasing the value of ξ increases the ellipticity of the container according to $\varepsilon = \sqrt{1 - \xi^{-2}}$. Using the definition of the ellipticity, the area and volume of such a prolate spheroid are expressed by [69]

$$A_o = 2\pi \left(1 + \frac{\xi}{\varepsilon} \arcsin \varepsilon \right) \quad \text{and} \quad V_o = \frac{4\pi}{3} \xi, \quad (3.11)$$

respectively. The reduced volume follows as

$$\nu_o = \frac{2^{\frac{3}{2}} \xi}{\left(1 + \frac{\xi}{\varepsilon} \arcsin \varepsilon \right)^{\frac{3}{2}}}. \quad (3.12)$$

Increasing the ellipticity of a prolate ellipsoid by increasing the parameter ξ , decreases the reduced volume only slowly. For instance, at an eccentricity corresponding to $\xi = 1.5$, the reduced volume is $\nu_o = 0.96$, which is still close to

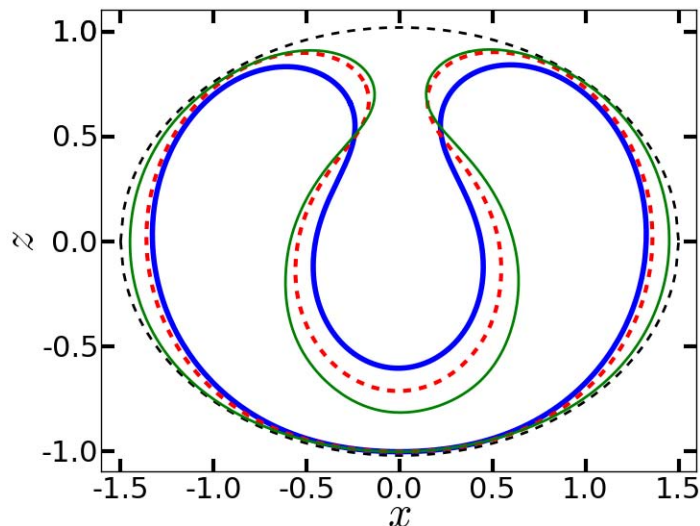


Figure 3.11: Slice of the system along the major axis for fixed $\xi = 1.5$ and $v = 0.8$ and different scaled areas $a = 1.1$ (blue thick solid line), $a = 1.2$ (red dashed line) and $a = 1.3$ (green thin line). For these areas the membrane detaches from the container.

one. This means that the shape of the invaginations should essentially stay the same compared to the case of the spherical confinement. And this is indeed what happens: In Fig. 3.10 we show the results of the finite element simulations of a membrane inside a prolate container with $\xi = 1.5$. The scaled volume is fixed to $v = 0.8$ and a is set to 1.2, 1.5, and 1.6, respectively. The shapes that we observe are consistent with the argument above. They are almost the same as those inside a spherical container (see Fig. 3.6) for the same set of (a, v) values.

We note that the invaginations pop up on almost planar regions of the ellipsoid. This is observed for other values of the parameters as well, not only for the membranes presented in Fig. 3.10. Another interesting aspect is the orientation of the slit-like neck of non-axisymmetric invaginations. They apparently tend to align themselves along the major axis of the container. This is predictable if one imagines the reverse configuration, packing one ellipsoid into another of comparable size with their major axes at a right angle. Obviously, such a conformation violates the self-avoidance of the membrane considerably, hence it is penalized by

3. FLUID MEMBRANE INVAGINATIONS

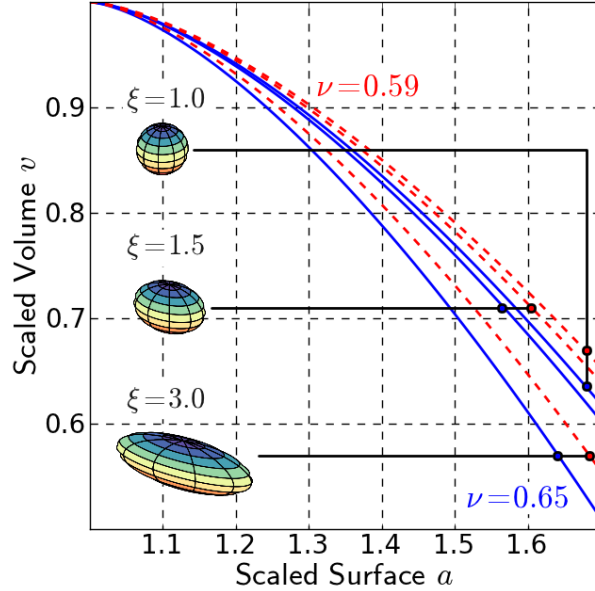


Figure 3.12: Shift of the transition lines *axisymmetric* \rightarrow *ellipsoidal* (Eq. 3.9) with $\nu_1 = 0.65$; blue solid lines) and *ellipsoidal* \rightarrow *stomatocyte-like* (Eq. 3.9) with $\nu_1 = 0.59$; red dashed lines) in the (a, v) phase diagram for $\xi = 1, 1.5$, and 3 .

the contact forces.

For low values of a we observe that the membrane detaches from the container at the extremities of the major axis (see Fig. 3.11). The reason for this is relatively simple: The membrane has to form an invagination to fit into the container while accommodating the volume constraint $v = 0.8$ at the same time. This already eats up a non-negligible amount of the membrane area. The remaining part is not sufficient to fill out the container, at least for small values of a such as $a = 1.1$, 1.2 and 1.3 if $\xi = 1.5$.

A further increase of the major axis parameter ξ should cause a significant shift of the transition lines (see above and Fig. 3.12) according to the equation 3.9. Let us follow this line of argument with a quantitative example. The transition from the axisymmetric invagination to the ellipsoidal one occurs around $\nu_1 = 0.65$. Fixing the scaled volume to $v = 0.8$, the corresponding scaled area for the spherical confinement is given by $a = 1.46$. When $\xi = 1.5$, the transition lines should move to $a = 1.44$, which is hard to observe in the simulations as stated.

But even for $\xi = 3$, for which the outer membrane is now cigar-like, the area shifts only to $a = 1.39$. In other words, if the scaled enclosed volume v is large the model predicts a small change of the transition point. In order to observe a significant shift in the phase diagram that we produced for the spherical container, one has to assign very high ellipticities to the container. However, for high ellipticities the contact of the invagination to the bottom part of the membrane prevails. These contacts bringing a new level of complexity to the problem, make the reduced volume arguments and our simple approximative model insufficient.

3.5 Conclusion

In this chapter, we studied the morphogenesis of fluid membrane invaginations using a simple mechanical model. In our approach to the problem we simplified the external constraints as a closed rigid confinement. For moderate values of surface expansion in a spherical container, we observed axisymmetric invaginations as equilibrium solutions. With higher increase in the surface area, the symmetry of the invaginations is broken and we found ellipsoidal invaginations. When we increased the surface area further, the geometry of the invaginations changed drastically. This type of invagination, that we call stomatocyte-like, consists of a secondary invagination inside the first one. We classified the shapes we found into a morphological phase diagram with the help of a theoretical approximative model.

The axisymmetric invaginations obtained for moderate surface growth are able to reproduce the basic geometry of biological invaginations such as inner mitochondrial cristae or embryonal gastrula. Interestingly, a random cut through a stomatocyte-like invagination exhibits similarities to electron tomography images of mitochondria lacking the membrane protein mitofilin. However, we should keep in mind that our model is static in the sense that it does not take into account, for instance, the dynamic nature of mitochondria. They divide and fuse ceaselessly in the cell as we mentioned in the beginning of this chapter.

We also investigated the invaginations of membranes having a non-zero spontaneous curvature, in order to relate our work further to experimental observations. We showed that the spontaneous curvature controls effectively the length

3. FLUID MEMBRANE INVAGINATIONS

scales: already a small change in its value modulates the sizes of the invagination and its connecting neck. Moreover, we studied the effects of non spherical containers. In particular, using ellipsoidal deformations of the simulation container we showed that the invagination morphologies are stable with respect to small geometric perturbations.

Our minimal invagination model, despite its simplicity, is capable of producing a basic set of invaginations which appear to be the ground states of fluid membrane folding under external confinement. Our results could help to differentiate the intrinsic structures of a folded membrane from those which are specific extrinsic effects. As examples of such external modulations, one can think of membrane protein interactions in the case of mitochondria [40, 41] or localized cell differentiation in gastrulation [70]. Both effects can be studied by introducing a local control of the spontaneous curvature into our model. This can be achieved by implementing a Ginzburg–Landau-type interface between different domains of the membrane [58, 71].

Another effect that could be relevant *in vivo* for the regulation of invaginations are the hydrodynamical interactions of the membrane. This is especially valid for the fluid membrane of organelles, surrounded by a viscous environment. Handling of hydrodynamic effects would require the simulation of viscous fluids which can be achieved either by a mixed finite element formulation [72, 73] or by coupling the system to a lattice Boltzmann framework [74].

Our model does not consider topology changes that could be induced via membrane fission or fusion during the folding process. But, it is possible to extend our approach to study such transitions by considering surfaces with higher genus. One can also think of adding an attractive part to the membrane self-contact forces as a way to simulate the stabilizing effect of the proteins involved in cristae formation.

Chapter 4

Polymorphic tubes

In the realm of biological objects, filaments, rods and tubes form another set of low dimensional entities, next to the class of membranes. As in the case of membranes, they can be observed at any scale, trunks of trees being one of the largest instances. This mundane structure that most of us see every day in our way to someplace provides indeed an interesting scaling behavior, if considered altogether with its network of branches. As Leonardo da Vinci observed, the total of the cross-sectional areas of the branches of a tree at every stage of its height equals the thickness of the trunk. It is only recently that Eloy proposed an explanation for *Leonardo's Rule* in terms of the tree's need to resist dynamic mechanical stresses induced by wind [75].

Another example of a one dimensional structure that puzzled careful observers is the coiling of plant tendrils. Climbing plants, seeking a structural support, grow soft and flexible tendrils. In this early period, the tip of the tendril traces large loops, then it binds to a support if it encounters one; otherwise the tendril dries and drops [76, 77]. The tendrils which are in contact with an object become woody and begin to curl. In this phase, forming natural springs, tendrils help plants to resist to winds and other loads. Since the total twist is zero in the tendril before coiling, it should stay the same after coiling. This results in a peculiar shape, a right-handed helix connected to a left-handed one by an inversion patch known as a **perversion** (see Fig. 4.1). A similar phenomenon can be observed in telephone cords or in electrospun nano and microfibers [78].

McMillen and Goriely [77] trace the first account of plant tendrils back to an

4. POLYMORPHIC TUBES

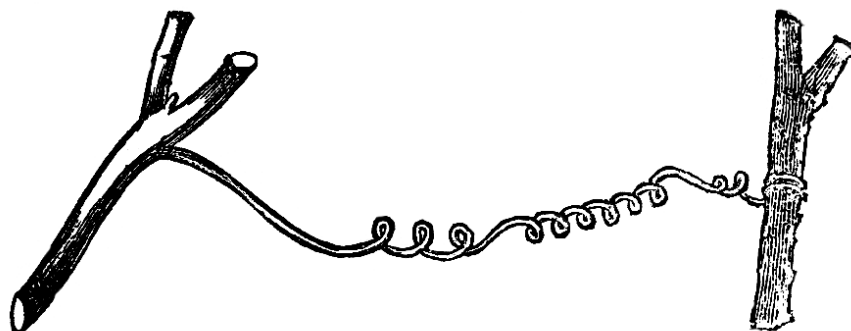


Figure 4.1: Tendril perversion drawn by Darwin (from [77]).

illustration in *Philosophia Botanica* of Linnaei published in 1751. In the nineteenth century, it is a subject addressed in most of the botany books but according to McMillen and Goriely, it is Charles Darwin who provided the first qualitative explanation of tendril perversion in his book *The Movement and Habits of Climbing Plants* in terms of geometric requirement. The mechanical approach to the problem consists of solving Kirchhoff equations for thin elastic rods [77, 79]. In this formulation, the stretching and bending of the rod are expressed as the deformation of the centerline whereas the twist of the rod is addressed through the rotation of a material frame defined on each point of the centerline.

In recent studies [80, 81] on vine tendrils, Vaughn and his colleagues observed the formation of a layer of gelatinous fiber cells when these are coiled. Their findings suggest that these gelatinous fibers can be the driving cause for coiling and twining in vines. Mahadevan and his coworkers observed similar results for cucumber tendrils [82] and asserted that coiling is driven by the asymmetric contraction of fibers. Experiments done on model systems and numerical simulations corroborate this idea of intrinsic curvature generation via the broken radial symmetry.

In this chapter, we will propose and study a polymorphic tube model to understand the symmetry breaking of a rod in terms of the incompatibility of its constituents. But before diving into the details of the model it is important to see that elasticity matters to thin and long macromolecular objects as well. A biofilament such as DNA [83] or α helix protein [84], is successfully treated

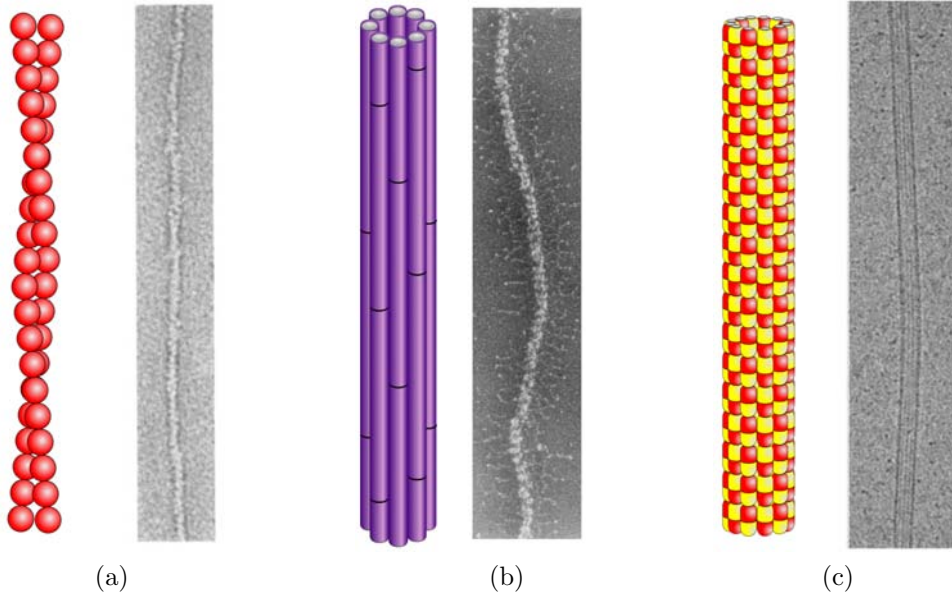


Figure 4.2: Biofilaments of the cytoskeleton. (a) Actin, (b) intermediate filaments, and (c) microtubule. (Electron micrographs are respectively from [88], [89], and [90], with permission of the publishers.)

within the framework of elasticity theory. In the case of actin filaments a member of the **cytoskeleton** family, the analytical predictions [85] of the distribution function of the end-to-end distance is in good agreement with the experimental measurements [86]. The cytoskeleton is a complex mechanical network in the cell that constitutes an important class of macromolecular biofilaments. Each member of the cytoskeleton performs different tasks in the cell [25]. **Intermediate filaments** give mechanical strength to the cell; **actin filaments** shape its contours and take part in cell locomotion; finally **microtubules** provide positional control of membrane-enclosed organelles and help intracellular transport among other functions (see section 4.1 for further details on microtubules). The function of the cytoskeletal filaments is highly dependent on *accessory proteins* such as crosslinkers, bundlers, capping and severing proteins [87]. These proteins link the components of the cytoskeleton to other structures in the cell and control their dynamics of assembly/disassembly as well.

The distinct mechanical and dynamical properties of these biofilaments arise as a result of their construction from different sets of protein subunits. In the case

4. POLYMORPHIC TUBES

of actin filaments, the subunits are globular actin proteins of size ~ 5 nm. The proteins self-assemble in the form of two stranded helical fibers of diameter 5-9 nm (see Fig. 4.2a). The intermediate filaments can be composed of different elongated subunits, vimentin being such an example [91]. They form rope-like fibers of diameters of the order of 10 nm (see Fig. 4.2b). In the case of microtubules, the subunits are called tubulins, and they self-assemble into hollow cylinders of diameter 25 nm (see Fig. 4.2c).

When we omit the torsional degree of freedom and anisotropies, the mechanical description of these filaments reduces to a simpler model which is also known as worm-like chain model, well known to the study of semi-flexible polymers. Hence the elastic properties of a filament are successfully characterized by solely the flexural rigidity $\kappa = EI$. Here E denotes the Young's modulus and I the second moment of the cross sectional area. In this formalism the deflection δ of a tube whose one end is clamped and the other is subject to a force F is given by

$$\delta = \frac{FL^3}{\alpha EI}, \quad (4.1)$$

with $\alpha = 3$.

The persistence length of a rod, which can be defined as the length over which a filament becomes flexible, is then given by the ratio of κ to thermal energy,

$$l_p = \frac{\kappa}{k_B T} = \frac{EI}{k_B T}, \quad (4.2)$$

where k_B and T denote respectively the Boltzmann constant and the temperature.

For the actin, different thermal fluctuation experiments (see section 4.1.2) have measured the persistence length l_p around $17 \mu\text{m}$ [86, 92]. However, a consensus about mechanical properties of microtubules is still lacking. But the fact that the mechanical behavior of microtubules is more complex than that of actins and intermediate filaments is not entirely surprising, since their tubular structure hints already at a higher level of complexity. In the following section we will focus on the structure of microtubules in order to understand to what extent they can be modeled as polymorphic tubes.

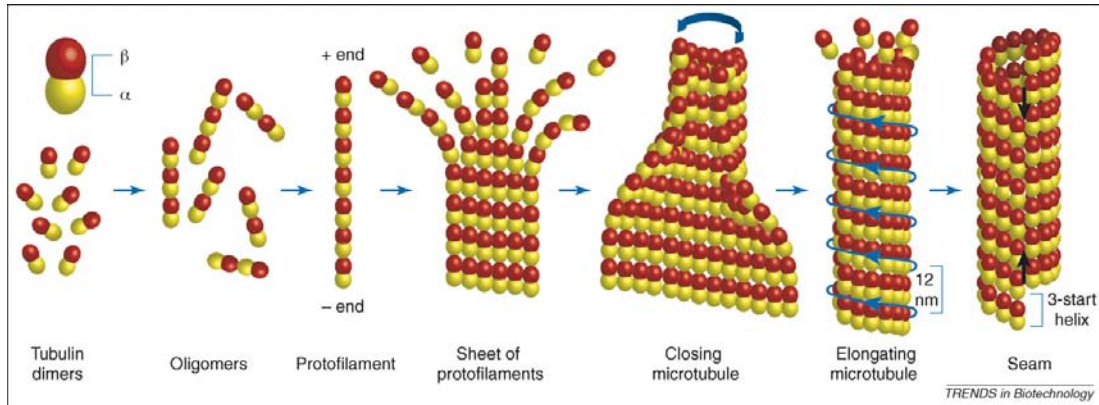


Figure 4.3: Self-assembly of microtubules (from [93] with permission of the publisher).

4.1 Microtubules

Microtubules are the stiffest of all cytoskeletal biofilaments and moreover they are highly resilient [93]. The high stiffness allows them to resist high loads whereas high resilience eases the growing of microtubules in different directions without breaking. These mechanical characteristics of microtubules enable them to perform completely different tasks in the cell. They play a central role in cell division by providing mechanical stability to the mitotic spindle. Eukaryotic cilia and flagella beat thanks to the microtubules. They also form paths for dynein and kinesin motors, hence allowing intracellular trafficking [94]. It is biologically and technology important to understand these properties which result from the anisotropic molecular structure.

4.1.1 Structure of microtubules

Microtubules are formed by cylindrical association of parallel protofilaments. The number of protofilaments can vary between 9 and 16 *in vitro*, but one usually finds 13 *in vivo* [93]. The assembly of each protofilament results from the head-to-tail binding of polar $\alpha\beta$ -tubulin heterodimer protein subunits (see Fig. 4.3). This directed arrangement of tubulin dimers endows microtubules with a structural polarity, with the plus end corresponding to the β -tubulin side, and the minus

4. POLYMORPHIC TUBES

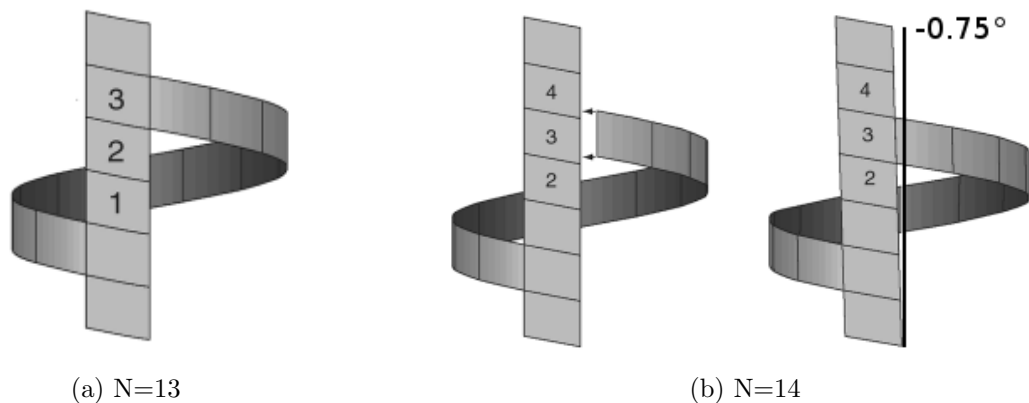


Figure 4.4: Lattice deformation in microtubules due to the seam (modified from [90] with permission of the publisher).

end to the α end. When forming a sheet (see middle figures in Fig. 4.3) homologous monomers, *i.e.*, α - α and β - β , contact each other. When closing into a tube neighboring protofilaments are slightly offset creating a **seam** (see rightmost image in Fig. 4.3) where contacts between α - β monomers are also observed. The amount of this offset is around 0.9 nm, and a microtubule with 13 protofilaments closes exactly 3 monomers above its starting point (Fig. 4.4a). This conformation is called a 3-start helix. But for instance, for 14 protofilament microtubule the offset does not match to the monomer length at the closing line. The tube accommodates this mismatch by skewing its longitudinal axis by -0.75° (Fig. 4.4b) [90].

Microtubules are dynamical filaments that polymerize and depolymerize incessantly. The mechanism of this endless reaction is captured by the **dynamic instability** model. According to this model, the dynamics is described by four parameters: the rates of polymerization and depolymerization, the frequencies of *catastrophe* and *rescue* [95], where the catastrophe means transition from polymerization to depolymerization and the rescue vice versa. Polymerization dynamics is believed to provide a structural flexibility to the cytoskeleton by allowing a rapid organization [95]. It is also noted that microtubules can generate pushing forces by polymerization and pulling forces by depolymerization [96]. Another interesting feature arising from the study of dynamic instability is the relation-

ship between (de)polymerization and geometry. The $\alpha\beta$ tubulin when integrated into the microtubule lattice hydrolyzes its bound guanosine triphosphate (GTP) molecule. Upon this reaction tubulin subunit prefers to be in a curved state directed away from the tube axis [97]. The direct consequence of the intrinsically negative curvature can be observed in the micrographs of growing microtubule tips [98]. These tips are formed by outwardly curved protofilaments of a number not yet sufficient to close as a tube. Jánosi *et al.* modeled these curved tips by an elastic sheet having different intrinsic curvatures in lateral and longitudinal directions [99]. Simplified analytical accounts and numerical calculations based on this model are consistent with the observed shapes of growing microtubule tips. This is a strong indication that intrinsically curved GDP-tubulin is geometrically confined in the cylindrical lattice and it is possibly responsible for some mechanical prestrain in the microtubule. It is also believed that this prestrain is the factor behind the initiation of rapid depolymerization, *i.e.*, catastrophe [6].

4.1.2 Experiments on microtubules

The dynamic nature of microtubule assembly forms an obstacle for *in vitro* studies of these biofilaments. The common strategy is to treat the microtubule with taxol to stop the depolymerization. It is believed that taxol achieves that by slowing down the straight-to-curved transition of microtubule dimers. But the observations of Elie-Caille *et al.* [97] suggests also that taxol treated dimers can be in different states, straight or slightly curved and occasionally strongly curved. Moreover, at longer time scales (~ 24 hours), the protofilaments are observed to form rings reminding the observer of the structure of GDP protofilaments.

The measurements of the mechanical properties of a microtubule can be divided in two broad categories: active methods and passive methods [100]. In active methods, the response of the microtubule is measured as a result of an experimentally controlled force. For instance, in the experiments reported in [101, 102] hydrodynamical flows are applied to deflect the microtubule (see Fig. 4.5 for a visualization of experimental methods).

One can also use optical tweezers to measure flexural rigidity of microtubules. In their experiments, Felgner and colleagues [104, 105] bend microtubules directly

4. POLYMORPHIC TUBES

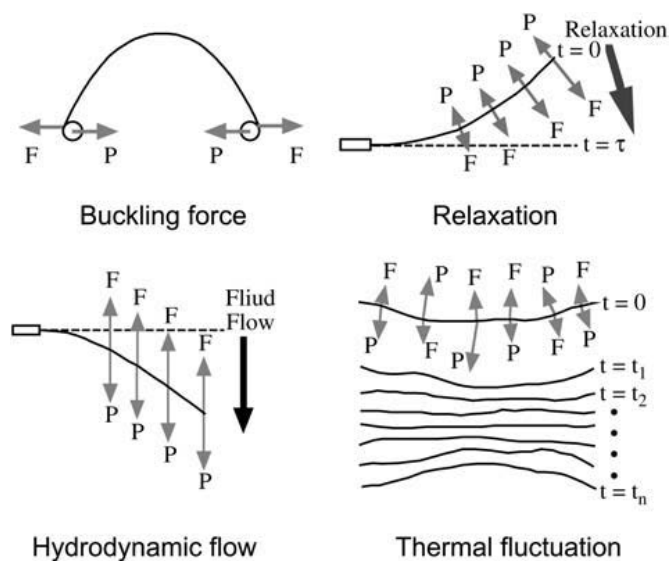


Figure 4.5: Different experimental methods applied to measure the rigidity of microtubules. P denotes external forces acting on microtubules and F denotes internal forces (from [103] with permission of the publisher).

with a laser trap and measure either the speed of the relaxation of microtubules after switching of the tweezers or the shape of maximum deflection of a microtubule moved back and forth against the surrounding buffer. Optical tweezers can also be used to apply compressive loads on microtubules by attaching polystyrene beads [103, 106, 107]. A similar buckling approach is used in [108] where the microtubules are confined in a vesicle and buckled through the tension of the vesicular membrane.

Finally, atomic force microscopy (AFM) also offers a way to apply controlled forces on microtubules [109, 110]. In these studies, the microtubules are deformed on the nanometer scale by the AFM tip, giving information mainly on local mechanical properties. However, this method is better suited to study local mechanical properties of dimers than to measure the flexural rigidity of the microtubule, which is a bulk property.

In contrast to that, in passive measurements, instead of applying external forces, mechanical information is harvested using thermal fluctuation as a force input. Due to these random thermal forces, the shape of the microtubules changes

continuously. After observing the shape of microtubules via microscopy, the shape is decomposed into Fourier cosine modes. Due to the thermal fluctuations, the amplitude of each Fourier mode fluctuates. Estimates of the flexural rigidity of the microtubules are calculated through the variance of the amplitude of each mode [102, 111, 112]. In [100] this method is extended to the measurement of the flexural rigidity of clamped microtubules whose one end is elongating.

The different measurements of the flexural rigidity κ and hence of the persistence length l_p issuing from different measurements and different methods are highly scattered. The value of κ varies between $1.9 \times 10^{-24} \text{ Nm}^2$ and $2.3 \times 10^{-23} \text{ Nm}^2$ [113]. There is also strong evidence that l_p can be a function of the tube length L [113]. These inconsistencies defy the idea that microtubules can be understood as simple Euler beam in terms of only one single elastic modulus E .

In an attempt to understand the length dependence of persistence length measurements of microtubules, an anisotropic beam model has been put forward [109, 113, 114, 115].

4.1.3 Anisotropic beam model

Since microtubules are self-assemblies of parallel protofilaments, one can expect that their mechanical properties are captured in terms of an *anisotropic fiber reinforced material* [113], well known in material science literature [116]. According to this beam model, protofilaments are considered as strong fibers weakly connected by easily shearable interfiber bonds [115]. This picture agrees with experimental results suggesting that the microtubule dimers are more strongly bound to each other in longitudinal direction than in lateral direction [109]. Hence, the bending of the microtubule does not only depend on the stretching of protofilaments (related to Young's modulus) but also has a contribution from the sliding of protofilaments with respect to each other (related to shear modulus). In this view the modeling of microtubules is similar to that of carbon nanotube ropes [117].

The quantitative description of the anisotropic beam model relates the stress to the strain by a 6×6 stiffness matrix [113]. In the case of transversely isotropic materials such as microtubules the stiffness matrix can be expressed in terms of

4. POLYMORPHIC TUBES

two 3×3 matrices [113]. First, we write the tensile/compressive stress-strain relation:

$$\begin{pmatrix} \sigma_x \\ \sigma_y \\ \sigma_z \end{pmatrix} = \begin{bmatrix} E_1 & -E_2/\nu_{21} & -E_2/\nu_{21} \\ -E_1/\nu_{12} & E_2 & -E_2/\nu_{23} \\ -E_1/\nu_{12} & -E_2/\nu_{23} & E_2 \end{bmatrix} \begin{pmatrix} \epsilon_x \\ \epsilon_y \\ \epsilon_z \end{pmatrix}, \quad (4.3)$$

where σ_i and ϵ_i are respectively the stress and the strain in the direction i . E_1 and E_2 are longitudinal and transverse Young moduli and ν_{ij} 's are Poisson ratios.

The second part is the shear-stress relation given by

$$\begin{pmatrix} \tau_x \\ \tau_y \\ \tau_z \end{pmatrix} = \begin{bmatrix} G_{13} & 0 & 0 \\ 0 & G_{13} & 0 \\ 0 & 0 & G_{23} \end{bmatrix} \begin{pmatrix} \gamma_{xy} \\ \gamma_{xz} \\ \gamma_{yz} \end{pmatrix}, \quad (4.4)$$

where τ_i denotes the shear stress in the i direction and γ_{ij} is the shear angle in the ij plane. The longitudinal and transverse shear moduli are, respectively, given by G_{13} and G_{23} . Cylindrical symmetry of the system provides $\frac{E_2}{\nu_{21}} = \frac{E_1}{\nu_{12}}$. We have also $G_{23} = \frac{E_2}{2(1+\nu_{23})}$ due to the transverse isotropy. Hence this system is composed of 5 independent elastic parameters.

When considering the deflection of a one-end-clamped beam due to a point force F at the free end, only the longitudinal Young modulus E_1 and shear modulus G_{13} are involved. With these boundary conditions the deflection is given by the sum of the bending and shear contributions [109, 113]:

$$\delta = \delta_B + \delta_S = \frac{FL^3}{\alpha E_1 I_2} + \frac{FL}{G_{13} k A}, \quad (4.5)$$

where L is the length of the free part of the tube, $\alpha = 3$ for a clamped beam, and k is a geometric correction of value 0.72 for a hollow tube and 9/10 for a filled one. $I_2 = \frac{\pi}{4}(R_o^4 - R_i^4)$ is the second moment of the cross sectional area A expressed in terms of R_i and R_o , the inner and outer radii of the tube.

If we write this deflection in terms of an effective bending modulus E_{bending} satisfying the Euler beam relation 4.1 we obtain the following elastic compliance

relation:

$$\frac{1}{E_{\text{bending}}} = \frac{1}{E_1} + \frac{\alpha}{4k} \frac{R_o^2 + R_i^2}{G_{13}L^2} \quad (4.6)$$

Now, the persistence length l_p also has a dependence on length:

$$l_p = l_p^\infty \left(1 + \frac{3E_1I_2}{G_{13}kAL^2} \right)^{-1}, \quad (4.7)$$

where $l_p^\infty = \frac{E_1I_2}{k_B T}$ denotes the persistence length in the long tube limit $L \gg \sqrt{\frac{\alpha E_1 I_2}{G_{13}kA}}$.

The AFM measurements of Kis *et al.* indicate a typical bending modulus E_{bending} of value 20 ± 10 MPa. Using Eq. 4.6 the Young modulus is calculated to be in the range $E_1 \sim 100$ MPa and the shear modulus $G_{13} = 1.4 \pm 0.4$ MPa [109]. The large difference between the two elastic moduli is at least two orders of magnitudes and can be interpreted by the highly anisotropic nature of microtubules. The same formalism allows Pampaloni *et al.* to fit the scattered data of thermal fluctuation experiments [113] and to find $l_p^\infty = 6.3 \pm 0.8$ mm and $E_1 = 1.51 \pm 0.19$ GPa. But, their prediction of the ratio between elastic moduli, E_1/G_{13} is at the order of 10^6 which appears to be unreasonably high.

4.1.4 Polymorphic tube model

Even though the anisotropic beam model predicts a length dependent persistence length which is in good agreement with experimental measurements, it does not provide a consistent framework to address all mechanical peculiarities of microtubules [6, 118].

First of all, it does not account for observations of the helicoidal microtubules reported in [102]. Moreover, the experiments of Amos and Amos based on sliding of microtubules over a glass surface suggest that microtubules are able to adopt different conformational states without the intervention of an external force [119]. As noted above, the prediction of extremely small shear modulus contradicts the observation that interprotofilament bonds do not displace significantly with respect to each other [120].

4. POLYMORPHIC TUBES

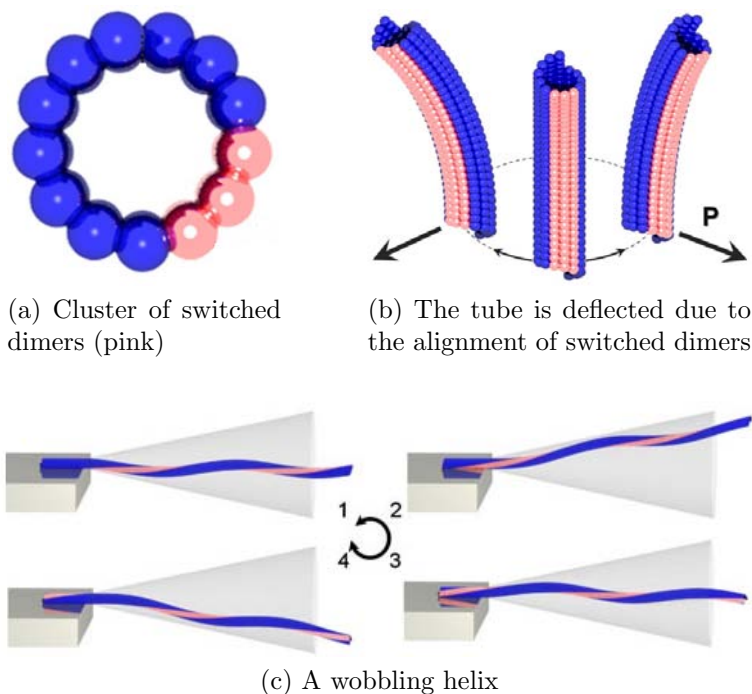


Figure 4.6: Polymorphic tube model (modified from [6] with permission of the publisher).

Another shortcoming of the anisotropic model lies in the anomalous dynamics of microtubules. For instance, Brangwynne *et al.* report unexpectedly large relaxation times for microtubules shorter than $\sim 20 \mu\text{m}$ [92]. The shear based beam model requires an internal dissipation to be posited to account for the unusual dynamics of microtubules [6].

In an attempt to interpret different aspects of microtubule mechanics in a compact scenario, Mohrbach *et al.* [6, 118] propose a completely radical tube model based on two hypotheses:

1. The taxol-GDP-tubulin dimer is multistable, having at least two equilibrium states: one straight and the other curved, with the curved state being more favorable.
2. The tubulin dimer states interact cooperatively along a protofilament.

According to the first hypothesis a free tubulin dimer which is preferably in the curved state will be forced to obey the elasticity of a cylindrical lattice

when integrated into one ring of a microtubule section. For such a section of a microtubule, a switched dimer on one side of the lattice will hinder the switching of the dimers on the opposite side. On the contrary, a dimer whose neighbor is already in a curved state will switch rather easily since the lattice is already frustrated at this site. The competition between these interactions would lead to a cluster of curved dimers on one side of the tube, whose direction is decided by spontaneous symmetry breaking (see the pink units in Fig. 4.6a). But since any direction is equivalent for this deflected geometry, it will be a highly degenerate state. Therefore, the block of switched dimers can be displaced azimuthally on the tube surface at small cost.

For a tube with more than one annular cross section, without the second hypothesis, the stacks of tube sections would be bent in random directions, canceling the deflection of each other at larger scale. The cooperativity would align these blocks on the same side of the lattice resulting in a macroscopic deflection of the tube (see the tubes in Fig. 4.6b). But since the lattice of microtubules are intrinsically twisted, the cooperatively interacting curved dimers along a protofilament will twist around the tube leading to a helical ground state whose pitch should match lattice the twist repeat length (see the tubes in Fig. 4.6c). But as in the case of one section, this conformation will be degenerate in N different orientations, N being the number of protofilaments. Clamping one such tube would result in the **wobbling** motion which is indeed alternating between degenerate deflection orientations.

This model implies a complex persistence length that shows an oscillatory behavior for intermediate length scales, of the form:

$$l_p(L) = aL + b \sin(q_0 L), \quad (4.8)$$

where a , b are parameters derived from the elasticity of the tube and q_0 is the lattice twist. The prediction of the model for the relaxation dynamics scales cubically with the length, $\tau \sim L^3$, in contrast to relaxation times of semiflexible polymers scaling with $\tau \sim L^4$. These predictions of the static and dynamics properties of the microtubule mechanics appear to conform to experimental results [6, 118].

4.2 Numerical model

We have already seen that a discretized two-dimensional membrane model is successfully used by Jánosi *et al.* [99] to study curved microtubule tips. In this model, the anisotropy of the microtubule walls is responsible for the final shape of the tips, which arises as a result of the balance of the tug-of-war between two intrinsic curvatures with opposite signs. A somewhat similar elastic competition can be seen in the polymorphic tube model presented in the previous section. It starts from discrete multistable components and constructs a tube by incorporating the cooperativity of its constituents. In both models, the mechanics is governed by the competition of incompatible effects. Here, we aim to present a numerical model to reconcile these two approaches. By incorporating the ideas of multistability and cooperativity into an elastic lattice, we will investigate the symmetry breaking of rod-like objects.

We build our system out of basic units composed of two squares as depicted in Fig. 4.7a, with sides of length d . We will construct a tube by tiling many of these dimers in a cylindrical lattice. Like the majority of the microtubules, we set the number of protofilaments to $N = 13$ but for the sake of generality, we do not introduce any irregularities into the lattice such as a seam or an internal twist. In Fig. 4.7b an example of such a construction is visualized: the blue strip shows a protofilament of 5 dimers and the pink strip is the smallest possible tube section formed by laterally neighboring 13 dimers.

As in previous studies of discrete models of elastic membranes [18, 99], we will enforce elastic properties through the stretching and bending of bonds. Basically, we differentiate two directions in the lattice: the vertical being along the protofilaments (blue in Fig. 4.7b), and the horizontal follows the cylinder surface laterally (pink in Fig. 4.7b). For the rectangular subunit, we identify two types of horizontal bonds. The upper and lower horizontal bonds combine two rectangular units along a protofilament, we will call them type B_1 bonds. The type B_2 bonds are the horizontal bonds in the middle separating the subunit into two squares. It is the bending of these bonds that will differentiate between the straight and curved states of a subunit. The vertical bonds are shared by two laterally neighboring dimers, they are of type B_3 .

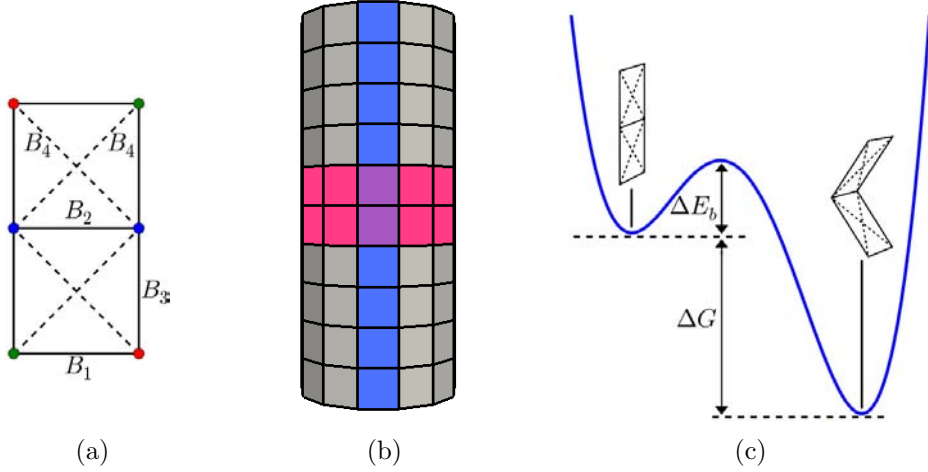


Figure 4.7: Construction of the polymorphic tube. (a) A rectangular subunit is divided into two squares by bonds B_2 . Ghost diagonals B_4 are added for rigidity. (b) Tubular assembly of subunits. One ring of lateral neighbors is colored in pink. One protofilament formed by longitudinal neighbors is colored in blue. (c) Asymmetric double well potential for the bonds B_2 . ΔG denotes the energy difference between the straight and curved states. ΔE_b is the height of the barrier with respect to the straight state.

As such our lattice is not rigid, since it is made of quadrilateral components solely. To enforce the rigidity, we will triangulate it by the addition of right and left directed “ghost” diagonals (depicted by dashed lines in Fig. 4.7a). Since we avoid any anisotropy other than the distinction between the vertical and the horizontal, we will assign similar properties to these ghosts and we will call all of them B_4 bonds. The stretching of ghost bonds will control the shearability of each square on the one hand, and the bending will ensure the planarity of the square’s four vertices on the other hand. Note also that subunits share two bonds of type B_3 laterally and one bond of type B_1 longitudinally. It is the rigidities of these bonds that will restrain the multistable nature of the dimers.

We express the resistance of bonds to be stretched by harmonic potentials. For all bonds \mathbf{d} , the stretching energy is given by

$$E_{\text{stretching}} = \frac{1}{2} \mu_{si} (|\mathbf{d}| - d_i)^2, \quad i = 1, 2, 3, 4, \quad (4.9)$$

4. POLYMORPHIC TUBES

where d_i are the preferred lengths of the bonds in the straight cylindrical state as in Fig. 4.7b. μ_{si} are the stretching rigidities. The values of the stretching rigidities will be expressed in units of $k_B T/b^2$, where b denotes the unit length in the system.

Similarly, we assign quadratic bending energies for the hinges defined by bonds:

$$E_{\text{harm}} = \frac{1}{2} \mu_{bi} (s - s_i)^2, \quad i = 1, 3, 4, \quad (4.10)$$

where the sine of the angle between the normals \mathbf{n} of two adjacent triangles a and b at bond \mathbf{d} is $s = (\mathbf{n}^a \times \mathbf{n}^b) \cdot \frac{\mathbf{d}}{|\mathbf{d}|}$. For the preferred values of s_i we set the sine's corresponding to the cylindrical state, and μ_{bi} are the bending rigidities. The values of the bending rigidities will be expressed in units of $k_B T \times b$.

The bistability of the dimers is achieved via the bending properties of the bonds B_2 . We choose a quartic bending potential having one minimum at $s = 0$ with zero energy and a second one at $s = s_2$ with energy $\Delta G < 0$:

$$E_{\text{anharm}} = As^4 + Bs^3 + Cs^2, \quad (4.11)$$

where the coefficients A , B , and C are all functions of the energy difference ΔG , the barrier ΔE_b , and the sine of the curved state is s_2 (see Fig. 4.7c).

The last term in the energy is the cooperativity between the bonds B_2 along a protofilament:

$$E_{\text{cooperativity}} = \mu_c (s - s_{\text{next}})^2 + \mu_c (s - s_{\text{prev}})^2, \quad (4.12)$$

where μ_c measures the strength of the cooperative interaction between a bond B_2 and its neighbors B_2 -next and B_2 -previous.

We will integrate this system in time using Brownian Dynamics method (see appendix E for the details of the simulations).

4.3 Results

4.3.1 One ring of dimers

The simplest tube one can construct consists of a closed ring of dimers. We will first try to understand for this case how the anharmonic potential of a dimer competes with the elasticity of the lattice. In order to reduce the complexity of the parameter space we set the stretching rigidities of horizontal and vertical bonds as $\mu_s = \mu_{s1} = \mu_{s2} = \mu_{s3}$. We will use μ_s as the control parameter for the mechanical behavior of the tube. The other parameters are set conveniently to prevent the tube from collapse and ensure numerical stability (see appendix E for details).

For sufficiently large values of μ_s (at the order of 10^5), the elasticity of the lattice suppresses the preference for the curved state of the free dimer: the tube maintains its cylindrical form. If, on the contrary, the value of μ_s is small (2×10^4), the curved state dominates the lattice structure; all dimers switch to a curved configuration. We will call such a kind of cluster of switched dimers a **confoplex** in the following. In this fully switched confoplex state, the tube still conserves its cylindrical symmetry but now its shape is catenoid-like having a negative curvature along the vertical direction and positive curvature along the circumferential direction (see Fig. 4.8a). Although the dimers are now in the curved state, they are still slightly frustrated: they cannot reach their preferred target angle exactly since all the other terms of the system favor a cylindrical section. The resulting catenoidal shape is still a compromise between the anharmonic term and the other contributions.

Between these two configurations, there exists another state in the configuration space. For instance, when the stretching rigidity equals $\mu_s = 4 \times 10^4$, the cylindrical symmetry is broken. On one side of the tube, we observe that two dimers are almost fully switched to the curved state (see Fig. 4.8b). The dimers of the opposite wall are slightly deflected inwards. Along the tube surface, the angles of the bonds of type B_2 change sign gradually from one side to the other. This *partial confoplex* state is similar to the blocks of switched dimers (Fig. 4.6a) of the polymorphic microtubule model but in our case states of subunits are not

4. POLYMORPHIC TUBES

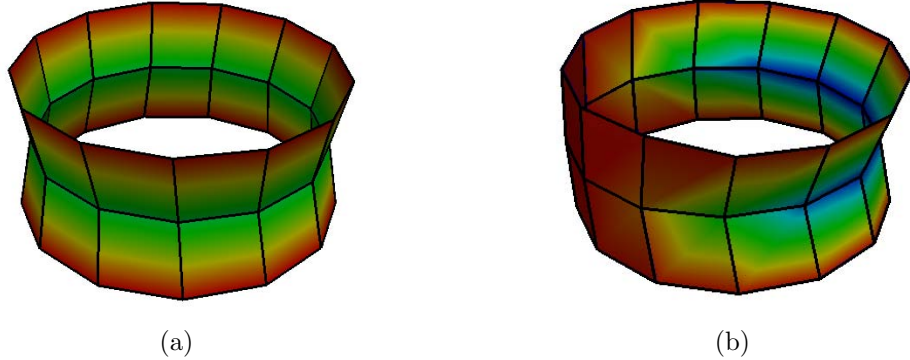


Figure 4.8: Two configurations for one ring of dimers. (a) A full confoplex for which all dimers are in the curved state. (b) A partial confoplex. The symmetry is broken due to a non uniform angular distribution along the bonds B_2 .

Ising-like; the angles change continuously.

Simple model

The transitions of the simple system from one state to another can be understood qualitatively using a reduced model. We observe for all three states, *i.e.*, cylinder, partial and full confoplexes that horizontal bonds form polygons which are close to circles. Hence, we approximate these three polygons by three parallel circles C_1 , C_2 , and C_3 as depicted in Fig. 4.9. For simplicity, we fix lower and upper circles C_1 and C_3 in space and in shape. Hence they are unstretchable with constant radius R . We do not take into account the stretching of vertical bonds, since this is a higher order effect in the deformation. The only free component in this simplified view is the circle C_2 . Its center is free to move along the x axis. It can be stretched as well with an energy cost proportional to a rigidity μ_{C_2} .

With these specifications the geometry of the system is expressed as a function of ΔR and Δx in the polar angle ϕ :

$$\begin{aligned}
 C_1 &: (R \cos(\phi), R \sin(\phi), 0), \\
 C_2 &: ((R - \Delta R) \cos(\phi) + \Delta x, (R - \Delta R) \sin(\phi), 1), \\
 C_3 &: (R \cos(\phi), R \sin(\phi), 2).
 \end{aligned} \tag{4.13}$$

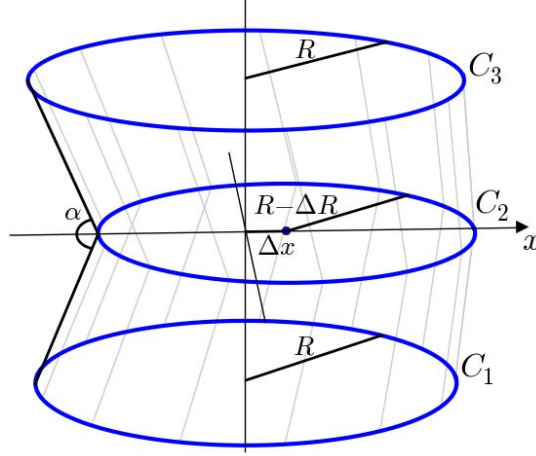


Figure 4.9: Simple model consists of three parallel circles. C_1 and C_3 are fixed in space and in size. C_2 can move along the $+x$ direction, and can shrink its radius by ΔR .

The stretching energy depends only on the perimeter of C_2 and therefore is independent of the displacement Δx .

$$E_s = \mu_{C_2}(2\pi\Delta R)^2. \quad (4.14)$$

In order to oppose to this stretching energy, we will define a bending energy associated to the surfaces lying between these three circles. Therefore, at each angle ϕ we calculate the sine of the angle α defined by the lines $\overline{C_2C_1}$ and $\overline{C_2C_3}$:

$$\sin \alpha = -\frac{2(\Delta R - \Delta x \cos(\phi))}{1 + (\Delta R)^2 + (\Delta x)^2 - 2\Delta R\Delta x \cos(\phi)}. \quad (4.15)$$

At first order in ΔR and Δx , this equals

$$\sin \alpha \approx -2(\Delta R - \Delta x \cos(\phi)). \quad (4.16)$$

Now, we express the bending energy density as a double well potential similar

4. POLYMORPHIC TUBES

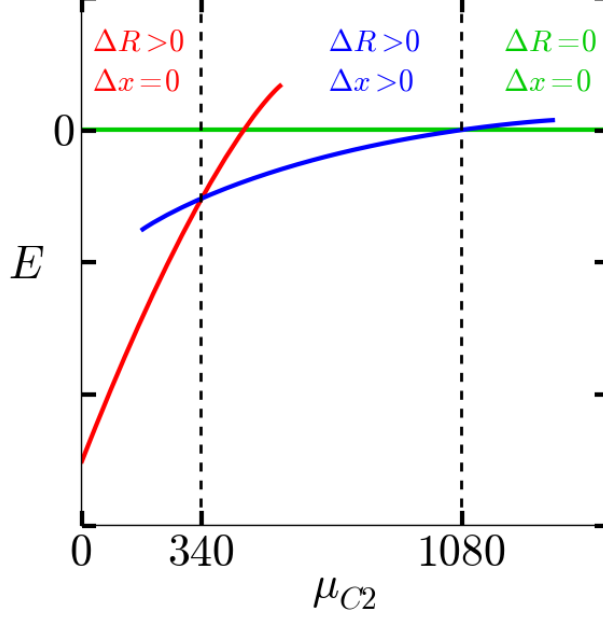


Figure 4.10: Energy as function of stretching rigidity for different minima of the simple model.

to the one used in the simulations and we integrate it along the C_2 contour:

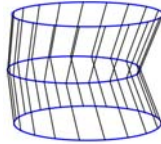
$$\begin{aligned}
 E_b &= \oint_{C_2} d\phi [A(\sin \alpha)^4 + B(\sin \alpha)^3 + C(\sin \alpha)^2] \\
 &= 4\pi [(2C(\Delta R)^2 - 4B(\Delta R)^3 + 8A(\Delta R)^4 + C(\Delta x)^2 \\
 &\quad + 3A(\Delta x)^4 - 6B(\Delta R)(\Delta x)^2 + 24A(\Delta R)^2(\Delta x)^2] . \quad (4.17)
 \end{aligned}$$

We solve the system $\frac{\partial E}{\partial(\Delta R)} = 0$ and $\frac{\partial E}{\partial(\Delta x)} = 0$ to find the extrema of the total energy $E = E_s + E_b$. Comparing the energies of solutions we determine the global minimum of the system (see Fig. 4.10). We observe that the ground state of the system admits three different configurations as a function of the rigidity μ_{C_2} :

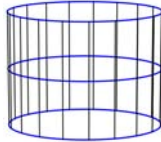
- For $\mu_{C_2} \in [0, 340]$, since the middle circle is easily stretchable, the tube minimizes its bending energy by shrinking its radius by ΔR , and the displacement Δx is not necessary. Hence the ground state has $\Delta R > 0$ and $\Delta x = 0$ corresponding to a catenoid-like shape:



- For $\mu_{C_2} \in [340, 1080]$, it is harder for C_2 to shrink. In order to satisfy the bending term, it shifts its center by Δx . So, the global minimum is found for finite ΔR and Δx , resulting in a partial switch:



- For $\mu_{C_2} > 1080$, the stretching of C_2 dominates the bending energy completely. The ground state has both vanishing ΔR and Δx . The tube keeps its cylindrical form:



Not surprisingly, this analytically solvable model does not predict the correct transition values, given its simplicity; nonetheless it provides a qualitative explanation for the observed morphologies in the simulation.

4.3.2 Longer tubes

In the previous section we were interested in the simplest tube having protofilaments with only one subunit. For longer protofilaments the previously irrelevant parameters of the cooperativity, μ_c , and the bending rigidity μ_{b1} of the horizontal B_1 bonds will have an effect on the tube conformation. For vanishing values of these parameters, each section of a long tube is expected to behave almost independently¹. Hence, we do not observe any long range interactions that could

¹However, they are still coupled to each other by the stretching μ_{s1} of bonds B_1 , this is why they are not completely uncorrelated.

4. POLYMORPHIC TUBES

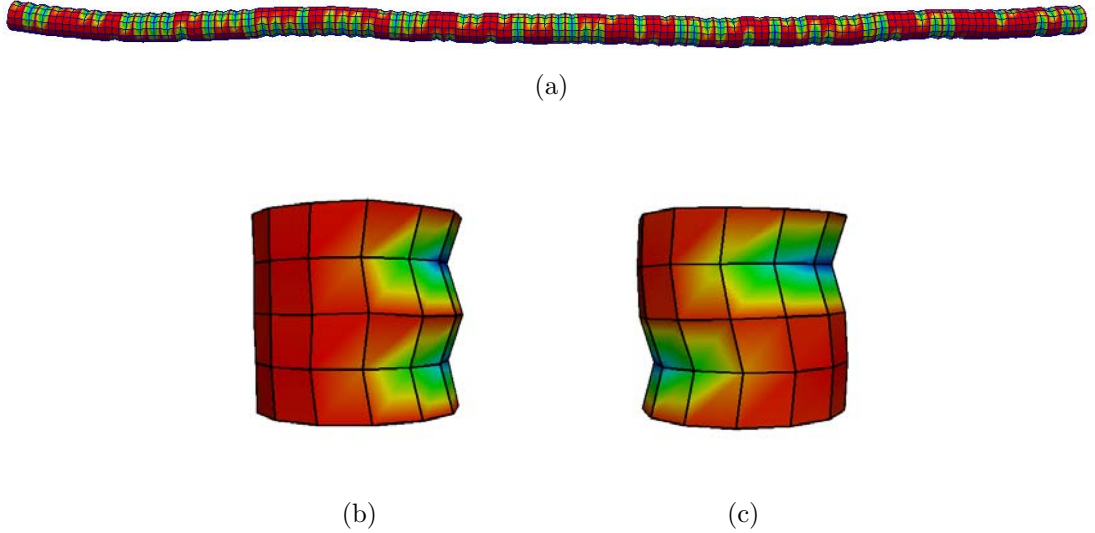
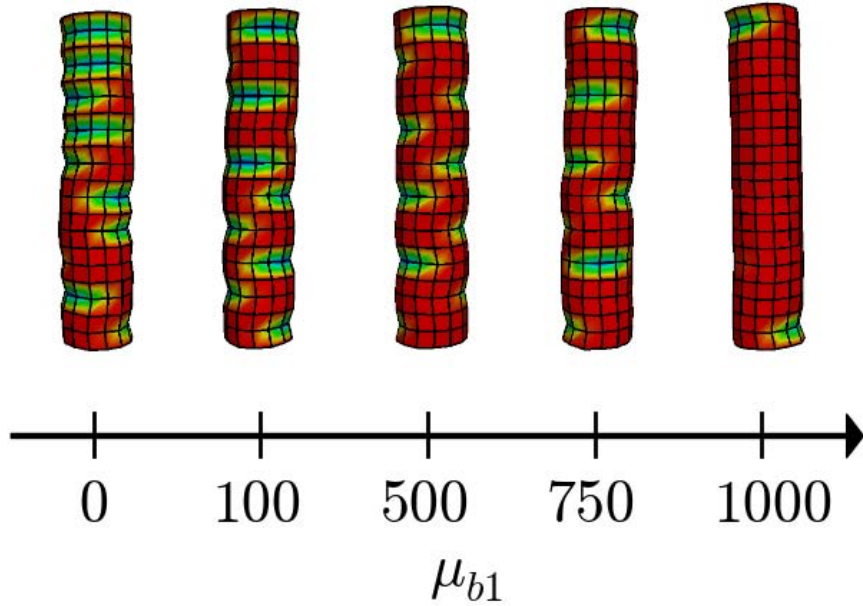


Figure 4.11: Configurations for long tubes. (a) A relatively long tube having 80 dimers on each of its protofilaments with $\mu_{b1} = 0$ and $\mu_c = 0$. Sections are oriented independently. The temperature of the system is $8T$. Two neighboring partial confoplexes in (b) aligned and (c) opposite configurations.

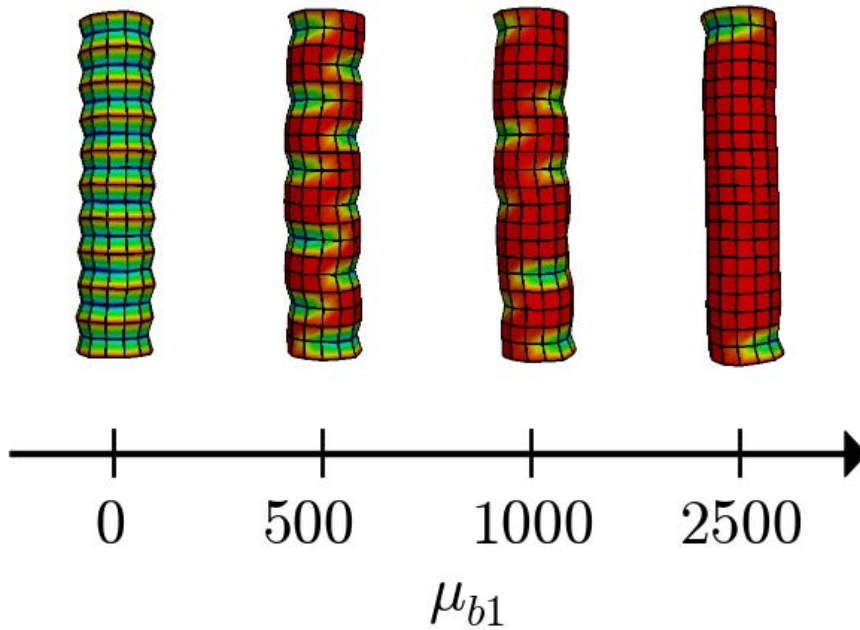
induce a global symmetry breaking. This can be seen in Fig. 4.11a where a tube composed of 80 partial confoplex sections is depicted.

Bending rigidity at the interface of two confoplexes

When we switch on either μ_{b1} or μ_c the states lying in the range between the aligned configuration (Fig. 4.11b) and the opposite (Fig. 4.11c) will have different energies. For the case of μ_{b1} (*i.e.*, the cooperativity $\mu_c = 0$) the difference is due to the angles created between two sections which have a non vanishing cost if the tube is not straight. The effect of this term on a tube assembled from partial confoplexes can be seen in the diagram Fig. 4.12a. At low values, *e.g.* at $\mu_{b1} = 100$, each section conserves still its partial confoplex configuration but they are never observed on top of each other. This suggests that the aligned state is not preferred by neighboring confoplexes; they repel each other in terms of orientation. For larger values of μ_{b1} , however, the strength of the horizontal bending starts to interfere with the other terms in the system. At $\mu_{b1} = 500$ the confoplexes become smaller in size, and when the value of the horizontal bending



(a) partial confoplex to straight



(b) full confoplex to straight

Figure 4.12: The effect of the horizontal bending μ_{b1} . (a) With increasing μ_{b1} partial confoplexes start to repel each other. For larger values, they shrink in size and disappear ($\mu_s = 4 \times 10^4$). (b) Similar behavior can be observed for full confoplexes ($\mu_s = 2 \times 10^4$).

4. POLYMORPHIC TUBES

rigidity reaches $\mu_{b1} = 750$, they are even smaller. When $\mu_{b1} = 1000$, the tube can only be switched on the edges where the lattice constraint is obviously weaker than in the bulk (see Fig. 4.12a).

A similar behavior can be observed for full confoplexes. With vanishing μ_{b1} , a tube formed by 10 dimer protofilaments is shown in the leftmost part of the diagram depicted in Fig. 4.12b. When we increase μ_{b1} to 500 the positive curvature created at the conjunction of two neighboring catenoid-like sections has a large cost. So, the sections which would be in full confoplex state when apart, are forced to be converted to partial confoplexes when self-assembled. For $\mu_{b1} = 1000$, we again observe that the confoplexes are reduced in size and at $\mu_{b1} = 2500$, the tube is cylindrical again (see rightmost image in Fig. 4.12b).

To see why the orientations of neighboring confoplexes are repulsive, we can have again recourse to the circular approximation of the tube sections. To see the interactions of two confoplexes, we will need five circles, three fixed ones (odd numbered circles) and two mobile ones (even numbered):

$$\begin{aligned}
 C_1 &: (R \cos(\phi), R \sin(\phi), 0), \\
 C_2 &: ((R - \Delta R) \cos(\phi) + \Delta x, (R - \Delta R) \sin(\phi), 1), \\
 C_3 &: (R \cos(\phi), R \sin(\phi), 2), \\
 C_4 &: ((R - \Delta R) \cos(\phi) + \Delta x \cos(\theta), (R - \Delta R) \sin(\phi) + \Delta x \sin(\theta), 3), \\
 C_5 &: (R \cos(\phi), R \sin(\phi), 4).
 \end{aligned} \tag{4.18}$$

The lower section of the tube is switched by the action of the circle C_2 and the upper one by that of the circle C_4 . The upper confoplex switches the same way as the lower one, but its orientation is not necessarily in the direction of $+x$. This feature is represented by the new parameter θ in Eq. 4.18, which denotes the angle between the orientations of two confoplexes:

- for $\theta = 0$, two confoplexes are perfectly aligned (see the lower inset in Fig. 4.13);
- whereas for $\theta = \pi$, they are oriented in opposite directions (see the upper inset in Fig. 4.13).

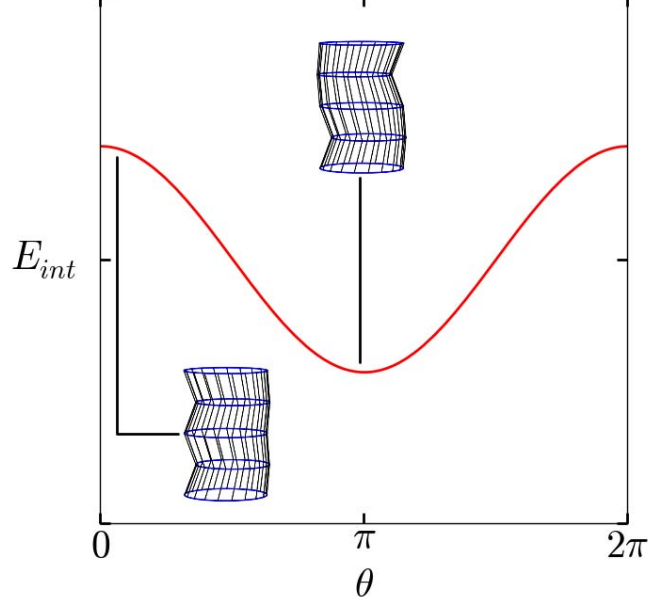


Figure 4.13: The interaction energy E_{int} as function of θ . $\theta = 0$ correspond to the aligned confocalplexes while $\theta = \pi$ means that confocalplexes face opposite directions.

To define an interaction potential we write the sine of the angle between the surfaces formed by the circle couples $C_2 - C_3$ and $C_2 - C_4$:

$$\sin \beta = \frac{2\Delta R - \Delta x[\cos(\theta - \phi) + \cos(\phi)]}{\sqrt{(1 + \Delta x^2 + \Delta R^2 - 2\Delta R\Delta x \cos(\phi))(1 + \Delta x^2 + \Delta R^2 - 2\Delta R\Delta x \cos(\theta - \phi))}}. \quad (4.19)$$

Again, for analytical tractability, we expand $\sin \beta$ at first order in ΔR and Δx :

$$\sin \beta \approx 2\Delta R - \Delta x[\cos(\theta - \phi) + \cos(\phi)]. \quad (4.20)$$

We define the interaction potential as the integral of $\sin \beta$ around the contour of the circle C_3 :

$$\begin{aligned} E_{\text{int}} &= \mu_b \oint_{C_3} d\phi (\sin \beta)^2 \\ &\approx 2\pi\mu_b (4\Delta R^2 + \Delta x^2 \cos(\theta) + \Delta x^2), \end{aligned} \quad (4.21)$$

4. POLYMORPHIC TUBES

where in the second line we used the Eq. 4.20.

Now we assume that the value of μ_b is sufficiently smaller than the stretching rigidity μ_s and the anharmonic potential, hence it does not interfere with the partial confoplex configuration. So for a given confoplex state with constant $\Delta R > 0$ and $\Delta x > 0$, E_{int} is cosine. Fig. 4.13 pictures a typical curve for E_{int} as a function of relative confoplex orientation θ ¹. Therefore, the minimum is reached at $\theta = \pi + 2\pi k, k \in \mathbb{Z}$, that is to say, when two confoplexes are oriented in opposite directions.

This analysis shows that for a global symmetry breaking, the system needs some cooperative interaction between neighboring sections to compensate the repulsive interactions.

Cooperativity

The cooperativity μ_c we introduce in the longitudinal direction is minimized when the angles of the bonds B_2 of nearest neighbors along a protofilament have the same value. When all dimers are switched (full-confoplex) or none of them are switched (cylindrical), this term obviously implies no effect. However, since the angle distribution is not isotropic for partial confoplexes, they have to align their directions in order to satisfy the cooperativity term. Therefore, this term can be seen as an attractive interaction between the confoplexes in contrast to the repulsive interaction due to the horizontal bending μ_{b1} .

When we introduce a weak cooperativity into the system, we observe that confoplexes have a tendency to “stick” to each other, organizing at small scale with a helicoidal-like order of fluctuating handedness (a snapshot can be seen in Fig. 4.14a). The pitch of these helices is at the order of few dimers, much smaller than the tube length. Therefore, right and left handed helices cancel each other on long scales and the tube appears straight. For the same weak cooperativity, if we decrease the value of μ_{b1} , the confoplexes have more success in aligning their orientations, although this does not lead to a complete alignment (see Fig. 4.14b). The switched dimers follow a helicoidal path on the tube surface, causing the centerline of the tube to be in a helix shape. The pitch of the helicoidal path is

¹A similar behavior is observed if we use the exact form Eq. 4.19 instead and integrate it numerically.

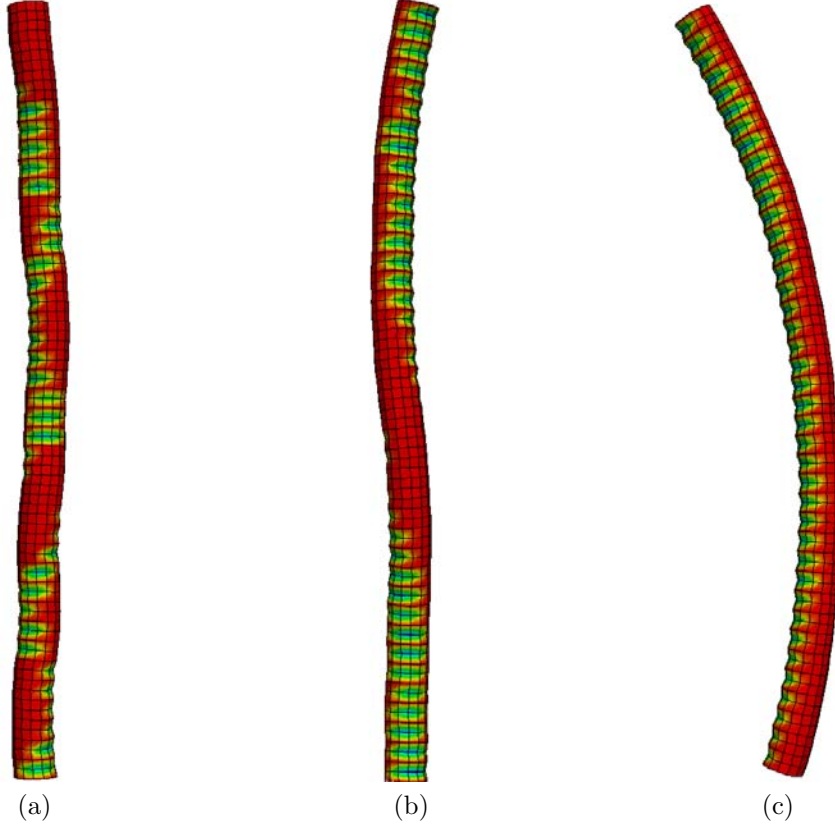


Figure 4.14: Cooperative confoplexes with protofilaments having 40 dimers. (a) The repulsive interactions are dominant when $\mu_c = 50$ and $\mu_{b1} = 300$. (b) For weaker repulsiveness, at $\mu_c = 50$ and $\mu_{b1} = 200$ a long scale order emerges. (c) At high cooperativity, $\mu_c = 250$ and $\mu_{b1} = 100$, the tube deflected to a C-like shape.

at the order of tens of dimers, comparable to the tube length in Fig. 4.14b where each protofilament has 40 dimers.

For weak μ_{b1} and high strengths of μ_c , the cooperativity becomes more pronounced than repulsive interactions of confoplex orientations. The dimers switch coherently along the protofilaments: partial confoplexes are put on top of each other. The pitch of helicoidal order now becomes very large and exceeds the size of the tube depicted in Fig. 4.14c. The result is a nicely bent tube having a C-like shape deflected towards a randomly chosen direction.

When both μ_c and μ_{b1} have significant values, the tube cannot keep this configuration anymore. The tube switches back to the cylindrical state (similar

4. POLYMORPHIC TUBES

to what happens in Fig. 4.12) with only few sections switched on the boundaries.

4.4 Conclusion

Tiling multistable components into a cylindrical sheet, we constructed a tube model which lends itself to be studied computationally. We showed that, as a result of the competition between different elastic terms in the system, each cross section of the tube is able to adopt at least three distinct configurations. Two of these configurations are cylindrically symmetric. The last one is the most interesting one since its symmetry is broken.

For tubes composed of many of these non-symmetric sections, we observed that the relative orientation of successive sections can be controlled by cooperative and repulsive interactions along the protofilaments of the tube. When repulsive interactions are stronger, the sections of the tube switch in opposite directions; their local deflections neutralize each other on long scales. When the attractive forces start to counterbalance the repulsive ones they first have tendency to stick locally. For sufficiently high cooperativity, the global contour is deflected towards a randomly chosen direction reminiscent of the Euler buckling of rods. However, in our case buckling is not caused by an external load but it emerges due to the internal organization of the constituents.

In conclusion, starting from few microscopic principles, we constructed an elastic tube capable of adopting multiple configurations. We demonstrated its ability to generate intrinsic curvatures confirming the insights of the related theoretical model explored in [6, 118]. One direction for further analysis is to study the response of the polymorphic tube to external forces and torques as well as its dynamical features. The effects of system specific properties are also worth studying. One can easily think of incorporating a seam and an internal twist for microtubules and an internal core for coiling rods. The latter can also be relevant to manufactured soft robotics systems [121].

Chapter 5

Final remarks

Throughout this manuscript, we presented our efforts to gain some physical insight into the problems gathering around the question “how biological objects get their shape?” In particular, we were interested in the morphogenesis of slender and thin structures constrained by internal or external factors. Our purpose was not to explain the very specifics of particular systems, but to provide basic mechanisms as generators of shape patterns that would constitute the building blocks of complex morphologies. We thus aimed to tie the mechanics to the geometry, wishing to extract universal features.

We have found the motivation for our models in various biological context on different scales, such as growing soft tissues, invaginations of membranes or microtubules. We constrained ourselves to make these models as simple as possible yet complex enough to grasp non trivial aspects. The dimensional properties of the objects we addressed granted us an approach based on the mechanics of surfaces. Under this general framework, we made use of various approaches especially numerical simulations. We profited from analytical calculations and some experimental results as well in Chapter 2.

In the future, a more comprehensive approach merits to be developed through the combination of external and internal constraints. A systematic study of the response to external loads and the stability of the dipoles we treated in Chapter 2 may be of interest for practical applications. One can also think to study the interactions of polymorphic tubes with membranes, which is undoubtedly relevant for many biological processes. In the same direction, the invaginations

5. FINAL REMARKS

of membranes enriched by proteins is a subject that still needs to be modeled in simple terms although it will pose new challenges on the computational level.

Appendix A

Parametrization of a surface

As depicted in Fig. A.1, we parametrize the surface Ω by the local coordinates (s^1, s^2) and describe its position vector by the map $\mathbf{x} : \mathbb{R}^2 \rightarrow \mathbb{R}^3$. The covariant surface basis vectors are given by the derivatives with respect to the curvilinear coordinates [21]:

$$\mathbf{a}_\alpha = \frac{\partial \mathbf{x}}{\partial s^\alpha} = \mathbf{x}_{,\alpha}, \quad (\text{A.1})$$

where the comma denotes the partial derivative. The covariant and contravariant components of the metric tensor are

$$a_{\alpha\beta} = \mathbf{a}_\alpha \cdot \mathbf{a}_\beta \quad a^{\alpha\beta} = \mathbf{a}^\alpha \cdot \mathbf{a}^\beta. \quad (\text{A.2})$$

The normal \mathbf{d} of the surface and the surface Jacobian \sqrt{a} are constructed as

$$\sqrt{a} := |\mathbf{a}_1 \times \mathbf{a}_2| \quad \text{and} \quad \mathbf{d} = \frac{\mathbf{a}_1 \times \mathbf{a}_2}{\sqrt{a}}. \quad (\text{A.3})$$

The symmetric curvature tensor $\overleftrightarrow{\mathbf{B}}$ has the components:

$$b_{\alpha\beta} = -\mathbf{d}_{,\alpha} \cdot \mathbf{a}_\beta = \mathbf{d} \cdot \mathbf{a}_{\alpha,\beta} = b_{\beta\alpha}. \quad (\text{A.4})$$

A. PARAMETRIZATION OF A SURFACE

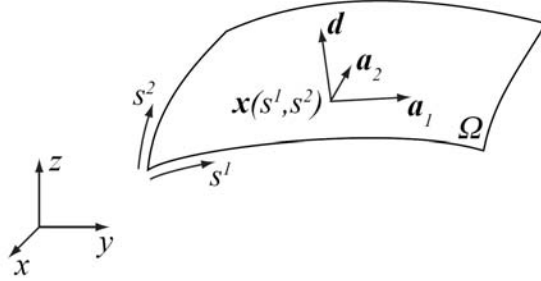


Figure A.1: Surface parametrization

The mean curvature is defined as one half of the trace of the curvature tensor:

$$H = \frac{1}{2} \text{tr}(\overleftrightarrow{\mathbf{B}}) = \frac{1}{2} b_{\alpha}^{\alpha} = -\frac{1}{2} \mathbf{a}^{\alpha} \cdot \mathbf{d}_{,\alpha} , \quad (\text{A.5})$$

and the Gaussian curvature is given by the determinant of the curvature tensor

$$K = \det(\overleftrightarrow{\mathbf{B}}) = |b_{\beta}^{\alpha}| . \quad (\text{A.6})$$

Appendix B

Harmonic approximation for dipole defects

Assuming that $\Psi/2\pi \ll 1$, we can expand the curvature $\kappa(s)$ and the constants C and M in powers of $\epsilon = \sqrt{-k}$:

$$\kappa = \kappa_1 + \kappa_3 + \dots; \quad M = M_0 + M_2 + \dots; \quad C = C_0 + C_2 + \dots. \quad (\text{B.1})$$

For vanishing $\epsilon \rightarrow 0$ we have $\mathcal{K}[0] = \frac{\pi}{2}$ and $\text{sn}[[m s, 0]] = \sin(m s)$. The equilibrium states are small oscillations around a flat configuration with $\kappa = 0$. The harmonic approximation of the quadrature 2.22 about $\kappa = 0$ reads

$$M_0^2 - C_0^2 + 2M_0M_2 - 2C_0C_2 = (\kappa_1')^2 + (1 - C_0)\kappa_1^2. \quad (\text{B.2})$$

The arc length s matches the azimuthal angle φ at lowest order. Hence the curvature can be written for a loop, vanishing at boundaries $\varphi = 0$ and at L_0 as

$$|\kappa_1| \approx A_1 \sin\left(\frac{\pi n \varphi}{L_0}\right), \quad (\text{B.3})$$

B. HARMONIC APPROXIMATION FOR DIPOLE DEFECTS

where the amplitude A_1 is a constant. Using Eq. 2.27, we see that the amplitude equals $A_1 = \frac{2\pi n}{L_0} \sqrt{-k}$.

The approximation of the quadrature gives the two zeroth order identities

$$C_0 = 1 - \left(\frac{n\pi}{L_0}\right)^2, \quad M_0^2 = C_0^2, \quad (\text{B.4})$$

where M_0 is positive which follows from the expansion of Eq. 2.29. However, the sign of C_0 can be positive or negative depending on whether $n\pi$ is bigger or smaller than L_0 (see below).

We also have the relation

$$2(M_0 M_2 - C_0 C_2) = A_1^2 (1 - C_0) \quad (\text{B.5})$$

from the Eq. B.2 and thus

$$A_1^2 = \frac{-2C_0}{1 - C_0} [-M_2 \text{sign}(C_0) + C_2]. \quad (\text{B.6})$$

The last equation is a constraint imposed on the second order terms M_2 and C_2 . One can check the consistency of Eqs. B.4 and B.6 by expanding the nonlinear expressions for C and M provided in Eqs. 2.28 and 2.29, in $\sqrt{-k}$ as well.

The amplitude A_1 of the curvature depends on the ratio of arc length to polar angle over the trajectory of the solution on the unit sphere. We have the exact formula relating the length to the azimuthal angle

$$L_{\pm} = 2\pi - 2\beta \pm \Psi = \int_0^{|\phi|} d\varphi \left[\left(\frac{d\vartheta}{d\varphi}\right)^2 + \sin^2 \vartheta \right]^{1/2}, \quad (\text{B.7})$$

where $|\phi| = 2\pi - \gamma$ if $\beta < \frac{\pi}{2}$ or $|\phi| = \gamma$ if $\beta > \frac{\pi}{2}$. We can obtain the terms in the above integral using Eq. 2.31 and the harmonic approximation for κ given by

Eq. B.3:

$$\sin^2 \vartheta \approx 1 - \frac{A_1^2}{M_0^2} \sin^2 \left(\sqrt{1 - C_0} \varphi \right), \quad \text{and} \quad (\text{B.8})$$

$$\left(\frac{d\vartheta}{d\varphi} \right)^2 \approx \frac{1}{M_0^2} \left(\frac{d\kappa_1}{d\varphi} \right)^2 = \frac{(1 - C_0) A_1^2}{M_0^2} \cos^2 \left(\sqrt{1 - C_0} \varphi \right). \quad (\text{B.9})$$

Thus, in the quadratic approximation,

$$2\pi - 2\beta \pm \Psi \approx |\phi| \left(1 - \frac{A_1^2}{4C_0} \right). \quad (\text{B.10})$$

Note that $|\phi| = L_0 + \mathcal{O}(\sqrt{-k})$. Equations B.6 and B.10 combine to the identity

$$-M_2 \text{sign } C_0 + C_2 = 2(1 - C_0)(\Gamma - 1), \quad (\text{B.11})$$

where $\Gamma = (2\pi - 2\beta \pm \Psi)/|\phi|$.

At the lowest non-trivial order, the last identity is all one need to satisfy the boundary conditions [122]. Thus we write the remaining boundary condition 2.40 as

$$\frac{C}{M} \approx \frac{C_0}{M_0} + \frac{M_0 C_2 - C_0 M_2}{M_0^2} = \text{sign}(C_0) \left[1 + \frac{C_2 - M_2 \text{sign}(C_0)}{C_0} \right]. \quad (\text{B.12})$$

Using Eq. B.11 this becomes

$$\frac{C}{M} \approx \text{sign}(C_0) \left[1 + \frac{2(1 - C_0)}{C_0} (\Gamma - 1) \right]. \quad (\text{B.13})$$

In order to approximate the right-hand side, we need an expression for the angle γ . When Ψ is small, $\alpha \approx \pi/2$, and it is possible to put the approximation

$$\cos \gamma \approx \cos(2\beta) + 2 \left(\frac{\pi}{2} - \alpha \right)^2 \sin^2 \beta, \quad (\text{B.14})$$

B. HARMONIC APPROXIMATION FOR DIPOLE DEFECTS

or, equivalently,

$$\gamma = 2\beta - \Delta\gamma, \quad \text{if } \beta < \frac{\pi}{2} \quad \text{and} \quad (\text{B.15})$$

$$\gamma = 2\pi - 2\beta + \Delta\gamma, \quad \text{if } \beta > \frac{\pi}{2}, \quad (\text{B.16})$$

where we have defined $\Delta\gamma = \left(\frac{\pi}{2} - \alpha\right)^2 \tan \beta$.

For both $\beta < \frac{\pi}{2}$ and $\beta > \frac{\pi}{2}$, we thus have $|\phi| = 2\pi - 2\beta + \Delta\gamma$ and,

$$\Gamma - 1 \approx \frac{1}{2\pi - 2\beta} [\pm\Psi - \Delta\gamma]. \quad (\text{B.17})$$

Furthermore, we use Eq. B.4 to obtain

$$-\frac{C_0}{1 - C_0} = 1 - \left(\frac{|\phi|}{n\pi}\right)^2 \approx 1 - \left(\frac{2\pi - 2\beta}{n\pi}\right)^2 - 2\Delta\gamma \left(\frac{2\pi - 2\beta}{n^2\pi^2}\right); \quad (\text{B.18})$$

where the correction in γ is irrelevant at this order. Thus we obtain

$$\frac{2(1 - C_0)}{C_0}(\Gamma - 1) \approx \frac{2}{2\pi - 2\beta} \left[1 - \left(\frac{2\pi - 2\beta}{n\pi}\right)^2\right]^{-1} (\mp\Psi + \Delta\gamma). \quad (\text{B.19})$$

Having approximately $\alpha \approx \frac{\pi}{2}$, the trigonometric term on the right-hand side of Eq. 2.40 can be written as

$$\frac{\sin \alpha \cos \beta}{\sqrt{1 - \sin^2 \alpha \sin^2 \beta}} \approx \text{sign} \left(\frac{\pi}{2} - \beta\right) \left[1 - \frac{1}{2} \left(\frac{\pi}{2} - \alpha\right)^2 \sec^2 \beta\right]. \quad (\text{B.20})$$

We have to be careful about the signs of the right-hand and the left-hand side of the equation corresponding to the different cases in order to correctly express the boundary condition 2.40.

In the harmonic approximation L_0 has to be smaller than 2π . From Eq. B.4, we obtain that $C_{+,0} \leq -\frac{5}{4}$ is always negative and $M_0 = -C_{+,0}$ for the surplus part having $n_+ = 3$. The (nonlinear) C_+ is thus also negative for small Ψ ; one

only finds two types of solution (see Tab. 2.1): $(\alpha < \frac{\pi}{2}, \beta_+ < \frac{\pi}{2}, L_0 = 2\pi - \gamma)$ and $(\alpha > \frac{\pi}{2}, \beta_+ > \frac{\pi}{2}, L_0 = \gamma)$.

As a result, the boundary condition 2.40 becomes

$$\frac{2}{2\pi - 2\beta} \left[1 - \left(\frac{2\pi - 2\beta}{3\pi} \right)^2 \right]^{-1} \left(-\Psi + \left(\frac{\pi}{2} - \alpha \right)^2 \tan \beta \right) = -\frac{1}{2} \left(\frac{\pi}{2} - \alpha \right)^2 \sec^2 \beta, \quad (\text{B.21})$$

for all $\beta_+ \in \{0, \pi\}$.

For the deficit part the number of extrema is $n_- = 1$. Since for $\beta_- < \frac{\pi}{2}$ we always have $L_0 = 2\pi - \gamma > \pi$, we find that $C_{-,0}$ is positive. For $\beta_- > \frac{\pi}{2}$ we always have $L_0 = \gamma < \pi$ and therefore $C_{-,0} < 0$. Both types of solution with $\alpha < \frac{\pi}{2}$ are thus possible (see Tab. 2.1 for the sign of C_-). However, $\alpha > \frac{\pi}{2}$ is not allowed.

For $\beta_- \in \{0, \pi\}$, the boundary condition 2.40 reads:

$$\frac{2}{2\pi - 2\beta} \left[1 - \left(\frac{2\pi - 2\beta}{\pi} \right)^2 \right]^{-1} \left(\Psi + \left(\frac{\pi}{2} - \alpha \right)^2 \tan \beta \right) = -\frac{1}{2} \left(\frac{\pi}{2} - \alpha \right)^2 \sec^2 \beta. \quad (\text{B.22})$$

We write equations B.21 and B.22 in the concise form:

$$\Psi = \frac{1}{2} f_{\pm}(\beta) \left(\frac{\pi}{2} - \alpha \right)^2, \quad (\text{B.23})$$

where

$$\begin{aligned} f_{\pm}(\beta) &= \pm \frac{1}{2} (2\pi - 2\beta) \sec^2 \beta \left[1 - \left(\frac{2\pi - 2\beta}{n_{\pm}\pi} \right)^2 \right] \pm 2 \tan \beta \\ &= \pm \frac{1}{2} \sec^2 \beta \left[(2\pi - 2\beta) \left[1 - \left(\frac{2\pi - 2\beta}{n_{\pm}\pi} \right)^2 \right] + 2 \sin 2\beta \right]. \end{aligned} \quad (\text{B.24})$$

To have $\Psi \neq 0$, Eq. B.23 implies that $\alpha = \frac{\pi}{2}$ can only be achieved for values of β_{\pm} at which f_{\pm} diverges. For the surplus part, the function f_+ diverges at $\beta_+ = \frac{\pi}{2}$. However f_- of the deficit part is a monotonically decreasing function of β_- with no divergences. Therefore, for any Ψ we have $\beta_+|_{\alpha=\frac{\pi}{2}} = \frac{\pi}{2}$ while $\beta_-|_{\alpha=\frac{\pi}{2}} = 0$ holds only if $\Psi \rightarrow 0$. This also observed in the nonlinear regime. Furthermore

B. HARMONIC APPROXIMATION FOR DIPOLE DEFECTS

we see that the numerical results of the nonlinear equations matches the results of the harmonic approximation in the limit of vanishing Ψ .

The angle α has to be the same for both the surplus and deficit parts. For fixed $\Psi/2\pi \ll 1$, together with Eq. B.23, this condition implies that $f_+(\beta_+) = f_-(\beta_-)$ in the harmonic approximation.

Appendix C

Numerical calculations for the axisymmetric invaginations

For moderate surface growth, the invaginations of the inner membrane are axisymmetric. By making use of a specific parametrization, the shape equation for the axisymmetric surfaces reduces to an ordinary differential equation. One can find the corresponding shapes using well established techniques which have previously been developed to study vesicle shapes [45, 123, 124, 125, 126], vesicle adhesion [127, 128], membrane-bound colloids [129, 130, 131, 132, 133], and membrane pulling and pushing [134, 135, 136, 137, 138, 139].

In Fig. C.1, we show the profile of an axisymmetric solution. The membrane is composed of two parts: a spherical cap of unit size in contact with the container, and an upper section detached from the container to form an invagination. The profile of the spherical cap follows exactly that of container, so it can be expressed by the height function of the unit sphere $z(x) = \pm\sqrt{1-x^2}$. The mean curvature of this part is always constant and equals $H = -1$. It is convenient to describe the free part by the angle-arc length parametrization, $\psi(s)$, where ψ is the angle between the tangent vector and the horizontal x axis and s is the arc length. The mean curvature is given by $H = -\frac{1}{2}(\dot{\psi} + \frac{\sin \psi}{x})$, in this parametrization.

We scale the mechanical energy 3.3 of the free part $\tilde{E} := E/(\pi\kappa)$, and express

C. NUMERICAL CALCULATIONS

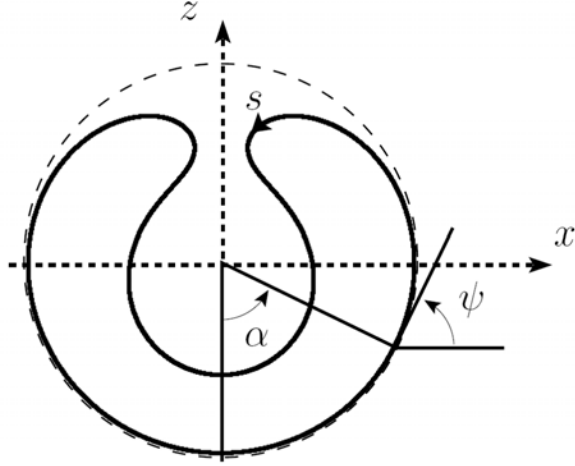


Figure C.1: Definition of variables. The confined axisymmetric membrane vesicle consists of a spherical cap in contact with the container and an upper free section. For the shown profile $\tilde{\sigma} = -0.25$ and $\tilde{P} = 0.7$, and $\alpha = 1.15$, which corresponds to a scaled area $a = 1.2$, a scaled enclosed volume $v = 0.8$, and a spontaneous curvature $C_0 = 0$.

it as an integral over the arc length, $\tilde{E} = \int_{\underline{s}}^{\bar{s}} ds \tilde{L}$ with

$$\tilde{L} = x \left(\dot{\psi} + \frac{\sin \psi}{x} + C_0 \right)^2 + 2\tilde{\sigma}x + \lambda_x (\dot{x} - \cos \psi) + \tilde{P}x^2 \sin \psi, \quad (\text{C.1})$$

where

$$\tilde{\sigma} = \frac{\sigma}{\kappa} \quad \text{and} \quad \tilde{P} = \frac{P}{\kappa} \quad (\text{C.2})$$

are the scaled tension and pressure, respectively. The Lagrange multiplier function λ_x fixes the geometrical constraint that $\dot{x} = \cos \psi$ everywhere along the profile. The conjugate momenta are

$$p_\psi = \frac{\partial \tilde{L}}{\partial \dot{\psi}} = 2x \left(\dot{\psi} + \frac{\sin \psi}{x} + C_0 \right) \quad \text{and} \quad p_x = \frac{\partial \tilde{L}}{\partial \dot{x}} = \lambda_x. \quad (\text{C.3})$$

We transform the scaled Lagrangian to the scaled Hamiltonian:

$$\begin{aligned}\tilde{H} &= \dot{\psi}p_\psi + \dot{x}p_x - \tilde{L} \\ &= \frac{p_\psi^2}{4x} + p_\psi \left(-\frac{\sin \psi}{x} - C_0 \right) - 2\tilde{\sigma}x + p_x \cos \psi - \tilde{P}x^2 \sin \psi ,\end{aligned}\quad (\text{C.4})$$

from which we obtain the Hamilton equations:

$$\dot{\psi} = \frac{\partial \tilde{H}}{\partial p_\psi} = \frac{p_\psi}{2x} - \frac{\sin \psi}{x} - C_0 ,\quad (\text{C.5})$$

$$\dot{x} = \frac{\partial \tilde{H}}{\partial p_x} = \cos \psi ,\quad (\text{C.6})$$

$$\dot{p}_\psi = -\frac{\partial \tilde{H}}{\partial \psi} = \left(\frac{p_\psi}{x} + \tilde{P}x^2 \right) \cos \psi + p_x \sin \psi ,\quad (\text{C.7})$$

$$\dot{p}_x = -\frac{\partial \tilde{H}}{\partial x} = \frac{p_\psi}{x} \left(\frac{p_\psi}{4x} - \frac{\sin \psi}{x} \right) + 2\tilde{\sigma} + 2\tilde{P}x \sin \psi .\quad (\text{C.8})$$

The shapes of the free membrane that are extrema of the energy can be found by integrating these equations with the appropriate boundary conditions. We must ensure that the membrane does not have any kinks at the start and the end points of the integration. Therefore, at the contact point $s = \underline{s}$ where the membrane takes off from the container, ψ should equal the angle α (see again Fig. C.1). Similarly, when the membrane reaches the z axis, $s = \bar{s}$, and the profile should be horizontal due to the symmetry. Hence, we obtain two conditions:

$$\psi(\underline{s}) = \alpha, \quad \psi(\bar{s}) = \pi .\quad (\text{C.9})$$

The energy balance at the contact points requires the contact curvature condition [127, 140]:

$$\dot{\psi}(\underline{s}) = 1 .\quad (\text{C.10})$$

The last condition on the Hamiltonian is due to the fact that we do not fix the total arc length $\bar{s} - \underline{s}$:

$$\tilde{H} = 0 .\quad (\text{C.11})$$

C. NUMERICAL CALCULATIONS

We solved the Hamilton equations using a standard shooting procedure [141]: for a fixed $\tilde{\sigma}$, \tilde{P} , and a trial angle α , we integrated the equations with the fourth-order Runge-Kutta method. The values of ψ , x , p_ψ , and p_x can be calculated at the starting point of the integration $s = \underline{s}$ with the help of the boundary conditions provided that the value of $\alpha \in \{0, \pi\}$ is given. We stop the integration as soon as the vertical axis is reached. Every α which results in $\psi(\bar{s}) = \pi$ returns a valid profile for the free part. Combining it with the spherical cap at the bottom provides us the profile of a closed axisymmetric membrane in a spherical cavity.

Note that in this method, we fix the Lagrange multipliers $\tilde{\sigma}$, \tilde{P} , and does not explicitly specify the values of the membrane area and enclosed volume. The shape we found are implicitly related to the area and volume. Once the profile is found, one can integrate $\dot{A} = 2\pi x$ and $\dot{V} = \pi x^2 \sin \psi$ from \underline{s} to \bar{s} to get the area and volume of the free part, respectively. The area of the membrane in contact with the container is given by $2\pi \int_0^{\underline{s}} ds \sin \psi = 2\pi(1 - \cos \alpha)$ and the volume of the corresponding lower spherical cap yields $\pi \int_0^{\underline{s}} ds x^2 \sin \psi = \frac{\pi}{3}(2 - 3 \cos \alpha + \cos^3 \alpha)$. Sweeping through the parameter space $(\tilde{\sigma}, \tilde{P})$ thus allows to find confined vesicles with variable area and volume.

Appendix D

Finite element simulations

We intend to study the equilibrium solutions of a closed membrane governed by the energy functional Eq. 3.5 augmented with container and self-contact constraints. Since the curvature integral in Eq. 3.5 is a quadratic functional of curvatures, it requires continuous second derivatives of the solution in order to remain bounded. In terms of the Finite Elements, this condition means the requirement of element trial functions that belong to the Sobolev space \mathcal{H}^2 , the space of square-integrable surface functions having square integrable derivatives through second-order. This condition can be roughly satisfied by surfaces which have C^1 continuity, *i.e.*, having continuous first derivatives. Only recently, Cirak *et al.* proposed an efficient Finite Element method fulfilling this C^1 continuity requirement based on Loop subdivision surfaces used extensively in the framework of Computer-aided design [142, 143]. Klug and coworkers extended the subdivision finite elements approach to the field of fluid membrane physics [57, 58]. In our implementation, we combined Klug *et al.*'s approach with the container constraint and the contact handling, both specific to our problem.

D. FINITE ELEMENT SIMULATIONS

D.1 Discretization

The surface is represented by a control mesh having F triangles and N nodes. Using the trial functions N^a , the position \mathbf{x} of a point on the surface is then interpolated by the weighted sum \mathbf{x}_h

$$\mathbf{x}_h(s^1, s^2) = \sum_{a=1}^N \mathbf{x}_a N^a(s^1, s^2), \quad (\text{D.1})$$

where \mathbf{x}_a is the position of node a . For N^a we employed the Loop subdivision trial functions (see, e.g., [142] for their precise form).

In contrast to the numerical shooting method, in the finite element simulations we enforce the volume and the surface area constraints using the penalty method, the mechanical energy taking the form of

$$E = \int_{\Omega} \frac{\kappa}{2} (2H - C_0)^2 \sqrt{a} ds^1 ds^2 + \frac{\mu_A}{2} (A - \bar{A})^2 + \frac{\mu_V}{2} (V - \bar{V})^2, \quad (\text{D.2})$$

where μ_A and μ_V are constants chosen large enough to approximatively fulfill the constraint on the prescribed target values. This approach offers improved convergence properties and easier implementation than Lagrangian multipliers.

In contrast to elastic shell theory, where a well-defined reference configuration of the material exists, the points of the lipid membrane surface can freely flow on the surface as long as the shape of the surface is not altered, a zero mode motion that corresponds to the in-plane flow of lipid molecules. Therefore, the solution of internal energy as formulated above could lead to arbitrary in-plane movements of mesh nodes resulting in severe mesh distortion. Such tangential distortions can be bypassed by two different techniques. The first one is based on a reformulation of the area constraint locally in the surface (*local area constraint method*). The second method enforces the area constraint globally as in Eq. D.2 (*global area constraint method*), but the mesh is stabilized by a regularization routine to improve mesh quality. We employed both methods to validate our results.

In the local area constraint method Eq. D.2 is recast into the equivalent for-

mulation

$$E = \int_{\Omega} \left[\frac{\kappa}{2} (2H - C_0)^2 + \frac{\mu_A}{2} (\sqrt{a} - \sqrt{\bar{a}})^2 \right] ds^1 ds^2 + \frac{\mu_V}{2} (V - \bar{V})^2, \quad (\text{D.3})$$

in which \sqrt{a} is the surface Jacobian such that $A = \int_{\Omega} \sqrt{a} ds^1 ds^2$. While physically identical, the area constraint here is enforced locally, *i.e.*, at the element level.

On the other hand, in the global area constraint method, we introduce an artificial spring potential on the edges of the mesh to penalize spurious tangential motion of nodes in an iterative process, such that the equilibrium solution is not affected [58].

At the start of a simulation, the reference length $\mathbf{l}^0 = l_1^0, \dots, l_M^0$ of all edges is calculated and stored. In each step of the computation, the deviation from the reference length is penalized with a linear spring force of the form

$$\mathbf{f}_a^{R1} = \sum_i k(l_i - l_i^0) \mathbf{n}_i, \quad (\text{D.4})$$

where the sum runs over all edges i of node a , l_i is the current edge length and \mathbf{n}_i is the unit vector along edge i . The reference lengths \mathbf{l}^0 are reset every 1000 iterations to the current edge lengths. The reset procedure is crucial to prevent the regularization forces to polymerize the surface by suppressing the fluid-like nature of the membrane. Furthermore, to reduce severe distortion of the elements of the mesh, we introduce a regularization force which favors equilaterality of the triangle. For a node a of such a distorted triangle, the corresponding force is calculated according to

$$\mathbf{f}_a^{R2} = \sum_i k(l_i - \bar{l}_i^0) \mathbf{n}_i, \quad (\text{D.5})$$

where the ‘‘equilateral reference length’’ \bar{l}_i^0 is given by $\bar{l}_i^0 = 2\sqrt{\frac{A}{\sqrt{3}}}$, *i.e.*, the edge length of an equilateral triangle with the same area as the distorted one.

For both area constraint methods, the finite element procedure proceeds in the same way: The energies Eq. D.2 or D.3 are expressed in a discrete form as a function of the nodal position coefficients \mathbf{x}_a . The variation of the energy with respect to the displacement of nodal position yields the corresponding nodal

D. FINITE ELEMENT SIMULATIONS

forces \mathbf{f}_a^M (M denotes the contribution from the membrane forces) :

$$\delta E = \frac{\partial E}{\partial \mathbf{x}_a} \delta \mathbf{x}_a = -\mathbf{f}_a^M \delta \mathbf{x}_a . \quad (\text{D.6})$$

In the so-called stress resultant formulation \mathbf{f}_a^M can be concisely written as

$$\mathbf{f}_a^M = \int_{\Omega} \left[\mathbf{n}^\alpha \cdot \frac{\partial \mathbf{a}_\alpha}{\partial \mathbf{x}_a} + \mathbf{m}^\alpha \cdot \left(\frac{\partial \mathbf{d}}{\partial \mathbf{x}_a} \right)_{,\alpha} + \hat{\mathbf{n}}^\alpha \cdot \frac{\partial \mathbf{a}_\alpha}{\partial \mathbf{x}_a} + \mathbf{f} N^\alpha \right] \sqrt{a} \, ds^1 ds^2 , \quad (\text{D.7})$$

where the stress resultant \mathbf{n}^α and the moment resultant \mathbf{m}^α measure the in- and out-of-plane forces due to bending, whereas $\hat{\mathbf{n}}^\alpha$ and \mathbf{f} account for the constraints.

They are given by

$$\mathbf{n}^\alpha = \kappa(2H - C_0) a^{\alpha\beta} \mathbf{d}_{,\beta} + \frac{\kappa}{2} (2H - C_0)^2 \mathbf{a}^\alpha , \quad (\text{D.8})$$

$$\mathbf{m}^\alpha = -\kappa(2H - C_0) \mathbf{a}^\alpha , \quad (\text{D.9})$$

$$\hat{\mathbf{n}}^\alpha = \mu_A \Delta A \mathbf{a}^\alpha + \mu_V \frac{V - \bar{V}}{3} [(\mathbf{x} \cdot \mathbf{d}) \mathbf{a}^\alpha - (\mathbf{x} \cdot \mathbf{a}^\alpha) \mathbf{d}] , \quad (\text{D.10})$$

$$\mathbf{f} = \mu_V \frac{V - \bar{V}}{3} \mathbf{d} . \quad (\text{D.11})$$

The coefficient ΔA depends on the type of the surface area constraint chosen; it is $\Delta A = \sqrt{a} - \sqrt{\bar{a}}$ in the case of the local area constraint method and $\Delta A = A - \bar{A}$ for the global area constraint method. In the latter case, the regularization forces $\mathbf{f}_a^{R1}, \mathbf{f}_a^{R2}$ as described above are added to the resulting force vector as well. Values of $\mu_A = 10^4$ and $\mu_V = 5 \cdot 10^4$ were used for the global constraint method, whereas the local constraint method had $\mu_A = 10^5$ and $\mu_V = 5 \cdot 10^4$.

The confinement of the membrane within a cavity is modeled by a quadratic force field switched on beyond the limits of the cavity. Once a node penetrates into the cavity field, its current position \mathbf{x}_a is used to calculate the penetration depth d_a , then a repulsive force proportional to the penetration depth is applied in the direction \mathbf{n} normal to the container surface:

$$\mathbf{f}_a^{C1} = k_1 d_a^2 \mathbf{n} , \quad (\text{D.12})$$

where a stiffness constant $k_1 = 1500$ was chosen.

To handle the self-intersection response of the membrane, we adopted the method developed by Volino and Magnat-Thalmann [144] based on the minimization of the intersection contour length. In other words, the algorithm calculates necessary forces to disentangle intersections *once they occurred*. This is in contrast with the classical contact handling methods where the contact forces are computed based on the distance between surface segments *before they penetrate*. As soon as some surface domains penetrate into each other the contour of intersection is detected. This information is then used to calculate the gradient \mathbf{G} , along which the displacement of a node a of a triangle involved in an intersection, minimizes the contour length (further details on the calculation of \mathbf{G} are provided in the appendix D.2). A contact force proportional to the gradient, $\mathbf{f}_a^{C_2} = k_2 \mathbf{G}$ is applied to node a . In our simulations, we chose a stiffness constant of $k_2 = 9$, which was sufficiently large to quickly resolve all intersections during a simulation within a few timesteps.

The force \mathbf{f}_a at node a is assembled by summing up all the terms in the system, *i.e.*, the Helfrich, constraints, container and contact forces. The equilibrium of the system is characterized by the balance of forces at each node:

$$\mathbf{f}_a = \mathbf{f}^M + \mathbf{f}_a^R + \mathbf{f}_a^{C_1} + \mathbf{f}_a^{C_2} = 0 , \quad (\text{D.13})$$

where $\mathbf{f}_a^R = \mathbf{f}_a^{R_1} + \mathbf{f}_a^{R_2}$ is only nonzero if the global area constraint method is used.

In contrast to Klug *et al.*, we do not employ a nonlinear gradient descent method to find equilibrium solutions. Instead, we integrate in time the nodal forces \mathbf{f}_a until a balance of forces is reached according to Newtons equation of motion:

$$\mathbf{M}\ddot{\mathbf{x}} = \mathbf{C}\dot{\mathbf{x}} + \mathbf{f}_a , \quad (\text{D.14})$$

where \mathbf{M} is the (diagonal) mass matrix, $\ddot{\mathbf{x}} = (\ddot{\mathbf{x}}_1, \dots, \ddot{\mathbf{x}}_N)$ is the generalized acceleration vector, and $\mathbf{C} = \mathbf{M} \cdot \text{diag}(c, \dots, c)$ is the mass-dependent viscous damping matrix. We chose c in the range of $c = [50, 200]$ depending on the amount of internal energy. Numerical integration in time was performed using a standard Newmark method, see, e.g., [56].

D. FINITE ELEMENT SIMULATIONS

Our simulations started from spherical meshes with $N = 2562$ nodes. For shapes with large surface growth, we repeatedly optimized the mesh during the simulation using the free REMESH software package [145]. The remeshing procedure redistributes a given number of nodes on the initial surface for improved accuracy and mesh quality. We employed up to three remeshing steps within one simulation, resulting in either $N = 3000$ or $N = 4000$ mesh nodes.

D.2 Self-avoidance

In our Finite Element simulations, the self-avoidance of the mesh is achieved in two steps. In the **detection** phase, we mark the pair of triangles that intersect each other. The second step consists of the **force calculation** required to entangle such triangles.

Detection of intersections

A naive intersection test of each triangle of the mesh with respect to all other triangles implies a complexity of the order $O(N^2)$. In order to remedy this inefficiency, we adopted a *Cell list* approach similar to the molecular dynamics simulations. Hence, our simulation box is divided into small cubical units called *Voxels*. According to this crystallized view of the simulation box, we draw a *Bounding box* around each triangle. A triangle is defined to be in a voxel, if the bounding box of the triangle overlaps with the voxel. In principle, one voxel can contain more than one triangle and one triangle can belong to more than one voxel. An iteration over the triangles and a simple rectangular overlap test establishes the list of triangles each voxel contains and the list of voxels each triangle belongs. In order to ensure efficient detection, these lists are reconstructed every 50 iterations.

At each iteration, the bounding boxes of triangles are updated and compared against the bounding boxes of the triangles which are in the same voxels. If there is an overlap, we test the intersection of the two triangles using the algorithm of Möller [146].

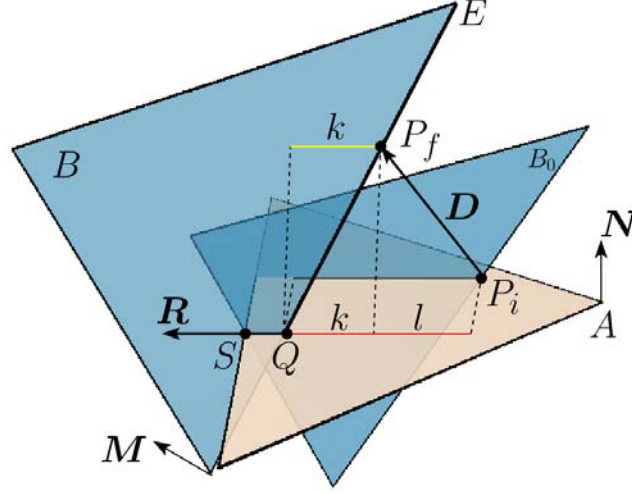


Figure D.1: The triangle B is displaced by a vector \mathbf{D} with respect to the triangle A . The intersection point between the edge E and the triangle A moves from point P_f to point Q over the polygon A .

Calculation of the contour gradient \mathbf{G}

After the detection phase, we have the complete list of pairs of triangles that intersect each other. Whenever such an intersection occurs, at least one edge the triangle B_0 intersects the triangle A as depicted in Fig. D.1. Let us assume that we displace the intersecting edge E by a small displacement vector \mathbf{D} . Hence the triangle B_0 moves and in its new configuration is denoted by B .

In the new configuration, the triangles A and B have the common segment \overline{QS} . We assign a vector \mathbf{R} to this segment \overline{SQ} . We compute \mathbf{R} through the normalized cross product of the surface normals \mathbf{N} , \mathbf{M} of the triangles A and B respectively. Explicitly given, this is

$$\mathbf{R} \sim \frac{\mathbf{N} \times \mathbf{M}}{|\mathbf{N} \times \mathbf{M}|}. \quad (\text{D.15})$$

The direction of the vector \mathbf{R} is adjusted to be towards the inside of the triangle B .

The point of the intersection of the edge E with the triangle A , moves from the position \mathbf{P}_i to the position \mathbf{P}_f after the displacement. By construction, we

D. FINITE ELEMENT SIMULATIONS

have the vector equality $\overrightarrow{P_i Q} = \mathbf{D} + \overrightarrow{P_f Q}$. Since \mathbf{N} is perpendicular to $\overrightarrow{P_i Q}$, this can also be written as:

$$\mathbf{N} \cdot \overrightarrow{P_f Q} = -\mathbf{N} \cdot \mathbf{D} . \quad (\text{D.16})$$

Using the fact that the vector associated to the displaced edge, *i.e.*, \mathbf{E} , is collinear with the vector $\overrightarrow{P_f Q}$, we write

$$(\mathbf{N} \cdot \mathbf{E}) \overrightarrow{P_f Q} = (\mathbf{N} \cdot \overrightarrow{P_f Q}) \mathbf{E} . \quad (\text{D.17})$$

Combining the equations D.16 and D.17, we get the relation

$$(\mathbf{N} \cdot \mathbf{E}) \overrightarrow{P_f Q} = -(\mathbf{N} \cdot \mathbf{D}) \mathbf{E} . \quad (\text{D.18})$$

On the triangle A , the intersection point slides from point P_i to the point Q . Hence the reduction in the intersection segment is given by the vector $\mathbf{l} + \mathbf{k}$ (see the red curve in Fig. D.1). The norm of this vector amounts to

$$\begin{aligned} k + l &= \overrightarrow{P_i Q} \cdot \mathbf{R} \\ &= \mathbf{D} \cdot \mathbf{R} + \overrightarrow{P_f Q} \cdot \mathbf{R} \\ &= \mathbf{D} \cdot \mathbf{R} - \frac{\mathbf{N} \cdot \mathbf{D}}{\mathbf{N} \cdot \mathbf{E}} \mathbf{E} \cdot \mathbf{R} . \end{aligned} \quad (\text{D.19})$$

Meanwhile, on the triangle B , the intersection point moves from point P_f to the point Q . In this case, the intersection segment is shortened by the vector \mathbf{k} (see the yellow curve in Fig. D.1). Its norm equals

$$k = \overrightarrow{P_f Q} \cdot \mathbf{R} = -\frac{\mathbf{N} \cdot \mathbf{D}}{\mathbf{N} \cdot \mathbf{E}} \mathbf{E} \cdot \mathbf{R} . \quad (\text{D.20})$$

Hence the overall contour reduction can be expressed as the dot product of the displacement \mathbf{D} with a vector \mathbf{G} :

$$l + 2k = \mathbf{G} \cdot \mathbf{D} , \quad (\text{D.21})$$

where

$$\mathbf{G} = \mathbf{R} - 2 \frac{\mathbf{E} \cdot \mathbf{R}}{\mathbf{E} \cdot \mathbf{N}} \mathbf{N}. \quad (\text{D.22})$$

In order to maximize the total reduction of the contour length, we should calculate the variation of $l + 2k$ with respect to \mathbf{D} , which is indeed the gradient vector \mathbf{G} . Hence we should apply a force to the nodes of the edge E in the direction of \mathbf{G} to minimize efficiently the intersection segment.

D. FINITE ELEMENT SIMULATIONS

Appendix E

Brownian dynamics simulations

Each vertex of the lattice is treated as a bead subject to the equation of motion:

$$\dot{\mathbf{r}} = \frac{D}{k_B T} \mathbf{f} + \sqrt{D} \boldsymbol{\nu}, \quad (\text{E.1})$$

where D is the diffusion constant, $\boldsymbol{\nu}$ is the Gaussian white noise, and \mathbf{f} is the sum of the (elastic) forces acting on the bead.

The conventional Brownian dynamics algorithm reads

$$\mathbf{r}(t + \Delta t) = \mathbf{r}(t) + \frac{D}{k_B T} \mathbf{f} \Delta t + \boldsymbol{\Gamma}, \quad (\text{E.2})$$

where the noise $\boldsymbol{\Gamma}$ is a noise sampled with zero mean and a variance $\langle \Gamma_i^2 \rangle = 2D\Delta t$, for each component i .

E.1 Stretching forces

For a bond $\mathbf{d} = \mathbf{p}^2 - \mathbf{p}^1$, connecting two beads \mathbf{p}^1 and \mathbf{p}^2 the stretching potential is given by

$$E_s = \frac{1}{2} \mu_s (|\mathbf{d}| - d_i)^2,$$

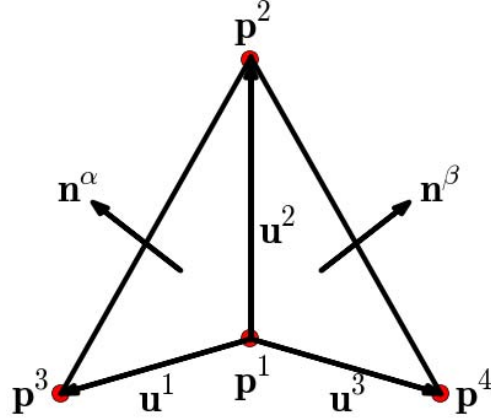


Figure E.1: A hinge formed by 4 points

where d_i denotes the preferred bond length. The corresponding forces on beads are given by

$$\mathbf{f}_1 = -\mathbf{f}_2 = -\frac{\partial E_s}{\partial \mathbf{p}_1} = \mu_s(|\mathbf{d}| - d_i) \frac{\mathbf{d}}{|\mathbf{d}|}. \quad (\text{E.3})$$

E.2 Bending forces

In order to write the bending energy of a bond \mathbf{u}^2 between the particles \mathbf{p}^1 and \mathbf{p}^2 we define two triangles with the help of two neighboring particles \mathbf{p}^3 and \mathbf{p}^4 (see the construction given in Fig. E.1). We define the bonds between the particles

$$\begin{aligned} \mathbf{u}^1 &= \mathbf{p}^3 - \mathbf{p}^1, \\ \mathbf{u}^2 &= \mathbf{p}^2 - \mathbf{p}^1, \\ \mathbf{u}^3 &= \mathbf{p}^4 - \mathbf{p}^1, \end{aligned} \quad (\text{E.4})$$

and the normals of two triangles formed by these bonds:

$$\mathbf{n}^\alpha = \frac{\mathbf{u}^1 \times \mathbf{u}^2}{|\mathbf{u}^1 \times \mathbf{u}^2|}, \quad \text{and} \quad \mathbf{n}^\beta = \frac{\mathbf{u}^2 \times \mathbf{u}^3}{|\mathbf{u}^2 \times \mathbf{u}^3|}. \quad (\text{E.5})$$

We project the cross product of triangle normals on the shared edge in order

to be able to control the sign of the angle. Hence the energy is expressed as:

$$E = \frac{1}{2}\kappa \left((\mathbf{n}^\alpha \times \mathbf{n}^\beta) \cdot \frac{\mathbf{u}^2}{|\mathbf{u}^2|} - \sin \gamma \right)^2. \quad (\text{E.6})$$

The variation of the energy with respect to positions of four particles can be written as

$$\begin{aligned} \frac{\partial E}{\partial \mathbf{p}^1} &= \frac{\partial \mathbf{u}^1}{\partial \mathbf{p}^1} \frac{\partial \mathbf{n}^\alpha}{\partial \mathbf{u}^1} \frac{\partial E}{\partial \mathbf{n}^\alpha} + \frac{\partial \mathbf{u}^2}{\partial \mathbf{p}^1} \frac{\partial \mathbf{n}^\alpha}{\partial \mathbf{u}^2} \frac{\partial E}{\partial \mathbf{n}^\alpha} + \frac{\partial \mathbf{u}^2}{\partial \mathbf{p}^1} \frac{\partial \mathbf{n}^\beta}{\partial \mathbf{u}^2} \frac{\partial E}{\partial \mathbf{n}^\beta} + \frac{\partial \mathbf{u}^3}{\partial \mathbf{p}^1} \frac{\partial \mathbf{n}^\beta}{\partial \mathbf{u}^3} \frac{\partial E}{\partial \mathbf{n}^\beta} + \frac{\partial \mathbf{u}^2}{\partial \mathbf{p}^1} \frac{\partial E}{\partial \mathbf{u}^2}, \\ \frac{\partial E}{\partial \mathbf{p}^2} &= \frac{\partial \mathbf{u}^2}{\partial \mathbf{p}^2} \frac{\partial \mathbf{n}^\alpha}{\partial \mathbf{u}^2} \frac{\partial E}{\partial \mathbf{n}^\alpha} + \frac{\partial \mathbf{u}^2}{\partial \mathbf{p}^2} \frac{\partial \mathbf{n}^\beta}{\partial \mathbf{u}^2} \frac{\partial E}{\partial \mathbf{n}^\beta} + \frac{\partial \mathbf{u}^2}{\partial \mathbf{p}^2} \frac{\partial E}{\partial \mathbf{u}^2}, \\ \frac{\partial E}{\partial \mathbf{p}^3} &= \frac{\partial \mathbf{u}^1}{\partial \mathbf{p}^3} \frac{\partial \mathbf{n}^\alpha}{\partial \mathbf{u}^1} \frac{\partial E}{\partial \mathbf{n}^\alpha}, \\ \frac{\partial E}{\partial \mathbf{p}^4} &= \frac{\partial \mathbf{u}^3}{\partial \mathbf{p}^4} \frac{\partial \mathbf{n}^\beta}{\partial \mathbf{u}^3} \frac{\partial E}{\partial \mathbf{n}^\beta}. \end{aligned} \quad (\text{E.7})$$

So, we basically need three types of partial derivatives.

1. type $\frac{\partial \mathbf{u}^i}{\partial \mathbf{p}^j}$

This one is trivial, the result is either unit matrix or its opposite:

$$\begin{aligned} \frac{\partial \mathbf{u}^1}{\partial \mathbf{p}^2} &= \frac{\partial \mathbf{u}^2}{\partial \mathbf{p}^3} = \frac{\partial \mathbf{u}^3}{\partial \mathbf{p}^4} = \mathbf{I}, \\ \frac{\partial \mathbf{u}^1}{\partial \mathbf{p}^1} &= \frac{\partial \mathbf{u}^2}{\partial \mathbf{p}^1} = \frac{\partial \mathbf{u}^3}{\partial \mathbf{p}^1} = -\mathbf{I}. \end{aligned} \quad (\text{E.8})$$

2. type $\frac{\partial \mathbf{n}^i}{\partial \mathbf{u}^j}$

The derivatives of the normals \mathbf{n} with respect to the bond vectors \mathbf{u} returns

$$\begin{aligned} \frac{\partial n_i^\alpha}{\partial u_p^1} &= \frac{1}{|\mathbf{u}^1 \times \mathbf{u}^2|} u_k^2 (\epsilon_{ipk} - n_i^\alpha n_s^\alpha \epsilon_{spk}), \\ \frac{\partial n_i^\alpha}{\partial u_p^2} &= \frac{1}{|\mathbf{u}^1 \times \mathbf{u}^2|} u_j^1 (\epsilon_{ijp} - n_i^\alpha n_s^\alpha \epsilon_{sjp}), \end{aligned} \quad (\text{E.9})$$

E. BROWNIAN DYNAMICS SIMULATIONS

$$\begin{aligned}\frac{\partial n_i^\beta}{\partial u_p^2} &= \frac{1}{|\mathbf{u}^2 \times \mathbf{u}^3|} u_k^3 \left(\epsilon_{ipk} - n_i^\beta n_s^\beta \epsilon_{spk} \right), \\ \frac{\partial n_i^\beta}{\partial u_p^3} &= \frac{1}{|\mathbf{u}^2 \times \mathbf{u}^3|} u_j^2 \left(\epsilon_{ijp} - n_i^\beta n_s^\beta \epsilon_{sjp} \right).\end{aligned}$$

3. type $\frac{\partial E}{\partial \mathbf{n}^j}$

Finally, we write the partial derivatives of E :

$$\begin{aligned}\frac{\partial E}{\partial \mathbf{n}^\alpha} &= \kappa \left((\mathbf{n}^\alpha \times \mathbf{n}^\beta) \cdot \frac{\mathbf{u}^2}{|\mathbf{u}^2|} - \sin \gamma \right) \left(\mathbf{n}^\beta \times \frac{\mathbf{u}^2}{|\mathbf{u}^2|} \right), \\ \frac{\partial E}{\partial \mathbf{n}^\beta} &= \kappa \left((\mathbf{n}^\alpha \times \mathbf{n}^\beta) \cdot \frac{\mathbf{u}^2}{|\mathbf{u}^2|} - \sin \gamma \right) \left(\frac{\mathbf{u}^2}{|\mathbf{u}^2|} \times \mathbf{n}^\alpha \right), \\ \frac{\partial E}{\partial \mathbf{u}^2} &= \frac{\kappa}{|\mathbf{u}^2|} \left((\mathbf{n}^\alpha \times \mathbf{n}^\beta) \cdot \frac{\mathbf{u}^2}{|\mathbf{u}^2|} - \sin \gamma \right) \left((\mathbf{n}^\alpha \times \mathbf{n}^\beta) - \left((\mathbf{n}^\alpha \times \mathbf{n}^\beta) \cdot \frac{\mathbf{u}^2}{|\mathbf{u}^2|} \right) \frac{\mathbf{u}^2}{|\mathbf{u}^2|} \right).\end{aligned}\tag{E.10}$$

E.3 Parameters

The value of the stretching rigidity μ_s is specified in the main text. For the diagonal bonds, we applied $\mu_{s4} = 1000 k_B T / b^2$ which was sufficient to conserve the rectangular nature of subunits. Here b denotes the unit length in the system. A bending rigidity $\mu_{b4} = 500 k_B T \times b$ was chosen for diagonal bonds. The bending rigidity of bonds B_3 was set to $\mu_{b3} = 1500 k_B T \times b$.

The anharmonic bending potential E_{anharm} of B_2 given in Eq. 4.11 has $\Delta G = 200 k_B T$, $\Delta E_b = 1 k_B T$, and $s_2 = -0.588$. So, a free dimer would prefer to be in curved state with an angle 36° . We use $E_{\text{anharm}}(s_2) = -\Delta G$ and $E'_{\text{anharm}}(s_2) = 0$, to write B and C as functions of A :

$$\begin{aligned}B &= \frac{2\Delta G}{(s_2)^3} - 2As_2, \\ C &= A(s_2)^2 - \frac{3\Delta G}{(s_2)^2}.\end{aligned}\tag{E.11}$$

We look for a solution having a maximum \tilde{s} between $s = 0$ and $s = s_2$, satisfying $E_{\text{anharm}}(\tilde{s}) = \Delta E_b$. Combining this constraint with Eq. E.11, we obtain the

relation

$$\frac{(A(s_2)^4 - 3\Delta G)^3(A(s_2)^4 + \Delta G)}{16A^3(s_2)^{12}} = \Delta E_b. \quad (\text{E.12})$$

By solving this equation for given values of ΔG , ΔE_b , and s_2 , we obtain A , and also B and C through Eq. [E.11](#).

If we were to approximate this double well potential by a harmonic one around s_2 , the chosen parameters would correspond to an effective bending rigidity of value $2000 k_B T \times b$, a value slightly larger than that of μ_{b3} . In the Brownian dynamics simulations, we set the Boltzmann constant k_B and the unit of temperature T to one. The diffusion coefficient and the integration step were respectively set to $D = 0.001 d^2/\tau$ and $\delta t = 0.01 \tau$, where τ denotes the unit of time in simulations.

E. BROWNIAN DYNAMICS SIMULATIONS

References

- [1] S. F. Gilbert. *Developmental Biology*. 6th edn. Sinauer Associates, Sunderland (MA), 2000. [1](#)
- [2] J. B. Reece et al. *Campbell Biology*. 9th edn. Pearson, 2010. [1](#)
- [3] D. R. Carter, M. C. H. Van der Meulen, and G. S. Beaupré. Mechanical factors in bone growth and development. *Bone*, 18:S5 – S10, 1996. [1](#)
- [4] N. D. Epstein and J. S. Davis. Sensing stretch is fundamental. *Cell*, 112(2):147 – 150, 2003. [1](#)
- [5] O. Hamant and J. Traas. The mechanics behind plant development. *New Phytologist*, 185(2):369–385, 2010. [2](#)
- [6] H. Mohrbach, A. Johner, and I. M. Kulić. Cooperative lattice dynamics and anomalous fluctuations of microtubules. *European Biophysics Journal*, 41:217–239, 2012. [3](#), [65](#), [69](#), [70](#), [71](#), [86](#)
- [7] E. Couturier, S. Courrech du Pont, and S. Douady. A Global Regulation Inducing the Shape of Growing Folded Leaves. *PLOS ONE*, 4(11):e7968, 2009. [5](#)
- [8] M. Kücken and A. C. Newell. A model for fingerprint formation. *EPL (Europhysics Letters)*, 68(1):141, 2004. [5](#)
- [9] E. K. Rodriguez, A. Hoger, and A. D. McCulloch. Stress-dependent finite growth in soft elastic tissues. *Journal of Biomechanics*, 27(4):455 – 467, 1994. [5](#)

REFERENCES

- [10] A. Lobkovsky et al. Scaling properties of stretching ridges in a crumpled elastic sheet. *Science*, 270(5241):1482–1485, 1995. [5](#)
- [11] M. Ben Amar and Y. Pomeau. Crumpled paper. *Proceedings of the Royal Society of London. Series A: Mathematical, Physical and Engineering Sciences*, 453(1959):729–755, 1997. [5](#), [26](#)
- [12] E. Cerda and L. Mahadevan. Conical surfaces and crescent singularities in crumpled sheets. *Phys. Rev. Lett.*, 80:2358–2361, 1998. [5](#)
- [13] E. Cerda and L. Mahadevan. Confined developable elastic surfaces: cylinders, cones and the elastica. *Proceedings of the Royal Society A: Mathematical, Physical and Engineering Science*, 461(2055):671–700, 2005. [5](#)
- [14] M. M. Müller, M. Ben Amar, and J. Guven. Conical defects in growing sheets. *Phys. Rev. Lett.*, 101:156104, 2008. [6](#), [12](#), [14](#)
- [15] N. Stoop et al. Self-contact and instabilities in the anisotropic growth of elastic membranes. *Phys. Rev. Lett.*, 105(6):068101, 2010. [6](#), [14](#), [23](#)
- [16] J. Guven, M. M. Müller, and P. Vázquez-Montejo. Conical instabilities on paper. *Journal of Physics A: Mathematical and Theoretical*, 45(1):015203, 2012. [6](#), [14](#), [37](#)
- [17] K. A. Serikawa and D. F. Mandoli. An analysis of morphogenesis of the reproductive whorl of *Acetabularia acetabulum*. *Planta*, 207:96–104, 1998. [6](#), [7](#)
- [18] H. S. Seung and D. R. Nelson. Defects in flexible membranes with crystalline order. *Phys. Rev. A*, 38:1005–1018, 1988. [6](#), [26](#), [72](#)
- [19] M. J. Bowick and L. Giomi. Two-dimensional matter: order, curvature and defects. *Advances in Physics*, 58(5):449–563, 2009. [6](#)
- [20] J. Guven and M. M. Müller. How paper folds: bending with local constraints. *Journal of Physics A: Mathematical and Theoretical*, 41:055203, 2008. [9](#), [12](#)

REFERENCES

- [21] E. Kreyszig. *Differential Geometry*. Dover Books on Mathematics Series. Dover Publications, 1991. [11](#), [89](#)
- [22] J. Guven. Membrane geometry with auxiliary variables and quadratic constraints. *Journal of Physics A: Mathematical and General*, 37(28):L313, 2004. [12](#)
- [23] M. Abramowitz and I. A. Stegun. *Handbook of Mathematical Functions*. 9th edn. Dover, New York, 1970. [15](#), [18](#), [24](#)
- [24] M. Labouesse. How cell mechanics shapes embryos. In M. Ben Amar, A. Goriely, L. F. Cugliandolo, and M M Muller, editors, *New Trends in the Physics and Mechanics of Biological Systems*, page 339. Oxford University Press, 2011. [29](#)
- [25] B. Alberts et al. *Molecular Biology of the Cell*. Garland Publishing, New York, NY, fourth edition, 2002. [29](#), [32](#), [61](#)
- [26] M. Michalak, J. M. Robert Parker, and M. Opas. Ca^{2+} signaling and calcium binding chaperones of the endoplasmic reticulum. *Cell Calcium*, 32(5 - 6):269 – 278, 2002. [29](#)
- [27] J. D. Tucker et al. Membrane invaginations in *Rhodobacter sphaeroides* is initiated at curved regions of the cytoplasmic membrane, then forms both budded and fully detached spherical vesicles. *Molecular Microbiology*, 76(4):833–847, 2010. [29](#)
- [28] C. A. Mannella. Structure and dynamics of the mitochondrial inner membrane cristae. *BBA - Mol. Cell. Res.*, 1763:542–548, 2006. [29](#), [30](#)
- [29] M. Zick, R. Rabl, and A. S. Reichert. Cristae formation-linking ultrastructure and function of mitochondria. *BBA - Mol. Cell. Res.*, 1793:5–19, 2009. [30](#), [32](#), [35](#)
- [30] A. Goriely et al. Elastic growth models. In R. P. Mondaini and P. M. Pardalos, editors, *Mathematical Modelling of Biosystems*. Springer, New York, 2008. [30](#)

REFERENCES

- [31] G. E. Palade. The fine structure of mitochondria. *The Anatomical Record*, 114(3):427–451, 1952. [31](#)
- [32] F. S. Sjöstrand. The ultrastructure of cells as revealed by the electron microscope. *International Review of Cytology*, 5:455–533, 1956. [31](#)
- [33] D. S. Friend and G. E. Brassil. Osmium staining of endoplasmic reticulum and mitochondria in the rat adrenal cortex. *The Journal of Cell Biology*, 46(2):252–266, 1970. [31](#)
- [34] K. Blinzinger, N. B. Rewcastle, and H. Hager. Observations on prismatic-type mitochondria within astrocytes of the syrian hamster brain. *The Journal of Cell Biology*, 25(2):293–303, 1965. [31](#)
- [35] J. P. Revel, D. W. Fawcett, and C. W. Philpott. Observations on mitochondrial structure: Angular configurations of the cristae. *The Journal of Cell Biology*, 16(1):187–195, 1963. [31](#)
- [36] W. Th. Daems and E. Wisse. Shape and attachment of the cristae mitochondriales in mouse hepatic cell mitochondria. *Journal of Ultrastructure Research*, 16(1-2):123–140, 1966. [31](#)
- [37] C. Ulivieri. Cell death: Insights into the ultrastructure of mitochondria. *Tissue and Cell*, 42:339–347, 2010. [31](#)
- [38] D. Nicastro et al. Cryo-electron tomography of neurospora mitochondria. *Journal of Structural Biology*, 129(1):48 – 56, 2000. [32](#)
- [39] M. Schlame and M. Ren. The role of cardiolipin in the structural organization of mitochondrial membranes. *BBA - Biomembranes*, 1788:2080–2083, 2009. [32](#), [35](#)
- [40] G. K. Voeltz and W. A. Prinz. Sheets, ribbons and tubules - how organelles get their shape. *Nat. Rev. Mol. Cell Bio.*, 8:258–264, 2007. [32](#), [35](#), [58](#)
- [41] R. Rabl et al. Formation of cristae and crista junctions in mitochondria depends on antagonism between Fcjl1 and Su e/g. *J. Cell Biol.*, 185(6):1047–1063, 2009. [32](#), [35](#), [50](#), [58](#)

REFERENCES

- [42] M. D. Gorter and F. Grendel. On biomolecular layers of lipoids on the chromocytes of the blood. *J. Exp. Med.*, 41(4):439–443, 1925. [32](#)
- [43] S. J. Singer and G. L. Nicolson. The fluid mosaic model of the structure of cell membranes. *Science*, 175(4023):720–731, 1972. [32](#)
- [44] M. R. Villarreal. http://commons.wikimedia.org/wiki/File:Cell_membrane_detailed_diagram_en.svg. Accessed: September 30, 2012. [33](#)
- [45] U. Seifert. Configurations of fluid membranes and vesicles. *Adv. Phys.*, 46(1):13–137, 1997. [33](#), [36](#), [41](#), [46](#), [49](#), [97](#)
- [46] P. R. Cullis, D. B. Fenske, and M. J. Hope. Physical properties and functional roles of lipids in membranes. In D. E. Vance and J. E. Vance, editors, *Biochemistry of Lipids, Lipoproteins and Membranes*, volume 31 of *New Comprehensive Biochemistry*, pages 1 – 33. Elsevier, 1996. [33](#), [34](#)
- [47] H. T. McMahon and J. L. Gallop. Membrane curvature and mechanisms of dynamic cell membrane remodelling. *Nature*, 438:590–596, 2005. [35](#)
- [48] J. Zimmerberg and M. M. Kozlov. How proteins produce cellular membrane curvature. *Nat. Rev. Mol. Cell Biol.*, 7(1):9–19, 2006. [35](#)
- [49] K. M. Davies et al. Structure of the yeast F_1F_0 -ATP synthase dimer and its role in shaping the mitochondrial cristae. *PNAS*, 109(34):13602–13607, 2012. [35](#)
- [50] J. B. John et al. The mitochondrial inner membrane protein mitofilin controls cristae morphology. *Mol. Biol. Cell*, 16:1543, 2005. [35](#), [49](#), [50](#)
- [51] P. B. Canham. The minimum energy of bending as a possible explanation of the biconcave shape of the human red blood cell. *Journal of Theoretical Biology*, 26:61–81, 1970. [36](#)
- [52] W. Helfrich. Elastic properties of lipid bilayers: Theory and possible experiments. *Z. Naturforsch. C*, 28:693–703, 1973. [36](#)

REFERENCES

- [53] E. A. Evans. Bending resistance and chemically induced moments in membrane bilayers. *Biophys. J.*, 14:923–931, 1974. [36](#)
- [54] O. Zhong-can and W. Helfrich. Bending energy of vesicle membranes: General expressions for the first, second, and third variation of the shape energy and applications to spheres and cylinders. *Phys. Rev. A*, 39:5280–5288, 1989. [37](#)
- [55] R. Capovilla and J. Guven. Stresses in lipid membranes. *Journal of Physics A: Mathematical and General*, 35(30):6233, 2002. [37](#)
- [56] O. C. Zienkiewicz and R. L. Taylor. *The Finite Element Method for Solid and Structural Dynamics*. Oxford: Elsevier Butterworth-Heinemann, 6th edition, 2005. [38](#), [105](#)
- [57] F. Feng and W. S. Klug. Finite element modelling of lipid bilayer membranes. *J. Comp. Phys.*, 220:394–408, 2006. [39](#), [101](#)
- [58] L. Ma and W. S. Klug. Viscous regularization and r-adaptive remeshing for finite element analysis of lipid membrane mechanics. *J. Comp. Phys.*, 227:5816–5835, 2008. [39](#), [58](#), [101](#), [103](#)
- [59] T. Lewiner et al. Curvature and torsion estimators based on parametric curve fitting. *Computers & Graphics*, 29(5):641–655, 2005. [40](#)
- [60] P. Paumard et al. The ATP synthase is involved in generating mitochondrial cristae morphology. *The EMBO Journal*, 21(3):221–230, 2002. [50](#)
- [61] Y. Rao, C. Rükert, W. Saenger, and V. Haucke. The early steps of endocytosis: From cargo selection to membrane deformation. *European Journal of Cell Biology*, 91:226–233, 2012. [50](#)
- [62] S. M. Ferguson and P. De Camili. Dynamin, a membrane-remodelling GTPase. *Nat. Rev. Mol. Cell Biol.*, 13:75–88, 2012. [50](#)
- [63] J. H. Hurley and P. I. Hanson. Membrane budding and scission by the ESCRT machinery: it’s all in the neck. *Nat. Rev. Mol. Cell Biol.*, 11:556–566, 2010. [50](#)

-
- [64] R. Lipowsky. Budding of membranes induced by by intramembrane domains. *J. Phys. II France*, 2:1825, 1992. [52](#)
- [65] W. Wiese, W. Harbich, and W. Helfrich. Budding of lipid bilayer vesicles and flat membranes. *J. Phys. Condens. Matter*, 4:1647, 1992. [52](#)
- [66] W. T. Gózdź. The interface width of separated two-component lipid membranes. *The Journal of Physical Chemistry B*, 110(43):21981–21986, 2006. [52](#)
- [67] S. L. Das, J. T. Jenkins, and T. Baumgart. Neck geometry and shape transitions in vesicles with co-existing fluid phases: Role of Gaussian curvature stiffness vs. spontaneous curvature. *EPL (Europhysics Letters)*, 86(4):48003, 2009. [52](#)
- [68] V. Anesti and L. Scorrano. The relationship between mitochondrial shape and function and the cytoskeleton. *Biochimica et Biophysica Acta (BBA) - Bioenergetics*, 1757(5-6):692 – 699, 2006. [52](#)
- [69] D. Zwillinger. *CRC Standard Mathematical Tables and Formulae*. Boca Raton, FL: CRC Press, 32nd edn. edition, 2011. [54](#)
- [70] T. Lecuit and P.-F. Lenne. Cell surface mechanics and the control of cell shape, tissue patterns and morphogenesis. *Nature Reviews Molecular Cell Biology*, 8:633–644, 2007. [58](#)
- [71] C. M. Elliott and B. Stinner. Modeling and computation of two phase geometric biomembranes using surface finite elements. *Journal of Computational Physics*, 229(18):6585 – 6612, 2010. [58](#)
- [72] M. Rognes, M. Calderer, and C. Micek. Modelling of and mixed finite element methods for gels in biomedical applications. *SIAM Journal on Applied Mathematics*, 70(4):1305–1329, 2009. [58](#)
- [73] T. Klöppel and W. Wall. A novel two-layer, coupled finite element approach for modeling the nonlinear elastic and viscoelastic behavior of human erythrocytes. *Biomechanics and Modeling in Mechanobiology*, 10:445–459, 2011. [58](#)

REFERENCES

- [74] R. M. MacMeccan, J. R. Clausen, G. P. Neitzel, and C. K. Aidun. Simulating deformable particle suspensions using a coupled lattice-Boltzmann and finite-element method. *Journal of Fluid Mechanics*, 618:13–39, 2009. [58](#)
- [75] C. Eloy. Leonardo’s rule, self-similarity, and wind-induced stresses in trees. *Phys. Rev. Lett.*, 107:258101, 2011. [59](#)
- [76] S. Isnard and W. K. Silk. Moving with climbing plants from Charles Darwin’s time into the 21st century. *American Journal of Botany*, 96(7):1205–1221, 2009. [59](#)
- [77] T. McMillen and A. Goriely. Tendril perversion in intrinsically curved rods. *Journal of Nonlinear Science*, 12:241–281, 2002. [59](#), [60](#)
- [78] M. H. Godinho, J. P. Canejo, L. F. V. Pinto, J. P. Borges, and P. I. C. Teixeira. How to mimic the shapes of plant tendrils on the nano and microscale: spirals and helices of electrospun liquid crystalline cellulose derivatives. *Soft Matter*, 5:2772–2776, 2009. [59](#)
- [79] A. Goriely and M. Tabor. Spontaneous helix hand reversal and tendril perversion in climbing plants. *Phys. Rev. Lett.*, 80:1564–1567, 1998. [60](#)
- [80] C. G. Meloche, J. P. Knox, and K. C. Vaughn. A cortical band of gelatinous fibers causes the coiling of redvine tendrils: a model based upon cytochemical and immunocytochemical studies. *Planta*, 225:485–498, 2007. [60](#)
- [81] A. J. Bowling and K. C. Vaughn. Gelatinous fibers are widespread in coiling tendrils and twining vines. *American Journal of Botany*, 96(4):719–727, 2009. [60](#)
- [82] S. J. Gerbode, J. R. Puzey, A. G. McCormick, and L. Mahadevan. How the cucumber tendril coils and overwinds. *Science*, 337:1087–1091, 2012. [60](#)
- [83] Z. Haijun and O. Zhong-can. Spontaneous curvature-induced dynamical instability of Kirchhoff filaments: Application to DNA kink deformations. *The Journal of Chemical Physics*, 110(2):1247–1251, 1999. [60](#)

REFERENCES

- [84] S. Neukirch, A. Goriely, and A. C. Hausrath. Chirality of coiled coils: Elasticity matters. *Phys. Rev. Lett.*, 100:038105, 2008. [60](#)
- [85] K. Kroy and E. Frey. Force-extension relation and plateau modulus for wormlike chains. *Phys. Rev. Lett.*, 77:306–309, 1996. [61](#)
- [86] L. Le Goff, O. Hallatschek, E. Frey, and F. Amblard. Tracer studies on f-actin fluctuations. *Phys. Rev. Lett.*, 89:258101, 2002. [61](#), [62](#)
- [87] A. R. Bausch and K. Kroy. A bottom-up approach to cell mechanics. *Nature Physics*, 2:231, 2006. [61](#)
- [88] L. M. Griffith and T. D. Pollard. The interaction of actin filaments with microtubules and microtubule-associated proteins. *Journal of Biological Chemistry*, 257(15):9143–9151, 1982. [61](#)
- [89] E. Fuchs and D. W. Cleveland. A structural scaffolding of intermediate filaments in health and disease. *Science*, 279(5350):514–519, 1998. [61](#)
- [90] D. Chrétien and S. D. Fuller. Microtubules switch occasionally into unfavorable configurations during elongation. *Journal of Molecular Biology*, 298(4):663 – 676, 2000. [61](#), [64](#)
- [91] H. Herrmann et al. Structure and assembly properties of the intermediate filament protein vimentin: The role of its head, rod and tail domains. *Journal of Molecular Biology*, 264(5):933 – 953, 1996. [62](#)
- [92] C. P. Brangwynne et al. Bending dynamics of fluctuating biopolymers probed by automated high-resolution filament tracking. *Biophysical Journal*, 93(1):346 – 359, 2007. [62](#), [70](#)
- [93] F. Pampaloni and E.-L. Florin. Microtubule architecture: inspiration for novel carbon nanotube-based biomimetic materials. *Trends in Biotechnology*, 26(6):302 – 310, 2008. [63](#)
- [94] I. M. Kulić et al. The role of microtubule movement in bidirectional organelle transport. *Proceedings of the National Academy of Sciences*, 105(29):10011–10016, 2008. [63](#)

REFERENCES

- [95] A. Desai and T. J. Mitchison. Microtubule polymerization dynamics. *Annual Review of Cell and Developmental Biology*, 13(1):83–117, 1997. [64](#)
- [96] A. Mogilner and G. Oster. Polymer motors: Pushing out the front and pulling up the back. *Current Biology*, 13(18):R721 – R733, 2003. [64](#)
- [97] C. Elie-Caille et al. Straight GDP-tubulin protofilaments form in the presence of taxol. *Current biology*, 17(20):1765–1770, 2007. [65](#)
- [98] D. Chrétien, S. D. Fuller, and E. Karsenti. Structure of growing microtubule ends: two-dimensional sheets close into tubes at variable rates. *The Journal of Cell Biology*, 129(5):1311–1328, 1995. [65](#)
- [99] I. M. Jánosi, D. Chrétien, and H. Flyvbjerg. Modeling elastic properties of microtubule tips and walls. *European Biophysics Journal*, 27:501–513, 1998. [65](#), [72](#)
- [100] M. E. Janson and M. Dogterom. A bending mode analysis for growing microtubules: Evidence for a velocity-dependent rigidity. *Biophysical Journal*, 87(4):2723–2736, 2004. [65](#), [67](#)
- [101] J. C. Kurz and R. C. Williams. Microtubule-associated proteins and the flexibility of microtubules. *Biochemistry*, 34(41):13374–13380, 1995. [65](#)
- [102] P. Venier, A. C. Maggs, M. F. Carlier, and D. Pantaloni. Analysis of microtubule rigidity using hydrodynamic flow and thermal fluctuations. *Journal of Biological Chemistry*, 269(18):13353–13360, 1994. [65](#), [67](#), [69](#)
- [103] M. Kikumoto, M. Kurachi, V. Tosa, and H. Tashiro. Flexural rigidity of individual microtubules measured by a buckling force with optical traps. *Biophysical Journal*, 90(5):1687 – 1696, 2006. [66](#)
- [104] H. Felgner, R. Frank, and M. Schliwa. Flexural rigidity of microtubules measured with the use of optical tweezers. *Journal of Cell Science*, 109(2):509–516, 1996. [65](#)

REFERENCES

- [105] H. Felgner et al. Domains of neuronal microtubule-associated proteins and flexural rigidity of microtubules. *The Journal of Cell Biology*, 138(5):1067–1075, 1997. [65](#)
- [106] M. Kurachi, M. Hoshi, and H. Tashiro. Buckling of a single microtubule by optical trapping forces: Direct measurement of microtubule rigidity. *Cell Motility and the Cytoskeleton*, 30(3):221–228, 1995. [66](#)
- [107] T. Takasone et al. Flexural rigidity of a single microtubule. *Japanese Journal of Applied Physics*, 41:3015–3019, 2002. [66](#)
- [108] D. Kuchnir Fygenson, M. Elbaum, B. Shraiman, and A. Libchaber. Microtubules and vesicles under controlled tension. *Phys. Rev. E*, 55:850–859, 1997. [66](#)
- [109] A. Kis et al. Nanomechanics of microtubules. *Phys. Rev. Lett.*, 89:248101, 2002. [66](#), [67](#), [68](#), [69](#)
- [110] P. J. de Pablo, I. A. T. Schaap, F. C. MacKintosh, and C. F. Schmidt. Deformation and collapse of microtubules on the nanometer scale. *Phys. Rev. Lett.*, 91:098101, 2003. [66](#)
- [111] F. Gittes, B. Mickey, J. Nettleton, and J. Howard. Flexural rigidity of microtubules and actin filaments measured from thermal fluctuations in shape. *The Journal of Cell Biology*, 120(4):923–934, 1993. [67](#)
- [112] B. Mickey and J. Howard. Rigidity of microtubules is increased by stabilizing agents. *The Journal of Cell Biology*, 130(4):909–917, 1995. [67](#)
- [113] F. Pampaloni et al. Thermal fluctuations of grafted microtubules provide evidence of a length-dependent persistence length. *Proceedings of the National Academy of Sciences*, 103(27):10248–10253, 2006. [67](#), [68](#), [69](#)
- [114] C. Heussinger, M. Bathe, and E. Frey. Statistical mechanics of semiflexible bundles of wormlike polymer chains. *Phys. Rev. Lett.*, 99:048101, 2007. [67](#)
- [115] H. Mohrbach and I. M. Kulić. Motor driven microtubule shape fluctuations: Force from within the lattice. *Phys. Rev. Lett.*, 99:218102, 2007. [67](#)

REFERENCES

- [116] S. Timoshenko. *Theory of Elasticity*. Engineering Societies Monographs. McGraw-Hill, 1951. [67](#)
- [117] J.-P. Salvetat et al. Elastic and shear moduli of single-walled carbon nanotube ropes. *Phys. Rev. Lett.*, 82:944–947, 1999. [67](#)
- [118] H. Mohrbach, A. Johner, and I. M. Kulić. Tubulin bistability and polymorphic dynamics of microtubules. *Phys. Rev. Lett.*, 105:268102, 2010. [69](#), [70](#), [71](#), [86](#)
- [119] L. A. Amos and W. B. Amos. The bending of sliding microtubules imaged by confocal light microscopy and negative stain electron microscopy. *Journal of Cell Science*, (14):95–101, 1991. [69](#)
- [120] D. Chrétien, H. Flyvbjerg, and S. D. Fuller. Limited flexibility of the interprotofilament bonds in microtubules assembled from pure tubulin. *European Biophysics Journal*, 27:490–500, 1998. [69](#)
- [121] D. Trivedi et al. Soft robotics: Biological inspiration, state of the art, and future research. *Applied Bionics and Biomechanics*, 5(3):99–117, 2008. [86](#)
- [122] J. Guven and P. Vázquez-Montejo. Confinement of semiflexible polymers. *Phys. Rev. E*, 85:026603, 2012. [93](#)
- [123] U. Seifert, K. Berndl, and R. Lipowsky. Shape transformation of vesicles: Phase diagram for spontaneous-curvature and bilayer-coupling models. *Phys. Rev. A*, 44:1182, 1991. [97](#)
- [124] S. Svetina and B. Žekš. Membrane bending energy and shape determination of phospholipid vesicles and red blood cells. *Eur. Biophys. J.*, 17:101, 1989. [97](#)
- [125] L. Miao, B. Fourcade, M. Rao, M. Wortis, and R. K. P. Zia. Equilibrium budding and vesiculation in the curvature model of fluid lipid vesicles. *Phys. Rev. A*, 43:6843, 1991. [97](#)
- [126] F. Jülicher and U. Seifert. Shape equations for axisymmetric vesicles: A clarification. *Phys. Rev. E*, 49:4728, 1994. [97](#)

REFERENCES

- [127] U. Seifert and R. Lipowsky. Adhesion of vesicles. *Phys. Rev. A*, 42:4768, 1990. [97](#), [99](#)
- [128] U. Seifert. Self-consistent theory of bound vesicles. *Phys. Rev. Lett.*, 74:005060, 1995. [97](#)
- [129] M. Deserno and T. Bickel. Wrapping of a spherical colloid by a fluid membrane. *Europhys. Lett.*, 62:767, 2003. [97](#)
- [130] M. Deserno. Elastic deformation of a fluid membrane upon colloid binding. *Phys. Rev. E*, 69:031903, 2004. [97](#)
- [131] M. Deserno. When do fluid membranes engulf sticky colloids? *J. Phys.: Condens. Matter*, 16:S2061, 2004. [97](#)
- [132] M. M. Müller and M. Deserno. Cell model approach to membrane mediated protein interactions. *Prog. Theor. Phys. Suppl.*, 184:351, 2010. [97](#)
- [133] S. Cao, G. Wei, and J. Z. Y. Chen. Transformation of an oblate-shaped vesicle induced by an adhering spherical particle. *Phys. Rev. E*, 84:050901, 2011. [97](#)
- [134] T. R. Powers, G. Huber, and R. E. Goldstein. Fluid-membrane tethers: Minimal surfaces and elastic boundary layers. *Phys. Rev. E*, 65:041901, 2002. [97](#)
- [135] I. Derényi, F. Jülicher, and J. Prost. Formation and interaction of membrane tubes. *Phys. Rev. Lett.*, 88:238101, 2002. [97](#)
- [136] A.-S. Smith, E. Sackmann, and U. Seifert. Effects of a pulling force on the shape of a bound vesicle. *Europhys. Lett.*, 64:281, 2003. [97](#)
- [137] A.-S. Smith, E. Sackmann, and U. Seifert. Pulling tethers from adhered vesicles. *Phys. Rev. Lett.*, 92:208101, 2004. [97](#)
- [138] G. Koster et al. Force barriers for membrane tube formation. *Phys. Rev. Lett.*, 94:068101, 2005. [97](#)

REFERENCES

- [139] D. Norouzi, M. M. Müller, and M. Deserno. How to determine local elastic properties of lipid bilayer membranes from atomic-force-microscope measurements: A theoretical analysis. *Phys. Rev. E*, 74:061914, 2006. [97](#)
- [140] M. Deserno M, M. M. Müller, and J. Guven. Contact lines for fluid surface adhesion. *Phys. Rev. E*, 76:011605, 2007. [99](#)
- [141] W. H. Press et al. *Numerical Recipes in C*. Cambridge: Cambridge University Press, 1992. [100](#)
- [142] F. Cirak, M. Ortiz, and P. Schröder. Subdivision surfaces: a new paradigm for thin-shell finite-element analysis. *Int. J. Numer. Methods Eng.*, 47:2039–2072, 2000. [101](#), [102](#)
- [143] F. Cirak and M. Ortiz. Fully C^1 -conforming subdivision elements for finite element-deformation thin-shell analysis. *Int. J. Numer. Methods Eng.*, 51:813–833, 2001. [101](#)
- [144] P. Volino and N. Magnenat-Thalmann. Resolving surface collisions through intersection contour minimization. *ACM Transactions on Graphics (SIGGRAPH)*, 25(3):1154–1159, 2006. [105](#)
- [145] M. Attene and B. Falcidieno. Remesh: An interactive environment to edit and repair triangle meshes. In *SMI 06: Proceedings of the IEEE International Conference on Shape Modeling and Applications 2006 (SMI'06)*, page 41. Society Press, 2006. [106](#)
- [146] T. Möller. A fast triangle-triangle intersection test. *Journal of Graphics Tools*, 2(2):25–30, 1997. [106](#)